FORCE MICROSCOPY OF TWO-DIMENSIONAL MATERIALS

A Dissertation
Presented to
The Academic Faculty

by

Yang Gao

In Partial Fulfillment
of the Requirements for the Degree
Doctor of Philosophy in the
School of Physics

Georgia Institute of Technology
May 2017

FORCE MICROSCOPY OF TWO-DIMENSIONAL MATERIALS

Approved by:

Dr. Elisa Riedo, Advisor
School of physics
Georgia Institute of Technology
and Advanced Science Research Center
City University of New York

Dr. Phillip N. First
School of Physics
Georgia Institute of Technology

Dr. Zhigang Jiang
School of Physics
Georgia Institute of Technology

Dr. Levent Degertekin
School of Mechanical Engineering
Georgia Institute of Technology

Dr. Dragomir Davidovic
School of Physics
Georgia Institute of Technology

Date Approved: [March 22, 2017]

To my beloved families and friends.

ACKNOWLEDGEMENTS

In addition, I'm very grateful to my defense committee members for their guidance and advices: Professor Dragomir Davidovic, Professor Zhigang Jiang, Professor Phillip N. First and Professor Levent Degertekin.

I want to thank my friends in Atlanta - Qi, Chao, Shangguo, Zhangxian, Xincheng, Wenchao, Wenbin, Xiong, Xiaoyun, Kan, Haoran, Yanyan, Zhihan, Jingjing and Jing for their immense help and support.

I also would like to thank my friends in New York: Shoushou, Jiumei, Kaikai, Dingding, Gege, Didi, Riri, Guanguan, Chuchu and others. 1105 is the best apartment in the world.

Thanks to everyone mentioned and not mentioned again!

TABLE OF CONTENTS

LIST OF TABLES

LIST OF FIGURES

SUMMARY

In this thesis we report on the development of a novel atomic force microscope (AFM) based sub-Å resolution indentation technique termed as Modulated Nano-indentation (MoNI) or more specifically, Å – indentation. MoNI was originally invented by customizing a commercial AFM to measure the radial elasticity of multi-walled carbon nanotubes in 2005. Later on we successfully applied MoNI on the investigation of the interlayer elasticity of two-dimensional (2D) materials.

Different from traditional nano-indentation technique (whether based on AFM or nano-indenter), of which the indentation depth is usually from 10nm to over 1μm, MoNI can allow for extremely shallow indentation depth below 1Å. The ability to produce an Å - scale deformation provides the possibility for the first time to precisely study the inter-layer van der Waals interaction and intercalation properties of 2D materials without surface destruction or interruption from the in-plane covalent bonds.

This thesis includes the basic background knowledge of elastic theory, contact mechanics and AFM in the first chapter and a brief introduction of two-dimensional materials in Chapter II. In Chapter III we present a detailed description of MoNI setup, experiment steps and data error analysis. In Chapter IV, we show the most recent MoNI results on a variety of 2D materials including graphene and graphene oxide at varying ambient humidity. Furthermore, the fingerprint of a new ultra-hard phase of epitaxial graphene on Silicon Carbide (SiC), which indicates the possibility of room-temperature diamondization, is discussed in Chapter V. In the last Chapter, we briefly summarize this thesis, discuss some other related results and take a short outlook of future developments.

CHAPTER 1.   FUNDAMENTALS

This thesis reports on the study of inter-layer elasticity of two-dimensional materials with atomic force microscopy (AFM). Hence it's quite necessary to give a brief introduction of the basic ideas of elastic theory in the first chapter. The elastic theory part in this chapter is mainly originated from Landau and Lifshitz's book "Theory of Elasticity"[1]. In the second section of this chapter we discuss Heinrich Hertz's theory about contact mechanics [2] and other improved models which take adhesion forces into consideration. In the last sections, we briefly talk about the fundamental mechanism of AFM [3] and its applications in the study of mechanical properties of 2D materials.

1.1   Theory of Elasticity

The elastic property of materials has been studied both theoretically and experimentally for hundreds of years not only for fundamental scientific understanding but also because it's the key property for a wide range of applications [1, 4]. Young's modulus (*E,* also known as elastic modulus), which describes material's ability to resist external stress is the most well-known and commonly used elastic constant. However, the elastic properties of almost all the known materials in principal cannot be featured only with Young's modulus.

The first point we have to make clear in the beginning is that in theory of elasticity we only consider solid bodies which can be regarded as continuous and homogeneous media.

1.1.1 Strain Tensor

The position of a point in a solid continuous body can be described with radius vector *r* in some co-ordinate systems. For example, if we use Cartesian co-ordinate system, we can define the position of any point with $x_1 (= x)$, $x_2 (= y)$ and $x_3 (= z)$. If the solid body is deformed under the action of external forces, the positon of every point will change form *r* to *r'*. The displacement of an arbitrary point is then given by *r' - r.* We can denote the point *displacement vector* with *u* (= *r' - r*):

$$u_i = x'_i - x_i \quad (i = 1, 2, 3) \tag{1.1.1}$$

Notice that the position vector x'_i and displacement vector u_i are apparently functions of the position vector x_i before deformation.

If we consider two points which are very close, the radius vector connecting the two points can be written as dx_i and the distance dl is $\sqrt{dx_i dx_i}$ using the general summation rule. When the solid body is deformed, the distance between to close points will also change. The radius vector is then $dx'_i = dx_i + du_i$. The distance dl' is thus given by

$$dl' = \sqrt{dx'^2_i} = \sqrt{(dx_i + du_i)^2} = \sqrt{dl^2 + du_i^2 + 2dx_i du_i} \tag{1.1.2}$$

If we replace $du_i = (\partial u_i / \partial x_j) \cdot dx_j$ in Eq. 1.1.2, we have

$$dl'^2 = dl^2 + 2\frac{\partial u_i}{\partial x_j}dx_j dx_i + \frac{\partial u_i}{\partial x_j}\frac{\partial u_i}{\partial x_k}dx_j dx_k \tag{1.1.3}$$

2

Actually second term on the right side of Eq. 1.1.3 is completely symmetric with i and j (i.e. if we exchange i and j the result remains unchanged) and the summation in is taken over both i and j, we can re-write is as $(\partial u_i / \partial x_j) \cdot dx_j dx_i + (\partial u_j / \partial x_i) \cdot dx_j dx_i$. Then we exchange the suffix i and k in the third term. Thus Eq. 1.1.3 can be transformed into the following form:

$$dl'^2 = dl^2 + 2u_{ij} dx_i dx_j \tag{1.1.4}$$

where $u_{ij} = u_{ji} \equiv \dfrac{1}{2}(\dfrac{\partial u_i}{\partial x_j} + \dfrac{\partial u_j}{\partial u_i} + \dfrac{\partial u_k}{\partial u_i}\dfrac{\partial u_k}{\partial u_j})$. This symmetrical tensor u_{ij} is called the *strain tensor*. If the body only experiences small deformation u_i is small so the last term in the strain tensor u_{ij} can be neglected. The strain tensor can be simplified as

$$u_{ij} = \dfrac{1}{2}(\dfrac{\partial u_i}{\partial x_j} + \dfrac{\partial u_j}{\partial u_i}) \tag{1.1.5}$$

Since the strain tensor is symmetrical, we can diagonalize it at any point in the body, which means we can choose any co-ordinate system such that only the diagonal elements u_{11}, u_{22} and u_{33} in the strain tensor are non-zero. We call these three components the principal values of the strain tensor and the corresponding co-ordinate axes as principal axes.

1.1.2   Stress Tensor

When a solid body is deformed, the arrangement of the molecules in the body will change and body ceases to be in its original state of equilibrium. The induced internal forces which tend to make the solid body system back to equilibrium, are called internal stresses. The internal stresses are due to the molecule interactions are short-range (or near action)

actions, which only act to the neighbouring points. Therefore, in the theory of elasticity, the forces exerted on any part of the body by surrounding parts act only on the surface of that part.

The total force exerted on a portion of the body can be written as the sum of all the forces on all the volume of that portion: $\int \vec{F}dV$, where $\vec{F}$ is the force per unit volume. Since the internal forces will cancel with each other (due to Newton's third law), only the forces acting on the surface of the portion need to be considered. Thus, for any part of the solid body, the total forces can transformed into the integral over the surface. According to Guass's law, the integral of the divergence of a vector over an arbitrary closed surface is equal to the integral of the vector's divergence (a scalar) over the volume enclosed by the surface. In our case, we have the integral of a vector over a volume, so the vector F_i must be the divergence of a rank-two tensor:

$$F_i = \partial \sigma_{ij} / \partial x_j \tag{1.1.6}$$

Then the force on the volume becomes

$$\int F_i dV = \int \frac{\partial \sigma_{ij}}{\partial x_j} dV = \oint \sigma_{ij} df_j \tag{1.1.7}$$

where df_i are the components of the surface element vector, directing along the outward normal. The tensor σ_{ij} is called *stress tensor*. To be more specific, for example, σ_{xx} is just the force per unit area perpendicular to the *x*-axis and the tangential forces (or shear force) along the *y* and *z* axes are σ_{yx} and σ_{zx}, respectively. In the general case of arbitrary deformation, not only the diagonal but also the non-diagonal elements in the stress tensor

are non-zero, which means there are not only normal forces but also tangential (shear) forces. We also mark here that the stress tensor is symmetrical.

1.1.3 *Thermodynamics of Deformation*

We can easily obtain the work done by the internal stresses by simply multiplying the force $F_i = \partial\sigma_{ij}/\partial x_j$ with the displacement δu_i and integrating over the volume:

$$W = \int \delta R dV = \int (\partial\sigma_{ij}/\partial x_j)\delta u_i dV \qquad (1.1.8)$$

where δR denotes the work done by the internal stresses per unit volume. We can transform Eq. 1.1.8 by using Green's theorem:

$$W = \int \delta R dV = \oint \sigma_{ij}\delta u_i df_j - \int \sigma_{ij}\frac{\partial\delta u_i}{\partial x_j} dV \qquad (1.1.9)$$

If we consider an infinite medium so the deformation at infinity should be zero. The first term in Eq. 1.1.9 should then be zero. The second term can be written in the following form by using the symmetry of the stress tensor:

$$\int \delta R dV = -\frac{1}{2}\int \sigma_{ij}(\frac{\partial\delta u_i}{\partial x_j} + \frac{\partial\delta u_j}{\partial x_i})dV = -\int \sigma_{ij}\delta u_{ij} dV \qquad (1.1.10)$$

Hence we can easily get the work per unit volume in terms of the change in the strain tensor:

$$\delta R = -\sigma_{ij}\delta u_{ij} \qquad (1.1.11)$$

If the deformation of the solid body is much smaller than its original size, it returns to its undeformed state when the external forces which cause the deformation cease to act. Such deformations are *elastic*. For large deformations, the total deformations do not disappear when the external forces are retracted, in other words a *residual deformation* remains in the solid body. In this case, the deformation is *plastic*. In this thesis, we only consider elastic deformation.

During an elastic deformation, the total internal energy change *dU* equals to the sum of the total work done on the system by the external force *W* and the heat absorbed by the system. For a reversible process, the heat is *Q* = *TdS*, where *T* is the temperature and *S* is the system's entropy. The work done by the internal forces is given by Eq. 1.1.11 so the work done by the external force is the $-\delta R$ (we assume the solid body system is at thermodynamic equilibrium at every instant, which is true for most practical processes). We have

$$dU = TdS + \sigma_{ij} du_{ij} \qquad (1.1.12)$$

Actually we can easily find out that $\sigma_{ij} du_{ij} = pdV$. According to thermodynamics, the free energy *F* = *U-TS*, we have

$$dF = -SdT + \sigma_{ij} du_{ij} \qquad (1.1.13)$$

Finally the thermodynamic potential Φ is defined as:

$$\Phi = U - TS - pV \qquad (1.1.14)$$

So we have

6

$$d\Phi = -SdT - u_{ij}d\sigma_{ij} \tag{1.1.15}$$

Based on the thermodynamic equations we just derived above, we have

$$\begin{cases} \sigma_{ij} = \left(\dfrac{\partial U}{\partial u_{ij}}\right)_S = \left(\dfrac{\partial F}{\partial u_{ij}}\right)_T \\[3mm] u_{ij} = -\left(\dfrac{\partial \Phi}{\partial_{ij}}\right)_T \end{cases} \tag{1.1.16}$$

1.1.4   Hooke's Law of Isotropic Body

In this section, we only consider isotropic body at constant temperature. When the solid body is not deformed, both the strain and stress tensors should be zero. Since

$\sigma_{ij} = \left(\dfrac{\partial F}{\partial u_{ij}}\right)_T$, we can conclude that there's no linear term in the expansion of F in powers

of strain tensor u_{ij}. Notice that the free energy F is a scalar so its expansion should also be a scalar. Two independent scalars of the second degree can be formed from the components of the symmetrical tensor u_{ij}: they can be taken as the superposition of squared sum of the diagonal components and the sum of the squares of all the components:

$$F = F_0 + \frac{1}{2}\lambda u_{ii}^2 + \mu u_{ij}^2 \tag{1.1.17}$$

Eq. 1.1.17 is the general expansion of the free energy of a deformed isotropic body. λ and μ are *Lamé coefficients*.

7

If the body volume does not change during the deformation and only the shape of the body changes, it is called a pure shearing; if the deformation only causes a volume change without altering its shape, it is a hydrostatic compression. Any deformation can be regarded as a combination of pure shearing and hydrostatic compression. We can decompose the strain tensor in the following format:

$$u_{ij} = (u_{ij} - \frac{1}{3}\delta_{ij}u_{kk}) + \frac{1}{3}\delta_{ij}u_{kk}, \quad \delta_{ij} = \begin{cases} 1, & i = j \\ 0, & i \neq j \end{cases} \quad (1.1.18)$$

The first term is then pure shearing and the second term can be attributed to hydrostatic compression. Plug Eq. 1.1.18 into Eq. 1.1.17, we have

$$F = F_0 + \mu(u_{ij} - \delta_{ij}u_{kk})^2 + \frac{1}{2}Ku_{kk}^2, \quad K = \lambda + \frac{2}{3}\mu \quad (1.1.19)$$

K and μ are called the *modulus of compression* and the *modulus of rigidity*. Obviously, both K and μ are positive. We can take the differentiation of F in terms of the strain tensor to get the stress tensor.

$$dF = [Ku_{kk}\delta_{ij} + 2\mu(u_{ij} - \frac{1}{3}u_{kk}\delta_{ij})]du_{ij} \quad (1.1.20)$$

Based on Eq. 1.1.16, the stress tensor is:

$$\sigma_{ij} = \frac{\partial F}{\partial u_{ij}} = Ku_{kk}\delta_{ij} + 2\mu(u_{ij} - \frac{1}{3}u_{kk}\delta_{ij}), \text{ constant } T \quad (1.1.21)$$

Especially when $i = j$, we have $\sigma_{ii} = 3Ku_{ii}$. We can also write the strain tensor in terms of the stress tensor:

8

$$u_{ij} = \delta_{ij}\sigma_{kk}/9K + (\sigma_{ij} - \frac{1}{3}\delta_{ij}\sigma_{kk})/2\mu \qquad (1.1.22)$$

We see from Eq. 1.1.22 that the strain tensor of an isotropic solid body is a linear function of the stress tensor. In other words, the deformation is proportional to the applied force. This is so-called the *Hooke's law* of isotropic body.

Now let's consider a simple case called *homogeneous deformation*, which means the strain tensor is constant throughout the whole solid medium. To simplify the situation without loss of generality, we consider the compression (or elongation) of an isotropic rod as shown in Fig. 1.1.1. The external force is only applied on the *z*-direction, which means no force is applied on the sidewall of the rod. Thus σ_{ji} is non-zero only when $i = j$. Based on Eq. 1.1.22, only the diagonal components of the strain and stress tensors are not zero. If the force per unit area is *p* (pressure), we have:

$$\begin{cases} u_{zz} = \dfrac{1}{3}(\dfrac{1}{3K} + \dfrac{1}{\mu})p \\ u_{xx} = u_{yy} = -\dfrac{1}{3}(\dfrac{1}{2\mu} - \dfrac{1}{3K})p \end{cases} \qquad (1.1.23)$$

Actually, the pressure applied on the rod is the stress tensor σ_{zz}, so we have

$$E = \frac{\sigma_{zz}}{u_{zz}} = 3/(1/3K + 1/\mu) = 9K\mu/(3K + \mu) \qquad (1.1.24)$$

Here the parameter *E* is just the *Young's modulus* of this isotropic rod.

We also notice that the deformations on the x and y direction are not zero when the force is only applied on the z-axis. The ratio of transverse (u_{xx} and u_{yy}) deformation and longitudinal deformation u_{zz} is defined as the *Poisson's Ratio*:

$$v = \frac{1}{2}(1 - \frac{3}{3K/\mu + 1})$$

(1.1.25)

K and μ are both positive, so we obtain an important conclusion:

$$-1 \leq v \leq \frac{1}{2}$$

(1.1.26)

We mark here that there are actually no substances known with negative Poisson's ratio, which would expand transversely while being elongated longitudinally. For general isotropic body with arbitrary shape, we have:

$$\begin{cases} \sigma_{xx} = \frac{E}{(1+v)(1-2v)}[(1-v)u_{xx} + v(u_{yy} + u_{zz})] \\ \sigma_{yy} = \frac{E}{(1+v)(1-2v)}[(1-v)u_{yy} + v(u_{xx} + u_{zz})] \\ \sigma_{zz} = \frac{E}{(1+v)(1-2v)}[(1-v)u_{zz} + v(u_{xx} + u_{yy})] \\ \sigma_{xy} = \frac{E}{1+v}u_{xy}, \sigma_{yz} = \frac{E}{1+v}u_{yz}, \ \sigma_{xz} = \frac{E}{1+v}u_{xz} \end{cases}$$

(1.1.27)
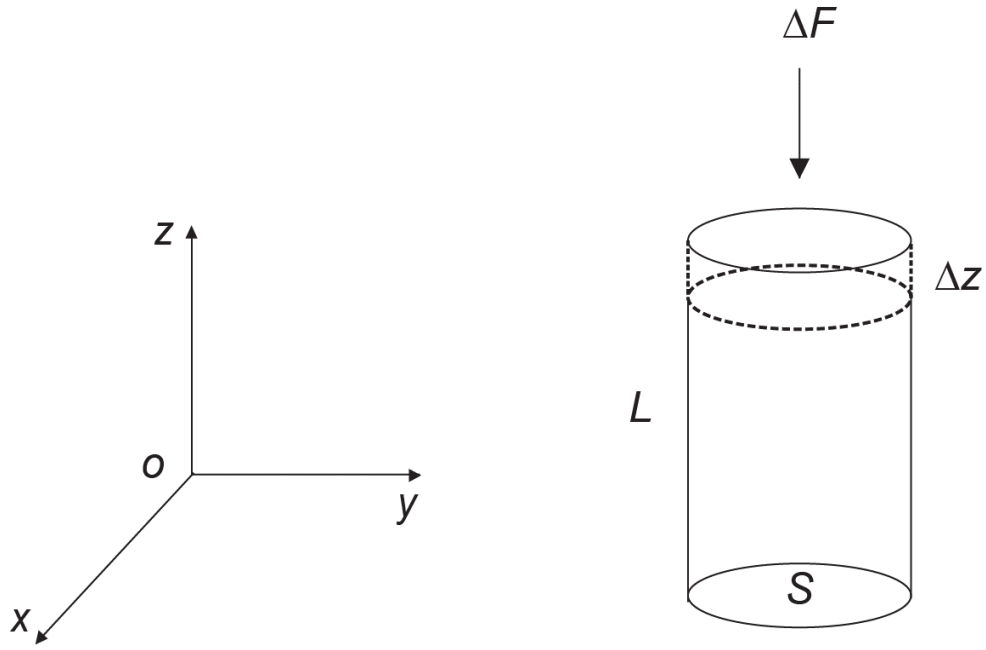
Figure 1.1.1: The hydrostatic compression on an isotropic rod. The force ΔF is applied on the z-direction and the consequent deformation is Δz.

If the length of the rod is L and cross-sectional area is S; the applied force is ΔF and the deformation is Δz (Δz is fairly small compared with total length L so that the area S is almost unchanged) as shown in Fig. 1.1.1, then the strain and stress tensor are:

$$
\begin{cases}
u_{zz} = \dfrac{\Delta z}{L} \\
\sigma_{zz} = \dfrac{\Delta F}{S}
\end{cases}
\tag{1.1.28}
$$

Then the Young's modulus is

$$E = \frac{\sigma_{zz}}{u_{zz}} = \frac{L}{S} \frac{\Delta F}{\Delta z}$$

$$\Rightarrow \frac{\Delta F}{\Delta z} = k = \frac{ES}{L}$$

(1.1.29)

Therefore we arrive to the familiar relationship between the spring constant k of an isotropic rod and its Young's modulus.

1.1.5   Elastic Properties of Anisotropic Materials

For isotropic medium, there are only two elastic constants – Young's modulus E and Poisson's ratio v. However, pure isotropic materials do not exist in our world (some materials can be categorized as quasi-isotropic materials if the elastic properties are close in all directions). For a general case of an-isotropic materials, the free energy needs to be written in this way:

$$F = \frac{1}{2} C_{ijkl} u_{ij} u_{kl}$$

(1.1.30)

where C_{ijkl} is a tensor of rank four, called the *elastic modulus tensor*. Since the strain tensor is symmetrical, the product in Eq. 1.1.29 does not change if we interchange the indexes i, j, k and l. Thus we can define the elastic modulus tensor is with the following symmetry:

$$C_{ijkl} = C_{jikl} = C_{ijlk} = C_{klij}$$

(1.1.31)

With the symmetry above, there are now only 21 independent elements in the elastic modulus tensor. Based on Eq. 1.1.16, we have the relationship between stress tensor and strain tensor:

12

$$\sigma_{ij} = \frac{\partial F}{\partial u_{ij}} = C_{ijkl} u_{kl} \tag{1.1.32}$$

If the solid medium possesses some symmetries (most crystals do have geometric symmetries), the number of independent elements in the elastic modulus tensor can be reduced. However, here we only discuss one special symmetry – *transversely isotropic material* for simplicity. More detailed discussion can be found in [1]. Transversely isotropic material, by its definition, is elastically isotropic in a certain plane (*x-y* plane) but not necessarily isotropic in the remaining out-of-plane direction (*z*). The most common transversely isotropic material is layered structure material. Two-dimensional (2D) materials, which consist of a few atomic layers with strong in-plane covalent bonds and weaker inter-layer van de Waals interaction, is a perfect example of transversely isotropic materials. More unique and outstanding properties of 2D materials are introduced in detail in the next chapter.

Since both the strain and stress tensor are symmetric, we can use Voigt notation to write the relationship between stress and strain tensor as:

$$\begin{bmatrix} \sigma_1 \\ \sigma_2 \\ \sigma_3 \\ \sigma_4 \\ \sigma_5 \\ \sigma_6 \end{bmatrix} = \begin{bmatrix} C_{11} & C_{12} & C_{13} & C_{14} & C_{15} & C_{16} \\ C_{12} & C_{22} & C_{23} & C_{24} & C_{25} & C_{26} \\ C_{13} & C_{23} & C_{33} & C_{34} & C_{35} & C_{36} \\ C_{14} & C_{24} & C_{34} & C_{44} & C_{45} & C_{46} \\ C_{15} & C_{25} & C_{35} & C_{45} & C_{55} & C_{56} \\ C_{16} & C_{26} & C_{36} & C_{46} & C_{56} & C_{66} \end{bmatrix} \begin{bmatrix} u_1 \\ u_2 \\ u_3 \\ u_4 \\ u_5 \\ u_6 \end{bmatrix} \tag{1.1.33}$$

where $(\sigma_1, \sigma_2, \sigma_3, \sigma_4, \sigma_5, \sigma_6) = (\sigma_{xx}, \sigma_{yy}, \sigma_{zz}, \sigma_{yz}, \sigma_{xz}, \sigma_{xy})$. The strain tensor u_{ij} follows the same index rule. For the simplest isotropic case, we can easily find from Eq.1.1.27 (see next page):

$$
\begin{bmatrix}
C_{11} & C_{12} & C_{13} & C_{14} & C_{15} & C_{16} \\
C_{12} & C_{22} & C_{23} & C_{24} & C_{25} & C_{26} \\
C_{13} & C_{23} & C_{33} & C_{34} & C_{35} & C_{36} \\
C_{14} & C_{24} & C_{34} & C_{44} & C_{45} & C_{46} \\
C_{15} & C_{25} & C_{35} & C_{45} & C_{55} & C_{56} \\
C_{16} & C_{26} & C_{36} & C_{46} & C_{56} & C_{66}
\end{bmatrix}
$$

$$
= \begin{bmatrix}
\dfrac{(1-v)E}{(1+v)(1-2v)} & \dfrac{vE}{(1+v)(1-2v)} & \dfrac{vE}{(1+v)(1-2v)} & 0 & 0 & 0 \\
\dfrac{vE}{(1+v)(1-2v)} & \dfrac{(1-v)E}{(1+v)(1-2v)} & \dfrac{vE}{(1+v)(1-2v)} & 0 & 0 & 0 \\
\dfrac{vE}{(1+v)(1-2v)} & \dfrac{vE}{(1+v)(1-2v)} & \dfrac{(1-v)E}{(1+v)(1-2v)} & 0 & 0 & 0 \\
0 & 0 & 0 & \dfrac{E}{1+v} & 0 & 0 \\
0 & 0 & 0 & 0 & \dfrac{E}{1+v} & 0 \\
0 & 0 & 0 & 0 & 0 & \dfrac{E}{1+v}
\end{bmatrix}
\quad (1.1.34)
$$

For transversely isotropic materials, there are five independent elements in the elastic modulus tensor as following:

$$
\overline{C} = \begin{bmatrix} C_{11} & C_{12} & C_{13} & 0 & 0 & 0 \\ C_{12} & C_{22} & C_{23} & 0 & 0 & 0 \\ C_{13} & C_{23} & C_{33} & 0 & 0 & 0 \\ 0 & 0 & 0 & C_{44} & 0 & 0 \\ 0 & 0 & 0 & 0 & C_{44} & 0 \\ 0 & 0 & 0 & 0 & 0 & (C_{11}-C_{12})/2 \end{bmatrix} \tag{1.1.35}
$$

The inverse matrix in *engineering notation* is (next page):

$$
\overline{\lambda}^{-1} = \begin{bmatrix} \dfrac{1}{E_x} & -\dfrac{v_{yx}}{E_x} & -\dfrac{v_{zx}}{E_z} & 0 & 0 & 0 \\ -\dfrac{v_{xy}}{E_x} & \dfrac{1}{E_y} & -\dfrac{v_{zy}}{E_z} & 0 & 0 & 0 \\ -\dfrac{v_{zx}}{E_z} & -\dfrac{v_{zy}}{E_z} & \dfrac{1}{E_z} & 0 & 0 & 0 \\ 0 & 0 & 0 & \dfrac{1}{G_{yz}} & 0 & 0 \\ 0 & 0 & 0 & 0 & \dfrac{1}{G_{xz}} & 0 \\ 0 & 0 & 0 & 0 & 0 & \dfrac{2(1+v_{xy})}{E_x} \end{bmatrix}
$$

$$
\begin{aligned}
E_z &= C_{33} - 2C_{13}^2/(C_{11}+C_{12}) \\
E_x &= E_y = (C_{11}-C_{12})(C_{11}C_{13}+C_{12}C_{33}-2C_{13}^2)/(C_{11}C_{33}-C_{13}^2) \\
G_{xy} &= (C_{11}-C_{12})/2 = C_{66} \\
v_{xz} &= v_{yz} = C_{13}/(C_{11}+C_{12}) \\
G_{yz} &= G_{xz} = C_{44}(C_{11}C_{13}+C_{12}C_{33}-2C_{13}^2)/(C_{11}-C_{12})
\end{aligned} \tag{1.1.36}
$$

In Eq. 1.1.36, E_z is the out-of-plane (or perpendicular-to-the-plane) Young's modulus, E_x

$= E_y$ is the in-plane Young's modulus, G_{xy} is the in-plane shear modulus (can be derived

from v_{xy}), $v_{xz} = v_{yz}$ is the out-of-plane Poisson's ratio and $G_{yz} = G_{xz}$ is the out-of-plane shear modulus. In 2D materials, E_x (E_y) indicates the strength of the in-plane covalent bonds and E_z shows how strong is the inter-layer van der Waals interaction. Usually $E_x > E_z$ since covalent bonds are stronger than van der Waals interactions

1.2   Contact Mechanics

In this section we will discuss how two different homogeneous mediums deform when they are in contact under external forces. As usual, we start from the simplest case: two infinite isotropic half-space with different Young's moduli and Poisson's ratios. Assume the normal pressure perpendicular to the contact plane is P, then the deformations of the two mediums are $z_1 = P/E_1$, $z_2 = P/E_2$. The total displacement $z = z_1 + z_2 = P(1/E_1 + 1/E_2)$. The effective Young's modulus is then

$$E^* = P/z = (1/E_1 + 1/E_2)^{-1} \tag{1.2.1}$$

1.2.1   Hertz Model

Heinrich Hertz first gave the analytical solution for the contact between two isotropic elastic bodies in 1882 while he was attempting to understand how the optical properties of two lenses will change while holding them together with forces [2].

Consider two elastic bodies in contact at a point as shown in Fig. 1.2.1. We denote the positive z-axis pointing into each body as z and z'. Near a point of ordinary contact with the xy-plane, the equation of the surface is
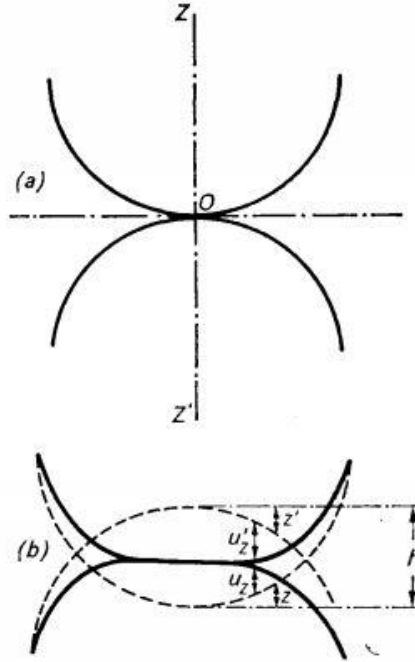
Figure 1.2.1: Two elastic bodies in contact. Surfaces before deformation are shown in (a), and squeezed surfaces in (b). Reprinted with permission from [1]. Copyright 1959, Pergamon Press Ltd.

$$\begin{cases} z = k_{ij} x_i x_j \\ z' = k_{ij}' x_i x_j \end{cases} i, j = 1,2 \tag{1.2.2}$$

k_{ij} and k_{ij}' are two symmetric tensors of rank two, whose principal values are $1/2R$ and $1/2R$', R and R' are the radii of curvature of the two elastic bodies at the contact point. Assume the two bodies are held closer by a distance d with a normal force F (parallel to z and z'). For arbitrary point in the contact region, we have

$$\begin{aligned} (z + u_z) &= (z' + u_z') = d \\ &= (k_{ij} + k_{ij}') x_i x_J + u_z + u_z' \end{aligned} \tag{1.2.3}$$

17

where u_z and u_z' are the displacements of the two elastic bodies, respectively. If we denote the principal values of $(k_{ij} + k_{ij}')$ as A and B, then we have

$$Ax^2 + By^2 + u_z + u_z' = d \qquad (1.2.4)$$

If the pressure at any point (x, y) in the contact region is P (x, y), we can write the displacement as a function of x and y in the following way (detailed derivation refers to [1]):

$$\begin{cases} u_z = \dfrac{1-v^2}{\pi E} \iint \dfrac{P(x, y)}{r} dxdy \\ u_z' = \dfrac{1-v'^2}{\pi E'} \iint \dfrac{P(x, y)}{r} dxdy \end{cases}, \quad r = \sqrt{x^2 + y^2} \qquad (1.2.5)$$

where E, v and E', v' are the Young's moduli and Poisson's ratio of the two elastic bodies, respectively. Plug Eq. 1.2.5 into Eq. 1.2.4, we have the pressure distribution of the contact

$$\frac{1}{\pi}\left(\frac{1-v^2}{E} + \frac{1-v'^2}{E'}\right)\iint \frac{P(x, y)}{r} dxdy = d - Ax^2 - By^2 \qquad (1.2.6)$$

The contact area is an ellipse

$$\frac{x^2}{a^2} + \frac{y^2}{b^2} = 1 \qquad (1.2.7)$$

and the contact pressure has the form

$$P(x, y) = \frac{3F}{2\pi ab}\sqrt{1 - \frac{x^2}{a^2} - \frac{y^2}{b^2}} \qquad (1.2.8)$$

18

Plug Eq. 1.2.8 into Eq. 1.2.6, we obtain

$$\frac{4F}{3\pi E^*}\int_0^\infty \frac{1-\dfrac{x^2}{a^2+\xi}-\dfrac{y^2}{b^2+\xi}}{\sqrt{(a^2+\xi)(b^2+\xi)}}d\xi = d - Ax^2 - By^2,$$ (1.2.9)

where $E^* = (\dfrac{1-v^2}{E}+\dfrac{1-v'^2}{E'})^{-1}$

Compare both sides on Eq. 1.2.9, we can easily conclude that

$$\begin{cases} d = \dfrac{4F}{3\pi E^*}\int_0^\infty \dfrac{d\xi}{\sqrt{\xi(a^2+\xi)(b^2+\xi)}} \\[3mm] A = \dfrac{4F}{3\pi E^*}\int_0^\infty \dfrac{d\xi}{(a^2+\xi)\sqrt{\xi(a^2+\xi)(b^2+\xi)}} \\[3mm] B = \dfrac{4F}{3\pi E^*}\int_0^\infty \dfrac{d\xi}{(b^2+\xi)\sqrt{\xi(a^2+\xi)(b^2+\xi)}} \end{cases}$$ (1.2.10)

A and *B* are both geometrical parameters which can be determined based on the shape of the two elastic bodies. Thus *a* and *b* be can be completely calculated from Eq.1.2.10. Then the force *F* vs. displacement *d* and contact pressure distribution are also given by Eq. 1.2.10 and Eq. 1.2.8.

Now let's consider a simple case of two spheres in contact. Then we have $A = B = 1/2R +1/2R'$. From Eq. 1.2.10, we have

$$a = b = F^{\frac{1}{2}}(\frac{3}{4E^*}\frac{1}{1/R+1/R'})^{\frac{1}{3}}$$ (1.2.11)

a is actually the contact radius under *F*. Plug Eq. 1.2.11 into Eq. 1.2.10, we have the indentation relationship:

$$F = \frac{4}{3}E^*(\frac{1}{R} + \frac{1}{R'})^{-\frac{1}{2}}d^{\frac{3}{2}}, \ E^* = (\frac{1-v^2}{E} + \frac{1-v'^2}{E'})^{-1} \tag{1.2.12}$$

Where E^* is the so called *effective Young's modulus*. If *R'* is infinitely large, meaning an isotropic sphere with radius *R* indenting an isotropic half-space, we have

$$F = \frac{4}{3}E^*R^{\frac{1}{2}}d^{\frac{3}{2}} \tag{1.2.13}$$

1.2.2   One Step Further Than Hertz: JKR and DMT Models

In 1971, Johnson, Kendall and Roberts (JKR) proposed a new theory that took adhesion between two elastic bodies into account [5]. They derived the following equation to describe the contact radius between a sphere and a plane in presence of adhesion:

$$a_{JKR} = \{\frac{3R}{4E^*}[F_z - 2F_{po} + 2\sqrt{(-F_{po}F_z + F_{po}^2)}]\}^{1/3} \tag{1.2.14}$$

In Eq. (8), the pull-off force in the JKR model is $F_{po}(JKR) = -\frac{3}{2}\gamma\pi R$, where γ is the Dupré energy of adhesion, or work of adhesion. It is, in fact, an energy per unit area and it represents the work done in completely separating a unit area of the interface. A key characteristics of this theory is a non-zero contact area at zero load and a pull-off force which still exhibits a non-zero contact area.

Derjaguin, Muller and Toporov (DMT) developed a separate expression to include adhesion in the contact of elastic bodies [6]. In DMT theory, the deformed contact profile remains the same as in the Hertz theory, but with an overall higher load due to adhesion. This is equivalent to attractive interactions acting at all separations between the sphere and the plane, thus:

$$a_{DMT} = (\frac{3R}{4E^*}(F_z - F_{po}))^{1/3}$$ (1.2.15)

In the DMT model, the adhesion force is constant and the contact area goes to zero when the load reaches the value of the pull-off force, $F_{po}(DMT) = -2\gamma\pi R$, i.e. there is no singularity in the contact stresses. The form of the contact area in the DMT model was, in fact, first presented in the work of Maugis [7] and is often referred to as the "Hertz-plus-offset" model.

JKR and DMT models are quite different mathematically and indeed are appropriate in two opposite regimes. Tabor (1977) defined a parameter to show that JKR and DMT models can be regarded as two extreme limits of one theory [8]. This parameter is called *Tabor parameter*:

$$\mu = \frac{d_c}{z_0} \approx (\frac{R\gamma^2}{E^{*2}z_0^2})^{\frac{1}{3}}$$ (1.2.16)

where d_c is the critical depth of penetration defined as the deformation when the applied force is zero. z_0 is the equilibrium separation between the two contact surfaces. When surface forces are short range compared to the resulting elastic deformations (i.e. compliant materials, large sphere radii, and strong, short-range adhesion forces), the Tabor parameter

is large where the JKR model describes the contact area accurately. The opposite limit (i.e. stiff materials, small sphere radii and weak, long-range adhesion forces) corresponds to a small Tabor parameter and it lies in the DMT regime.

1.2.3 Other Contact Mechanics Models

In between the two extreme regimes described by JKR and DMT models, other models have been developed such as the Maugis-Dugdale model [7] and the Carpick-Ogletree-Salmeron (COS) model [9].

In Maugis-Dugdale model [7], perfect contact occurs within the contact radius a predicted by Hertz and the adhesive force extends to an area with radius c. The vertical displacement $u(c)$ and separation $h(c)$ at c are given by

$$\begin{cases} u(c) = \frac{1}{\pi R}[a^2(2 - \frac{c^2}{a^2})\arcsin(\frac{a}{c}) + a^2\sqrt{c^2/a^2 - 1}] \\ h(c) = \frac{c^2}{2R} - \frac{a^2}{R} + u(c) \end{cases} \qquad (1.2.17)$$

Then the pressure distribution is

$$p(r) = \begin{cases} -\frac{\sigma_0}{\pi}\arccos(\frac{2 - \frac{c^2 - r^2}{a^2}}{\frac{c^2}{a^2}(1 - \frac{r^2}{c^2})}) & , \quad r \leq a \\ -\sigma_0 & , \quad a \leq r \leq c \end{cases} \qquad (1.2.18)$$

where σ_0 is the maximum force between the two elastic bodies predicted by the Lennard-Jones potential. Maguis also proposed a parameter λ which is equivalent to the Tabor parameter:

$$\lambda = \sigma_0 (\frac{9R}{2\pi\gamma E^{*2}})^{\frac{1}{3}} = 1.16\mu \qquad (1.2.19)$$

Carpick, Ogletree and Salmeron (1999) proposed a simple equation to find the contact radius as below [9]:

$$a = a_0(\beta)(\frac{\beta + \sqrt{1 - F/F_{po}(\beta)}}{1+\beta})^{\frac{2}{3}} \qquad (1.2.20)$$

Where a is the contact radius when $F = 0$, β is a parameter related to λ by

$$\lambda = -0.924 \ln(1 - 1.02\beta) \qquad (1.2.21)$$

$\beta = 1$ corresponds to the case of JKR model and $\beta = 0$ corresponds to DMT model.

Besides the models introduced above, there are still a lot more models used in practical cases, for example, the Bradley model for rigid contact and Sneddon model for soft materials. However, due to the space limitation, we do not discuss these models in this thesis. Another essential point we need to remark here is that all the mentioned models in this thesis are only valid for isotropic bodies. As a matter of fact, there's no analytical model for anisotropic materials, even for the simplest case – orthotropic materials.

1.3 Atomic Force Microscopy

Atomic force microscopy (AFM) belongs to the category of Scanning Probe Microscopy (SPM) [10], which means the information of the surface (topography, force, etc.) is collected by "feeling" or "touching" the surface with a probe. Compare with another member of the SPM family– Scanning Tunneling Microscopy (STM) [11], which gathers information of the surface by the tunneling current through the conductive sample to the probe in vacuum, AFM is able to measure both conductive and non-conductive materials and can be performed in air and even in liquid. The first AFM was invented in 1982 by IBM and then implemented to practical experiments in 1986 by Bining, Quate and Gerber [3].
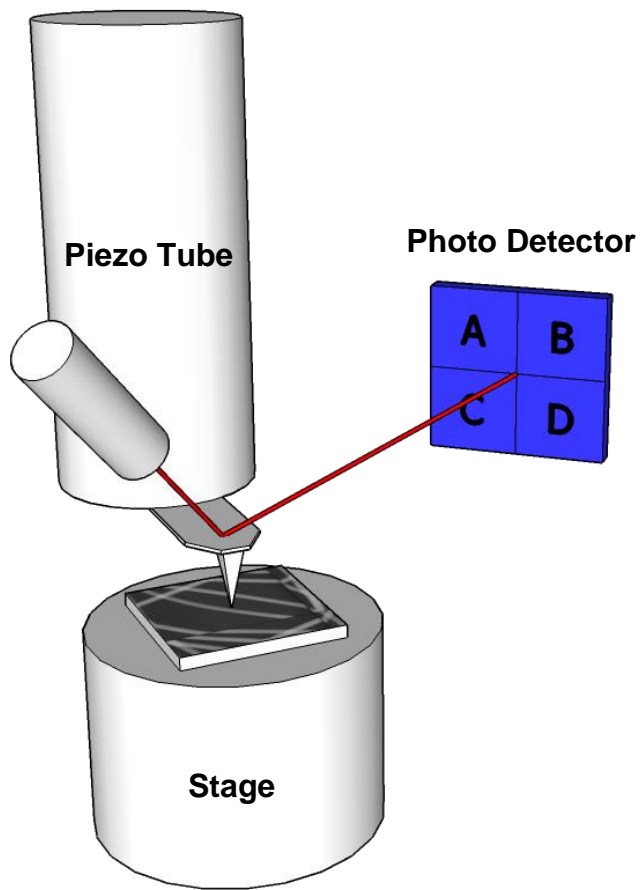
Figure 1.3.1: Scheme of the configuration of an AFM. The piezo tube controls the movement of the probe in the X - Y plane and the vertical Z direction. . A laser is projected on the backside of the cantilever and reflected to a photodetector. The bending and torsion of the cantilever then can be obtained by the position of the laser spot on the detector.

1.3.1   Basic Configuration

Figure 1.3.1 shows the basic configuration of a typical AFM. The AFM probe is made up of two parts: the long-arm cantilever and an apex (facing to the sample) on the end of the cantilever. Interactions between the apex and the sample surface make the cantilever deform both vertically and laterally. The normal/vertical force acting on the apex of the probe causes the bending of the cantilever and the lateral force causes the torsion of the cantilever. To detect the deformation of the cantilever, a laser beam (usually red laser) is projected on the backside of the cantilever, which is usually coated with reflective metal such as Al to enhance the reflection rate and therefore increase the overall sensitivity. The laser is then reflected to a four-quadrant position sensitive photo-detector as shown in Fig. 1.3.1. The sum and position of the laser spot on the detector can be used to determine the deformation of the cantilever quantitatively. The bending of the cantilever makes the position of the laser reflection change vertically (up and down) on the detector while the torsion of the cantilever makes the laser deflection change laterally (left and right) on the detector. Therefore, the vertical bending and lateral torsion are proportional to the two following quantities:

$$
\begin{cases}
bending \propto \dfrac{(A+B)-(C+D)}{A+B+C+D} \\[4mm]
lateral \propto \dfrac{(A+C)-(B+D)}{A+B+C+D}
\end{cases}
\qquad (1.3.1)
$$

(A+B) − (C+D) and (A+C) − (B+D) are usually termed as *deflection/vertical* and *lateral/friction* in most commercial AFMs, respectively.

The photodetector has a spatial resolution of 1 nm. Considering the mechanical amplification of the laser-cantilever-detector system, the vertical resolution of an AFM system can reach as high as sub-Å scale.

A piezoelectric tube, which expands and contracts proportionally to applied voltage, is used to control the movement of the probe in X-, Y- and Z-direction by applying voltages to deform the tube while the sample remains still as shown in Fig. 1.3.1. In some other AFM systems, the piezo tube is attached to the sample stage so that sample stage moves while the probe keeps unmoved. The two setups are apparently equivalent.

There are plenty of AFM modes developed and used nowadays for a variety of applications. The key factor to differ those AFM modules is the signal used for the feedback loop. In the following sections, we will briefly introduce several most commonly used modes and their working mechanisms.

1.3.2 Contact Mode

The simplest and most popular mode is called *contact mode*. As its name shows, in contact mode, the probe is in the contact regime with the sample surface. In contact mode, a feedback loop keeps the deflection signal constant, i.e., the normal force applied on the cantilever. It's also called *constant force mode*. While the probe is in physical contact with the sample surface under a certain normal force, the cantilever is bent substantially; as the scanner gently traces the probe across the sample (or the sample under the probe), the contact force causes the cantilever to bend more (for high features) or less (for low features or holes) to accommodate the changes in topography. Due to the presence of feedback loop

which maintains a constant bending/force of the cantilever, the piezo tube then will adjust the relative height of the probe/sample to compensate for topographical features.

Now let's discuss the physical nature of the probe – sample interaction. When the probe is brought within 1 nm above the sample surface, the interacting forces can be approximated by the Lennard-Jones potential [12]:

$$V(r) = 4\varepsilon[(\frac{\sigma}{r})^{12} - (\frac{\sigma}{r})^{6}] \qquad (1.3.2)$$

where r is the distance between atoms, ε is the depth of the potential well and σ is the distance where the inter-atom potential is zero. The behavior of the Lennard-Jones potential is shown in Fig. 1.3.2. The first term is the repulsive electrostatic interaction due to the electron orbital overlapping at short range. The second term is the van der Waals energy, describing the long-range attractions. As shown in Fig. 1.3.2, when two atoms are far from each other, the two-atom system's energy is negative which means there is weak attractive interaction between the two atoms. While the two atoms are brought closer to each other, the van der Waals attraction gets stronger and the energy reaches a minimum value. If the atoms are getting closer, the first repulsive term (Pauli repulsion) becomes dominant over the second term (van der Waals). As we can see from Fig 1.3.2, the repulsive interaction increases rapidly in the contact regime. As a result, the extremely strong repulsive force will resist almost any force that attempts to push the atoms closer. In the contact mode the cantilever pushes the apex against the sample with a relatively large normal force, so contact mode is usually working in the repulsive regime as shown in Fig. 1.3.2.

The lateral torsion of the cantilever is caused by the frictions between the tip and sample surface. Indeed, the lateral signal is proportional to the friction force between the probe and sample. Therefore, contact mode AFM is the most powerful tool for the tribological study at the nanoscale.
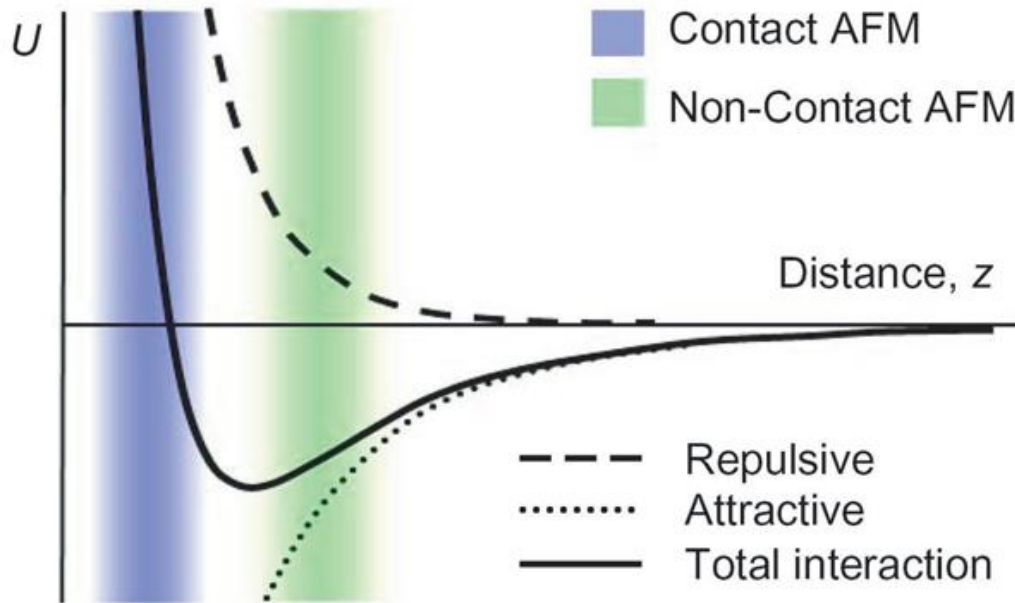
Figure 1.3.2: The Lennard-Jones Potential diagram.

Image taken from: www.parkafm.com.

1.3.3   Non-contact/Tapping Mode

The contact mode makes hard physical contact between the probe and sample and drags laterally while scanning and it can damage the sample surface, especially soft materials like polymer and biological materials. Furthermore, contact mode is not sensitive

to rapid topographical change. On the opposite, *non-contact mode* or *tapping mode* are non-destructive and have even higher resolution and more functionalities [13].

In the non-contact/tapping mode, a stiff (much stiffer than the contact mode probe) cantilever is vibrated by a piezo at or near the cantilever resonance frequency, the oscillation amplitude is from a few nanometers (for non-contact mode) to several hundred nanometers (for tapping mode). In tapping mode, the driving frequency and amplitude are kept constant and used for feedback signal. When the probe is brought close to the sample surface, the van der Waals interaction (attractive) will slightly change the resonance frequency of the cantilever as shown in Fig. 1.3.3, as result, the corresponding driving amplitude will decrease. The feedback loop will then adjust the relative height of the probe so that the frequency or amplitude to the original value when the probe and sample are far away. Most commercial AFM uses the amplitude as the feedback signal, which is the amplitude modulation (AM) mode; but sometimes frequency modulation (FM) is also used.

Non-contact/tapping mode not only can give higher quality topographical image, but can also reveal more information about the sample than contact mode. Phase Imaging is a derivative mode of dynamic mode AFM (tapping mode and non-contact mode). The phase of the cantilever oscillations θ, measured relative to the drive signal of the piezoelectric crystal, has turned out to be a powerful signal for studying the properties of the sample surface. The phase image contains the information about the molecule structure, surface charge distribution, elastic properties and etc. The information hidden in the phase image is so rich and complicated that extensive studies are still undergoing.
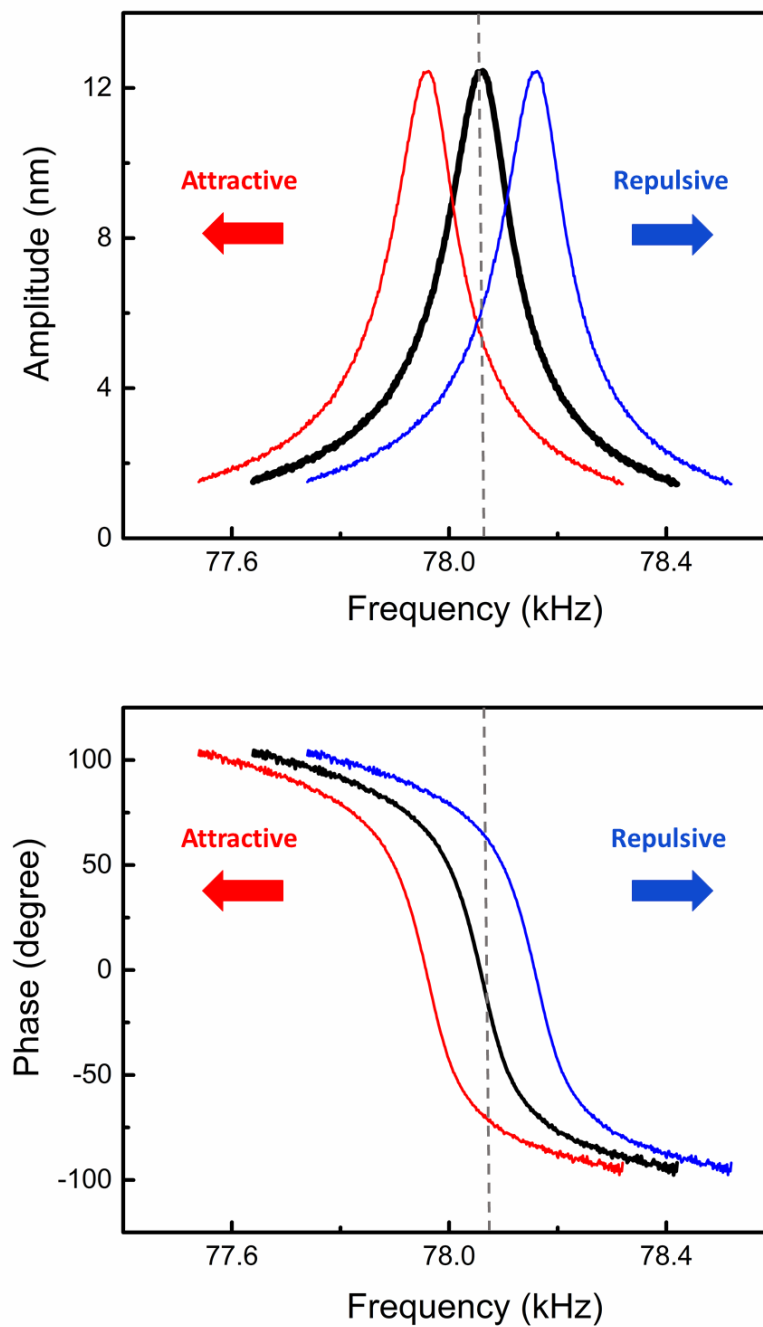
Figure 1.3.3: Resonance frequency tune of an AFM probe. Top: amplitude vs. drive frequency. Bottom: phase vs. drive frequency. Both attractive and repulsive interaction between the probe and sample will decrease the driving amplitude.

Besides contact/non-contact modes, people have been developing new modules for electrical and electronic characterization of materials besides the basic topographical imaging. These new AFM modules include Conductivity (or Current) AFM (C-AFM) [14], Electrostatic Force microscopy (EFM) [15], Kelvin Probe Force Microscopy (KPFM) [16], and Magnetic Force Microscopy (MFM) [17]. These secondary modules have been widely used to investigate material's dielectric constant, work function, magnetism and other related properties. Again, due to the limitation of space, we will not discuss these AFM modules in this thesis.

CHAPTER 2.   TWO-DIMENSIONAL MATERIALS

Two-dimensional material, consisting of only one-atomic layer in thickness (as shown in Fig. 2.1.1), has attracted people's interests both in academic and industrial fields due to its unique two-dimensionality and corresponding outstanding properties [18-26]. For example, 2D material is naturally a perfect two-dimensional electron gas system, therefore enormous studies have been done on the novel Quantum behavior on 2D materials at low temperature and high magnetic field. Till now, (room-temperature) Quantum Hall Effect [27, 28], Fractional Quantum Hall Effect [29] and other novel physical behaviors [30] have been predicted and successfully observed. In this Chapter, we briefly review the recent progress of the research about the structures, properties and applications of several typical 2D materials, including graphene, graphene oxide (GO) [31-34], Transition Metal Dichalcogenides (TMDs) [20, 35-37], etc.

2.1   Graphene

2.1.1   Basic Properties

Graphene, first found in 2004 [38, 39], is the most well-known and widely studied member of 2D materials family. Graphene is a flat monolayer of carbon atoms tightly packed into a two-dimensional (2D) honeycomb lattice or can simply be considered as one layer of graphite. Graphene is a basic building block for graphitic materials of all other dimensionalities (Fig. 2.1.1). It can be wrapped up into 0D fullerenes, rolled into 1D nanotubes or stacked into 3D graphite [18].

For graphene, each carbon atom is covalently bonded with its three neighbors with three σ bonds and another π-bond is oriented out of plane. Actually, the electron orbitals
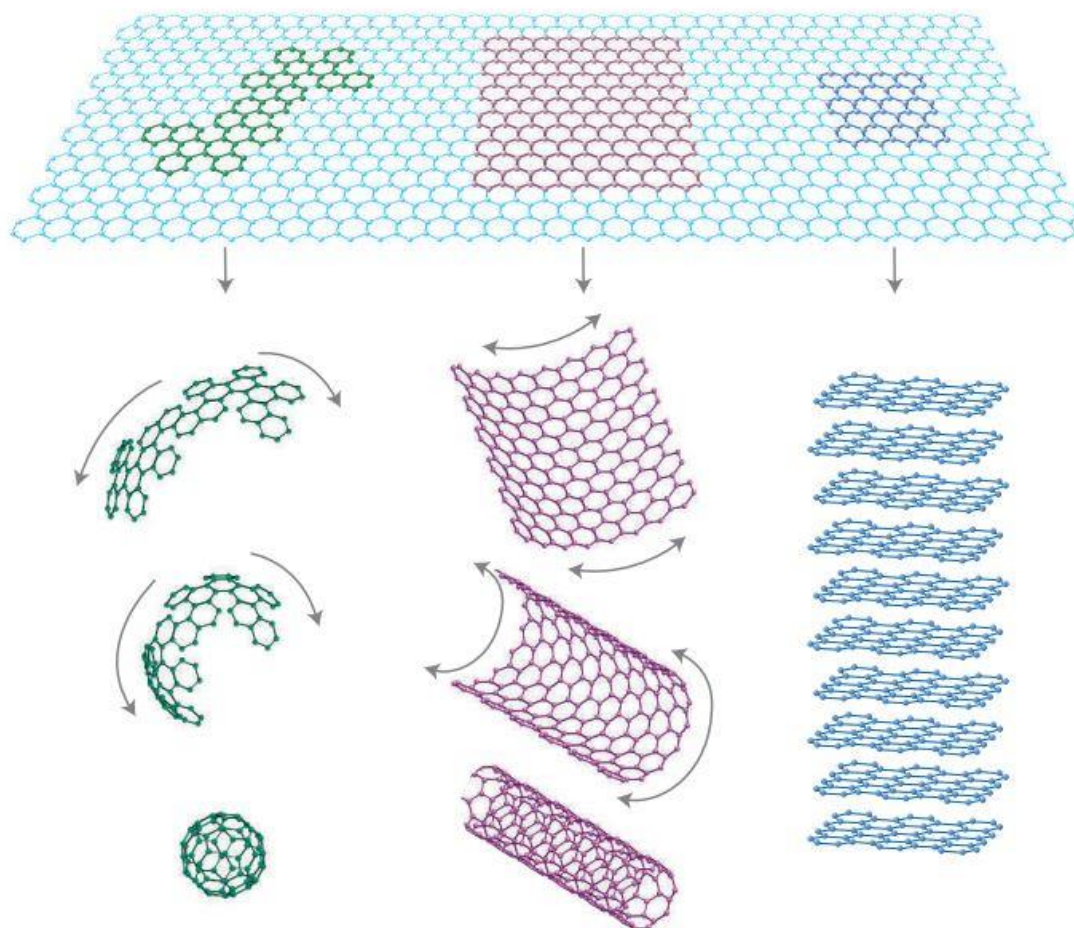
Figure 2.1.1: Graphene is a 2D building material for carbon materials of all other dimensionalities. It can be wrapped up into 0D fullerenes, rolled into 1D nanotubes or stacked into 3D graphite. Reprinted with permission from [18]. Copyright 2007, Nature Publishing Group.

are sp^2 hybridized – a combination of orbitals s, p_x and p_y that constitute the σ-bond. The rest p_z electron makes up the π-bond. The π-bonds hybridize together to form the π-band and π∗-bands. Graphene is a zero-gap semiconductor since the conduction and valence bands meet at the Dirac points of the 2D Brillouin zone as shown in Fig. 2.1.2. More interestingly, the equation describing the electrons' energy dispersion relation near Dirac point in graphene is:

$$E = \hbar v_F \sqrt{k_x^2 + k_y^2} = \hbar v_F k = v_F P \tag{2.1.1}$$

where the k is the wave vector, v_F is the Fermi velocity. Based on Eq. 2.1.1, the dispersion relation is linear thus the effective mass of the electrons in graphene near Dirac point is zero. Consequently, at low energies, even neglecting the true spin, the electrons in graphene can be described by an equation that is formally equivalent to the massless Dirac equation. Hence, the electrons and holes in graphene are both considered as Dirac fermions.

Graphene has outstanding mechanical, electronic, optical and thermal properties, thus holds great promise for a wide range of applications. The intrinsic strength of monolayer graphene is as high as 130 GPa [40]. This ultra in-plane stiffness is due to the sp^2 bonds, one of the strongest covalent bonds we ever know. Furthermore, graphene displays remarkable in-plane electron mobility at room temperature, with reported values of 15000 $cm^2 \cdot V^{-1} \cdot s^{-1}$[18]. Scattering by graphene' acoustic phonons intrinsically limits room temperature mobility to 200000 $cm^2 \cdot V^{-1} \cdot s^{-1}$ at a carrier density of 10^{12} cm^{-2} [41]. The corresponding resistivity of graphene sheets is ~ 10^{-6} Ω·cm, lower than that of silver, but still one of the lowest ever known at room temperature. Due to its exceptional electronic properties, graphene can be used in making large-scale CMOS [42], high-performance field

effect transistors (FETs) [22, 26, 38, 43], supercapacitors [44, 45], etc. Besides mechanical and electronic properties, the thermal conductivity of graphene is as high as 5300 W/mK [46] and opacity is also unexpectedly high [47].
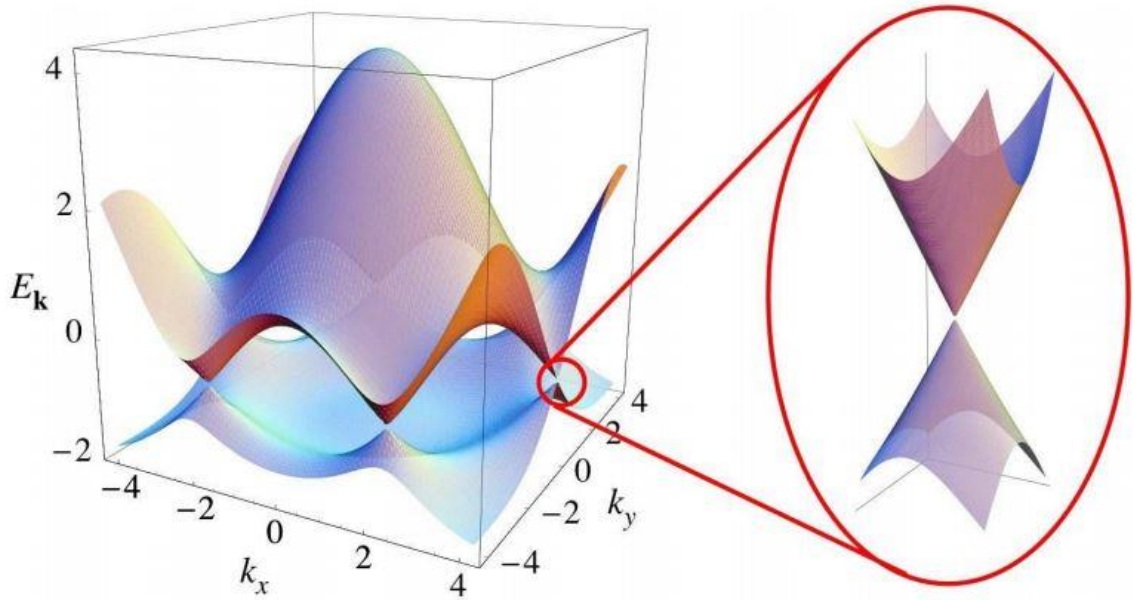
Figure 2.1.2: Band structure of graphene. The bandgap is zero at Dirac points. Reprinted with permission from [26]. Copyright 2009, American Physical Society.

2.1.2 Epitaxial Graphene

There are several mainstream graphene synthesis methods, including mechanical exfoliation (the "scotch tape" method) [38], chemical vapor deposition (CVD) [48, 49] and also epitaxial growth from SiC [23, 24, 50]. The mechanical exfoliation method is quite simple: first separating graphene films from bulk graphite using adhesive (scotch) tape and then transferring to other substrate like SiO_x/Si. The mechanical exfoliation method was invented by Novoselov and Geim in 2004 to get the first single layer graphene and indeed is still probably the most popular graphene preparation methods in research field nowadays due to its simplicity and low cost [38]. In contrast to its extreme simplicity, the graphene obtained via mechanical exfoliation has very high mobility and small amount of defects. However, the size control is extremely challenging thus the reliability of the mechanical exfoliation method is limited.

De Heer *et al*. found that graphene layers could be epitaxially grown on SiC by annealing 4H/6H SiC at temperature higher than 1200°C and at low pressure (10^{-6} Torr) [23, 24, 39, 51]. In this case, the Si atoms will evaporate and the remaining Carbon atoms on the SiC surface will reconstruct and form graphene layers as shown in Fig. 2.1.3. This graphene is termed as epitaxial graphene (EG). EG can be grown on both polar faces of SiC, which are denoted as Carbon-terminated face (000-1) and Silicon-terminated face (0001). Epitaxial graphene grows much faster on the C-face than Si-face, thus few-layer graphene (FLG) is usually grown on the Si-face while multi-layer graphene (MLG) is on the C-face as shown in Fig. 2.1.4. More details about the epitaxial growth methods can be found in [23, 24, 51]. Compared with exfoliated graphene, EG's number of layers is much more controllable. Besides, EG can be grown homogeneously on SiC with large area and

high quality. Last but not least, while the exfoliated graphene has to be transferred to a substrate during which contaminants and defects might be introduced into the graphene layers, SiC itself is a good substrate for electronic device applications, thus no transfer is needed. The purity and high quality can be maintained. Based on the reasons above, we mainly studied EG instead of exfoliated flake graphene in this thesis.
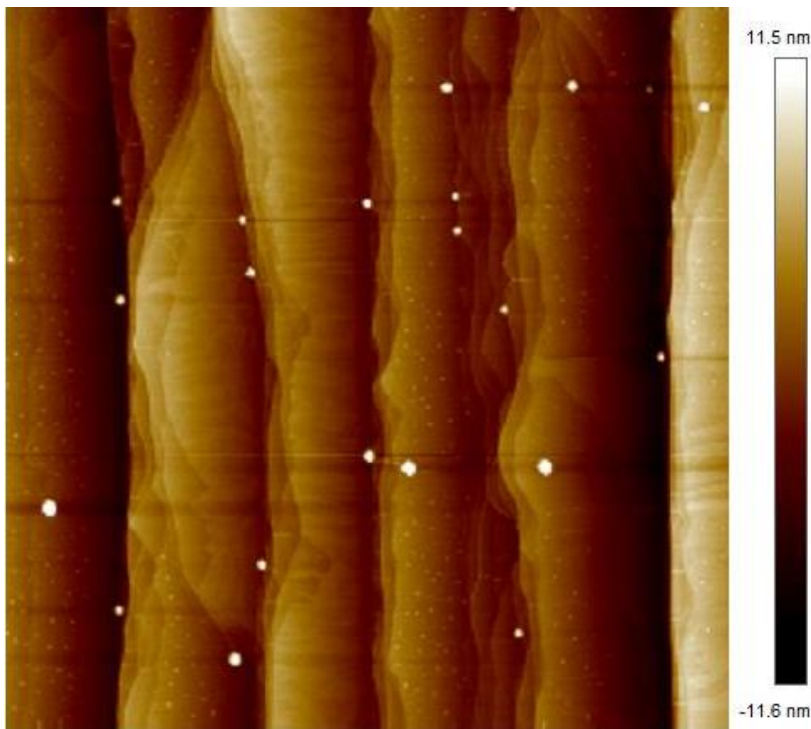
Figure 2.1.3: AFM topographic image of epitaxial graphene on SiC (0001). The vertical stripes are SiC steps formed during the annealing and graphene is uniformly distributed on those SiC steps. The image size is 10 μm.
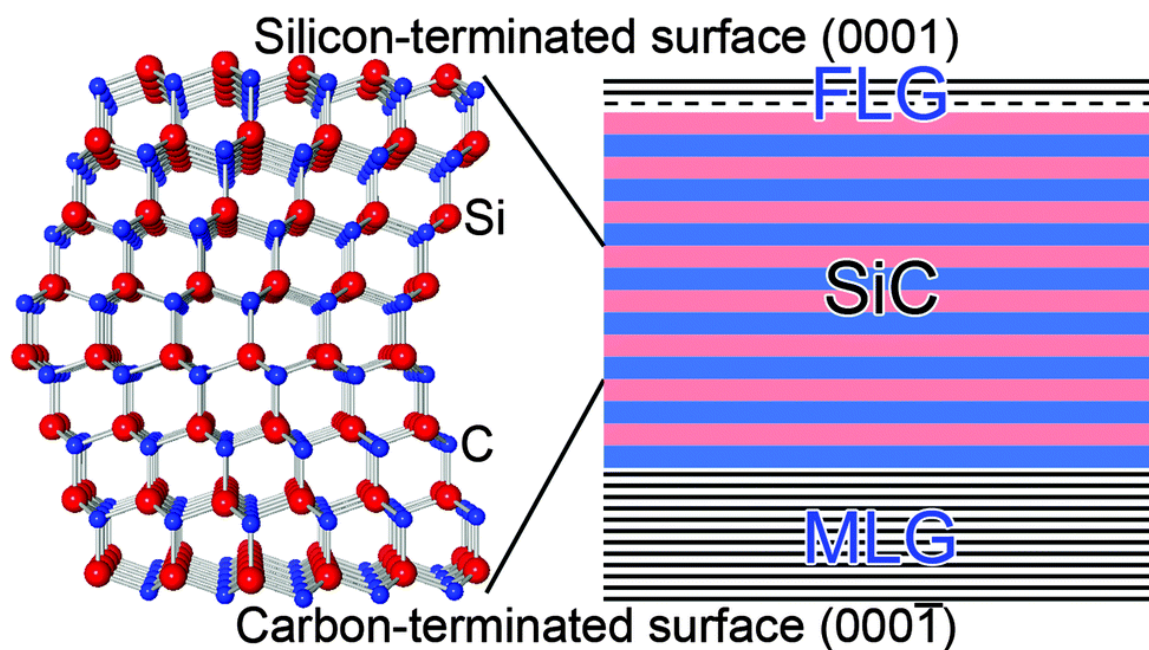
Figure 2.1.4: Schematic diagram of epitaxial graphene grown on the Si-terminated surface (0001) and Carbon-terminated surface (000-1) of 6H-SiC. Reprinted with permission from [50]. Copyright 2014, Royal Society of Chemistry.

2.2   Graphene Oxide

2.2.1   Basic Properties

Graphite oxide is a compound of carbon, oxygen, and hydrogen in variable ratios, obtained by treating graphite with strong oxidizers [34, 52, 53]. The bulk material disperses in basic solutions to yield monomolecular sheets, termed as graphene oxide (GO).

The most common method for synthesizing graphene oxide is the Hummers' method which treats graphene with a mixture of H_2SO_4, $NaNO_3$, and $KMnO_4$ [52]. The graphene films are usually oxidized with hydroxyls (-OH), epoxides (-O-), carbonyls (C=O) and other functional groups as shown in Fig. 2.2.1.
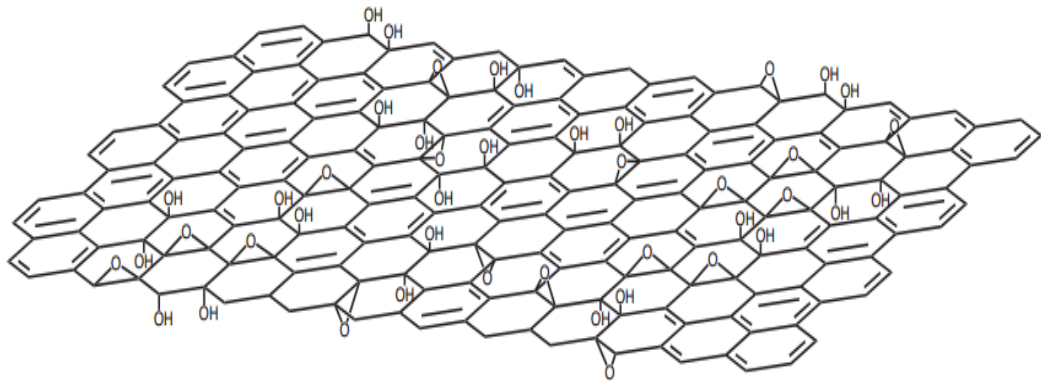
Figure 2.2.1: Schematic diagram of graphene oxide structure. Reprinted with permission from [53]. Copyright 2009, Nature Publishing Group.

Like graphene, GO also inspired a wide range of applications. For example, GO itself is an insulator thus we can use GO as a reduction precursor for engineering and manipulating graphene electronics [25, 54]. GO can also be used for water purification [55,

56], high-rate lithium batteries [57] , optical devices [58] and mechanical actuators [59]. GO is also reduced to prepare large scale graphene sheets [53].

2.2.2   *Epitaxial Graphene Oxide*

Epitaxial graphene oxide (EGO) can be synthesized from epitaxial graphene with mild Hummers' method, which avoid graphene exfoliation and dispersion in solution [31, 60]. Once the reactions are terminated, EGO films on the SiC chips are picked up from solution and rinsed with deionized water and then blown-dried with nitrogen gas. Both experimental and theoretical studies have revealed that the interlayer distance increases from 3.4 Å of EG to 9.3 Å of EGO due to the intercalation of water molecules [60].

2.3   **Other 2D Materials**

Besides graphene and its close relative graphene oxide, other 2D materials have been obtained and studied nowadays, including Hexagonal Boron Nitride (h-BN), Transition Metal Dichalcogenide (TMD), Phosphorene, etc.

2.3.1   *Hexagonal Boron Nitride (h-BN)*

Hexagonal boron nitride (h-BN) has a layered structure similar to graphene. Within each layer, boron and nitrogen atoms are bound by strong covalent bonds, whereas the layers are held together by van der Waals forces. The interlayer "registry" of these sheets differs from graphene, because the atoms are eclipsed, with boron atoms lying over and above nitrogen atoms [61-63]. Even though they share similar hexagonal structure, h-BN have very different properties from graphene. For example, h-BN is purely insulating while

graphene is semi-metal. Hexagonal BN can be used as the substrate for high-quality graphene electronics [61].

2.3.2   Transition Metal Dichalcogenides (TMDs)

Transition metal dichalcogenide (TMD) are semiconductors of the type MX_2, with M a transition metal atom (Mo, W, etc.) and X a chalcogen atom (S, Se, or Te) [35, 37, 64-66]. One layer of M atoms is sandwiched between two layers of X atoms as shown in Fig. 2.3.1.
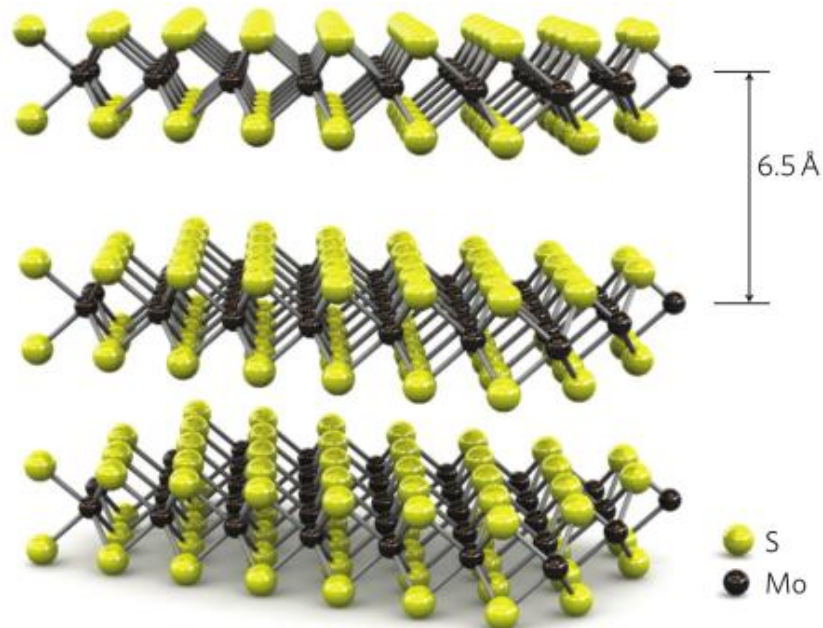
Figure 2.3.1: MoS_2 atomic structure. Reprinted with permission from [37]. Copyright 2011, Nature Publishing Group.

Graphene has exceptional electronic properties as we discussed in section 1.1.1. However, single-layer graphene does not have a band-gap, which means all the semiconductor devices such FETs cannot be built on graphene. Monolayer TMDs, which have direct band-gap (for example, 1.8eV for MoS_2) [37], are indeed one of the substitutes of graphene in band-gap engineering and device applications. Furthermore, owing to the direct band gap, TMDs are also perfect candidates for optoelectronic devices. MoS_2 have been used as a phototransistor [67] and ultrasensitive bio-detectors [68].

2.3.3 Phosphorene

Phosphorene is a single layer of black phosphorus, much in the same way that graphene is a single layer of graphite. Phosphorene is predicted to be a strong competitor to graphene because, in contrast to graphene, phosphorene has a band gap. Phosphorene was first isolated in 2014 [69-71] by mechanical exfoliation and has become one of the most attractive members among the whole 2D materials family [69-76]. Unfortunately, due to its instability (phosphorene reacts fast with oxygen and water) in air at room temperature, challenges still remain with phosphorene related research and applications.

CHAPTER 3.   INSTRUMENTATION: MODULATED NANO-INDENTATION (MONI)

3.1   State of the Art

3.1.1   Traditional Nano-indentation for Micro-hardness Measurements

The traditional nano-indentation technique was originally developed in the mid-1970s to determine the hardness of bulk materials [77]. During a traditional indentation test (macro or micro indentation), a hard tip (usually made of or coated with diamond) is indenting into the unknown objective material with an increasing normal load which is controlled by the user. The force-displacement is then recorded. Figure 3.1.1 is a schematic diagram of a force-displacement curve. For a nano-indentation (or micro-indentation), the normal load is usually relatively large (larger than $1\mu N$) so the deformation lies into the regime of plastic deformation. As we introduced in section 1.1.3, a permanent deformation will remain even after the external force disappears. Therefore, the loading and unloading curves usually do not overlap as shown in Fig. 3.1.1. Furthermore, the nano-indentation method usually makes a residual hole with a certain depth h on the sample surface as shown in Fig. 3.1.2. If the maximum load is F_{max} and the area of residual hole is A, then the hardness of the material can be defined (there are other hardness definitions based on the methods, but we only introduce this definition for simplicity) as:

$$H = \frac{F_{max}}{A} \tag{3.1.1}$$
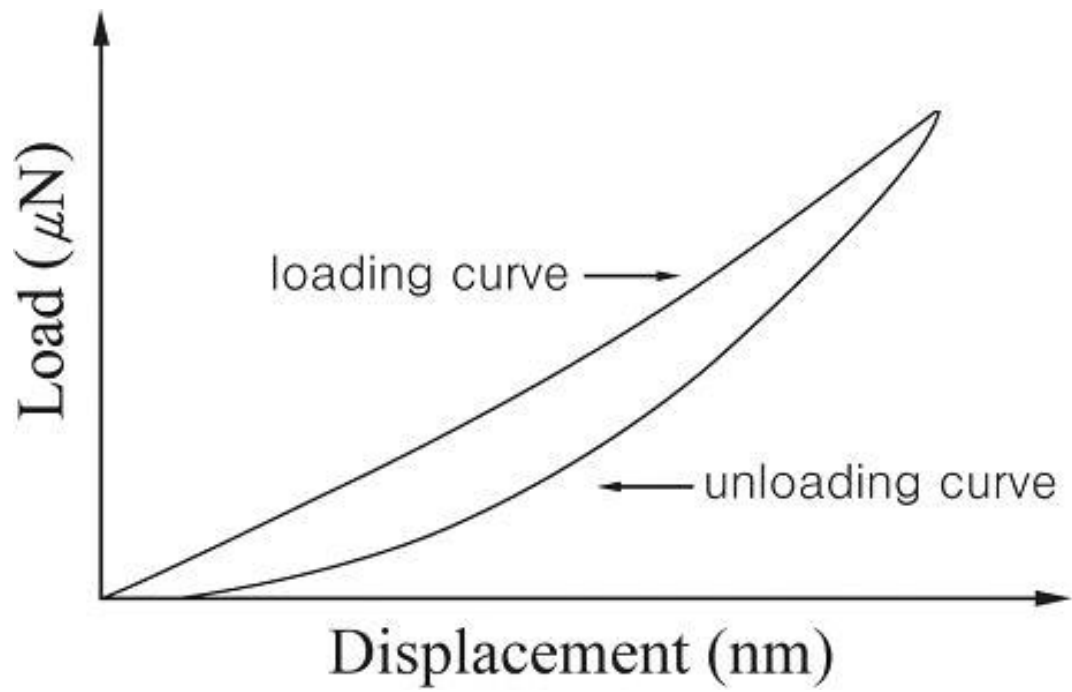
Figure 3.1.1: Schematic diagram of force-displacement curve of nano-indentation. The loading and unloading curves show a hysteresis behavior.
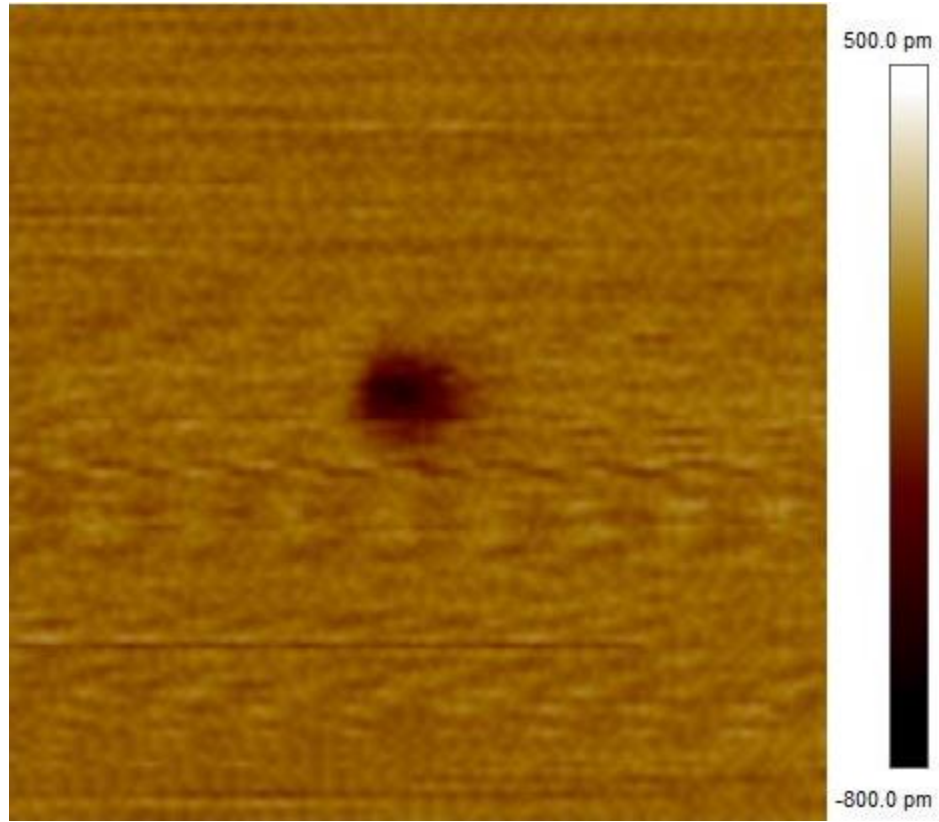
Figure 3.1.2: AFM topographic image of the residual hole after nano-indentation measurement on SiC with a diamond indenter. The image size is 400nm.

3.1.2 Traditional Nano-indentation on Supported Thin Films

Traditional nano (micro) indentation technique has also been widely used to investigate the mechanical properties of thin film coating supported on rigid substrate [78-82]. Similar to the micro-hardness measurements as introduced in *3.1.1*, nano-indentation technique can also be used to measure the effective hardness of thin film/substrate composites, as long as the indentation depth is large enough to cause plastic deformation. If the indentation is down to the nm-scale such that the deformation lies in the linear or elastic regime, one can study the elastic properties of the thin film coating and the composites. Figure 3.1.3 shows indentation curves of SiO_2 coating with different thicknesses on Si substrate [82]. The effective Young's modulus of the composites can be extracted from the beginning part (indentation depth < 10nm) of the indentation curve when the deformation is still elastic. If we keep indenting until the indentation depth is comparable with the film thickness, the substrate effect is apparently not negligible and plastic deformation becomes dominant [81]. As a matter of fact, the traditional nano-indentations (performed by nano- or micro-indenter) will measure only the substrate when the coating film gets down to a few nanometers thick. Furthermore, if the coating film is layered materials, the information of the inter-layer van der Waals interactions is completely lost.
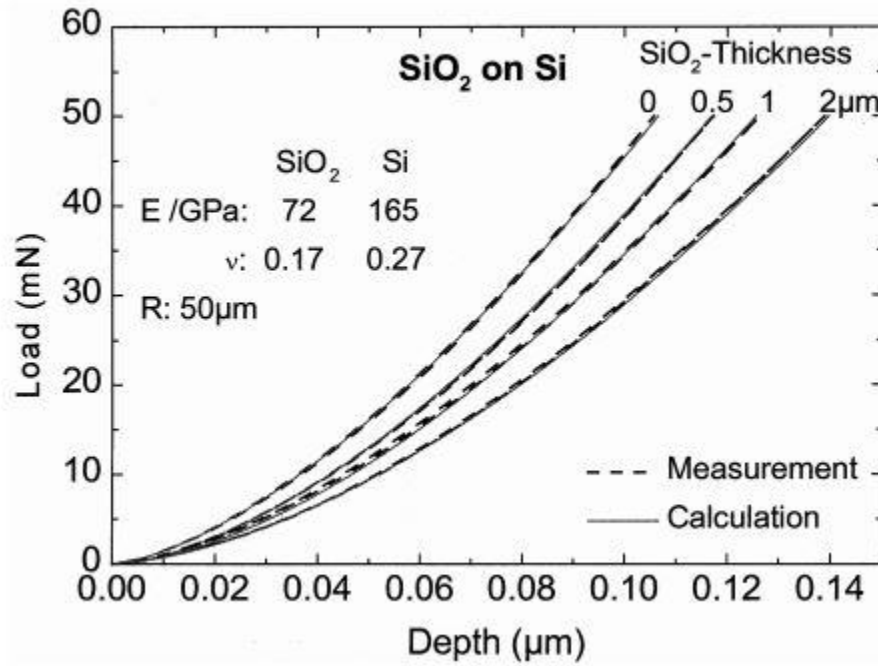
Figure 3.1.3: Comparison of calculated to measured load-depth data for SiO_2 on Si for different film thickness values. The elastic parameter for the calculation are given in the figure. Reprinted with permission from [82], Copyright 1999, Elsevier.

3.1.3   AFM Based Nano-indentation on Suspended Thin Films

Traditionally, nano-indentation was performed with a micro-indenter. Apparently, atomic force microscope (AFM) can be directly applied to perform nano-indentation measurements [83, 84]. Besides, with a much higher capability to apply nanoscale force and control the vertical displacement at higher resolution, AFM can not only measure the hardness but also other mechanical properties like the elastic/shear modulus. Actually, scientists have already used AFM to measure the in-plane Young's modulus of two-dimensional (2D) materials, which is defined as the material with only one-atom-layer thickness [40, 66]. 2D materials display extraordinary mechanical, electronic, optical and thermal properties due to its unique geometry structure [18]. More detailed introductions of 2D materials can be found in Chapter II.

Figure 3.1.4 shows a typical setup of AFM based nano-indentation on 2D material. A 2D membrane is suspended on open holes and the mechanical properties of the free-standing films were probed by indenting the center of each film with an AFM by collecting a force-distance curve on the free-standing 2D film. The stress-strain relationship is:

$$\sigma = E\varepsilon + D\varepsilon^2 \tag{3.1.2}$$

where σ is the symmetric second Piola-Kirchhoff stress, ε is the uniaxial Lagrangian strain, E is the Young's modulus, and D is the third-order elastic modulus. The value of D is typically negative, so the presence of the second-order term leads to a lessening of stiffness at high tensile strains and an increasingly stiff response at high compressive strains. Then the force-displacement relationship is given as:

$$F = \sigma_0 (\pi a)(\frac{\delta}{a}) + E(q^3 a)(\frac{\delta}{a})^3 \qquad\qquad (3.1.3)$$

where F is applied force, δ is the deflection at the center of the 2D film, σ_0 is the pretension in the film, a is the diameter of the hole underneath the 2D film and $q = 1/(1.05 - 0.15v - 0.16v^2)$ is a dimensionless constant where v is the Poisson's ratio of the 2D film. A typical force-displacement curve is shown in Fig. 3.1.5.

AFM − based nano-indentation has been proven to be a powerful tool to measure the mechanical properties of 2D materials. For example, the Young's modulus of graphene film was measured by AFM nano-indentation, and its value is 1 TPa, one of the most stiff materials ever known [40]. However, most AFM nano-indentation measurements caused large deformation (larger than 10nm as shown in Fig. 3.1.5) on free-standing 2D films. Furthermore, all these measurements considered the 2D film as an isotropic material. As a result, the normal force is burdened by the in-plane covalent bonds and the obtained "Young's modulus" is actually the in-plane elastic modulus $E_{//}$. As we have discussed in this chapter, 2D material is transversely-isotropic. Previous AFM nano-indentation is unable to extract information of another important elastic constant − the out-of-plane elastic modulus $E_{\perp}$, which corresponds to the inter-layer van der Waals interactions. In the following sections, we introduce a new AFM based indentation technique - MoNI, which allows for extremely small deformation so that the out-of-plane modulus $E_{\perp}$ can be investigated thoroughly [85].
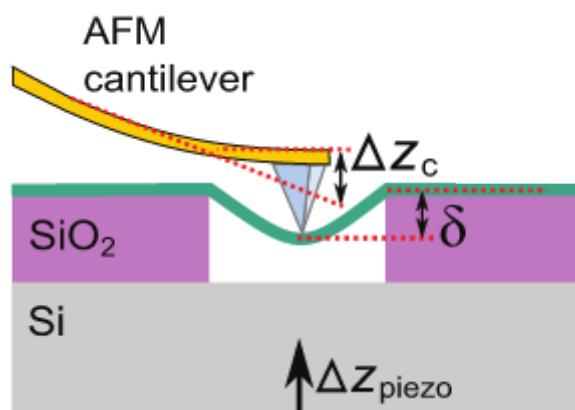
Figure 3.1.4: Schematic diagram of AFM nano-indentation on free-standing 2D film. Reprinted with permission from [66], Copyright 2012, Wiley Online Library.
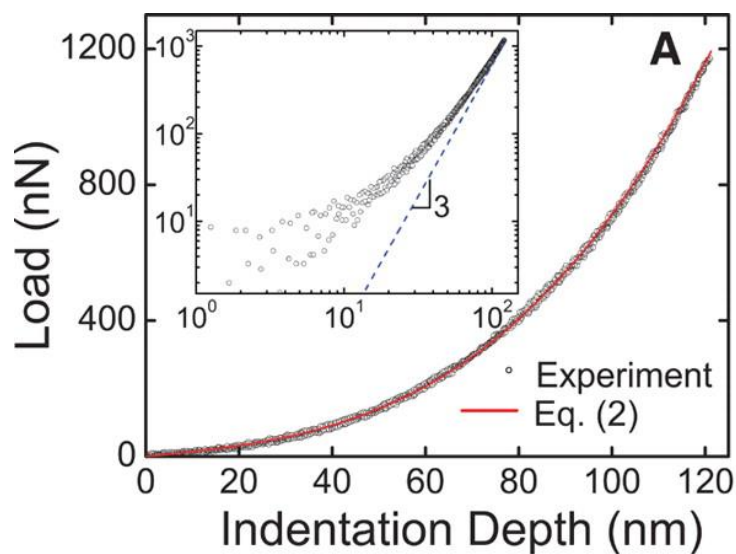
Figure 3.1.5: Indentation curve of a diamond AFM probe on free-standing monolayer graphene film. Reprinted with permission from [40], Copyright 2008, AAAS.

3.2 MoNI Experimental Setup

3.2.1 Basic Introduction

As discussed above, most AFM based nano-indentation measurements directly acquire indentation curves of 2D films by indenting the free-standing materials with a relatively large deformation (above 10nm) so the 2D films are usually severely stretched "in-plane". Consequently, the indenting normal force is mainly burdened by the in-plane covalent bonds while the out-of-plane inter-layer interaction has infinitesimal contribution to the total indentation curve (A back-of-the-envelope model to demonstrate this point can be found in section 4.2). Nano-indentation is thus able to measure the in-plane Young's modulus but not sensitive to the inter-layer van der Waals interaction of 2D materials. Besides, with such large deformation, the best achieved vertical resolution is only 1nm and the 2D films might even be damaged.

Here we introduce a novel AFM based sub-Å resolution indentation technique – *Modulated Nano-indentation (MoNI)* [85-88] but we also call it "Å – Indentation" to better reflect its extremely high resolution (sub-Å) and outstanding ability to investigate the inter-layer interactions and probe – sample surface phenomena at Å-scale. In the rest of this thesis we still call this technique as "MoNI".

Three key features of MoNI shall be emphasized: (1) the indentation depth is as small as 1Å, (2) the measured materials need to be supported on a rigid substrate to maintain small deformation and avoid vibrations, (3) MoNI is especially sensitive to the inter-layer interaction and the in-plane interactions are negligible.
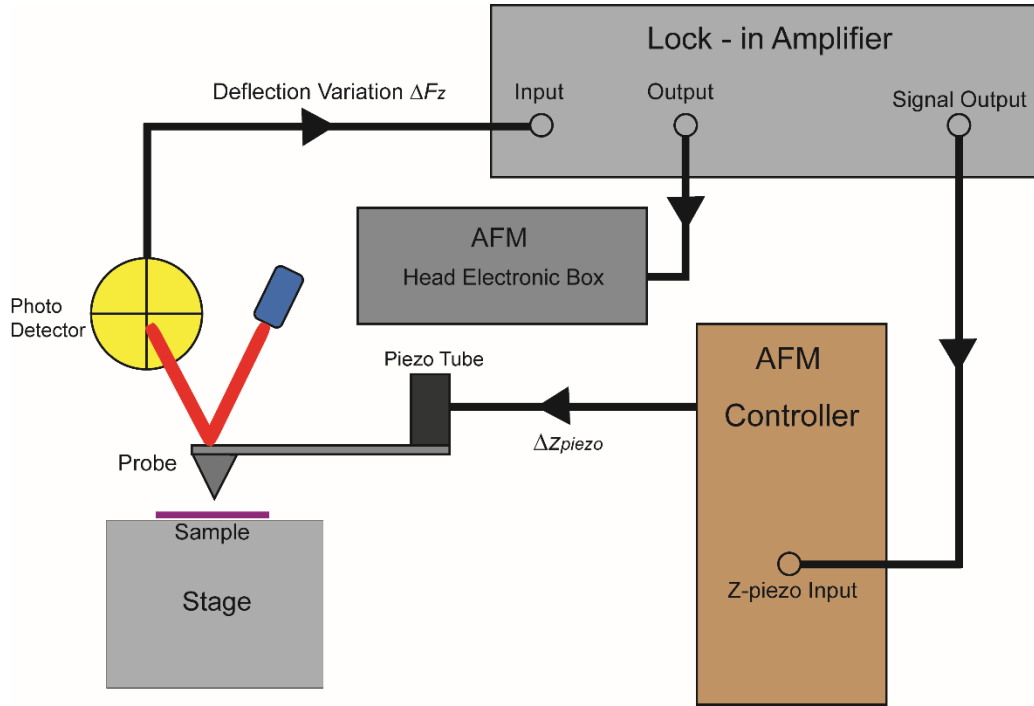
Figure 3.2.1: A schematic representation of the setup of MoNI.

All the MoNI measurements in this thesis were carried out on a homemade system based on the Contact Mode of Agilent PicoPlus AFM as shown in Fig. 3.2.1. Before starting a MoNI experiment, a frequency sweep is crucial to find the resonance frequencies of the AFM piezo tube f_{piezo} (not the cantilever resonance frequency). Then we make sure the frequency f of the oscillations, which are applied to the AFM probe via the piezoelectric

stage rigidly attached to the AFM cantilever-tip system, is far from f_{piezo}. Avoiding f_{piezo} allows for extremely small oscillations (~ 0.1 Å) and shallow indentation depth (< 1 Å), as well as to remain in the linear regime. For all the MoNI measurements reported in this thesis we used $f = 0.991$ kHz. The oscillations are controlled by a Lock-in amplifier (Stanford Research Systems, SR830) and the normal force F_z between the probe and sample is maintained constant by the feedback loop of the AFM. By working with a constant force, any thermal drift is avoided.

During the measurements, the driving piezo-stage oscillation amplitude Δz_{piezo} is fixed and equal to the sum of the cantilever bending and probe-sample normal deformation. Under such circumstances, the AFM cantilever and the probe-sample contact can be considered as two springs connected in series: the cantilever with spring constant $k_{cantilever}$ and the probe-sample contact with stiffness (or effective spring constant) $k_{contact}$. The force required to stretch these two springs in series with a total displacement Δz_{piezo} is equal to the normal force variation ΔF_z which is caused by the piezo-stage oscillation. This experimental configuration allows us to measure the total spring constant k_{tot} at each normal load F_z from the following relation:

$$\frac{\Delta F_z}{\Delta z_{piezo}} = k_{tot}(F_z) = \left(\frac{1}{k_{lev}} + \frac{1}{k_{cont}} \right)^{-1} \tag{3.2.1}$$

ΔF_z is recorded at each F_z and much smaller than F_z. An important feature, which distinguishes MoNI from traditional nano-indentation technique, is that the probe is first approached with a force ~ 10^2 nN to make hard contact with sample surface and then

quickly retracted from the surface. The normal force variation ΔF_z and total stiffness k_{tot} at each fixed normal force F_z are measured during the retraction.

The measurement of $\Delta F_z/\Delta z_{piezo}$ ($= k_{tot}$) at different normal loads F_z allows us to acquire the probe-sample contact stiffness $k_{contact}$ as a function of F_z since $k_{cantilever}$ is just the cantilever spring constant, which can be measured independently. After we measure $\Delta F_z/\Delta z_{piezo} = k_{tot}$, we integrate $k_{contact}$ versus F_z to obtain the F_z vs. indentation curves. The integration relationship to get the indentation curves is the following:

$$z_{indent}(F_z) = z_{indent}(F_{po}) + \int_{F_{po}}^{F_z} \frac{dF_z}{k_{cont}(F_z)} \tag{3.2.2}$$

Then the acquired indentation curves can be fitted with appropriate models to extract the Young's modulus and other physical properties of the objective materials, which will be discussed in detail in the following sections.

The following sections give a detailed description of the experimental procedures of MoNI in the step orders.

3.2.2   *AFM Piezo Tube Frequency Sweep*

The very first step of MoNI is to find a suitable frequency (f_{output}) of the lock-in amplifier output sinusoidal signal to the AFM piezo-tube. Since the AFM probe oscillation is directly controlled by the piezo-tube attached to the probe, f_{output} needs to be far from the piezo-tube resonance frequency f_{piezo}, otherwise the oscillation is too large for performing MoNI. Notice that the resonance frequency f_{piezo} is not the resonance frequency of the probe-
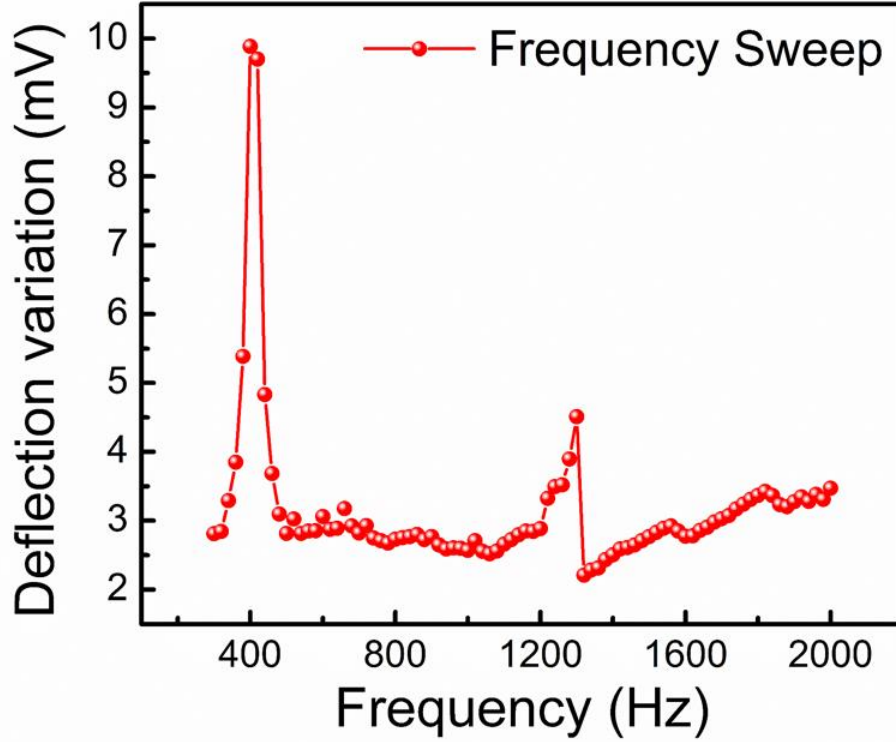
Figure 3.2.2: Frequency sweep of the piezoelectricity tube. Two resonance frequencies are found at ~ 400Hz and ~1300Hz.

cantilever system $f_{cantilever}$ (usually 300 to 500 KHz for the probes we use), which is much larger than f_{piezo}.

To measure f_{piezo}, we first approach the AFM probe in contact mode on a standard Silicon Carbide (SiC) wafer without oscillation. Afterwards we turn on the lock-in oscillation output and sweep the output frequency f_{output} by increasing with small interval (10 Hz) and record the corresponding root mean square (RMS) of the cantilever deflection

signal ΔV_{rms}^{Def} with the same lock-in amplifier simultaneously. We then plot ΔV_{rms}^{Def} versus

f_{output} as shown in Fig.3.2.2. There are two peaks at ~400 Hz and ~1300 Hz, respectively.

The deflection amplitude is quite "stable" between 600 to 1200 Hz, therefore we choose

$f_{output} = 0.991$ kHz (fixed) for the following measurements.

3.2.3   Lock-in Amplifier and Piezo Tube Calibration

The second step is to determine how much the amplitude of the output signal should

applied the AFM piezo tube in order to oscillate the piezo-probe system without too large

or too small amplitude.

First we calculate the AFM sensitivity W_N of the piezo-cantilever-laser system from

contact-mode force-distance curves acquired on very hard and flat material (SiC) with a

large force (>100nN) such that the $\Delta z_{piezo} = \Delta z_{cantilever\ bending}$ (in other words, the probe-

sample contact deformation is negligible). A set of approaching and retracting curves are

plotted with red and blue in Fig. 3.2.3, respectively. The "jump-off" point on the retracting

curve, which indicates the point when the probe-sample contact is lost, is also highlighted.

The optical sensitivity W_N is simply the slope of the "contact" part of the force-distance

curve. In Fig. 3.2.3, we have $W_N = 96$ nm/V.

Then we change the driving signal (output lock-in signal) ΔV_{rms}^{Drive} and record

the corresponding cantilever deflection variations in the photodetector ΔV_{rms}^{Def} while

the probe is in hard contact with the sample. A plot of ΔV_{rms}^{Def} versus ΔV_{rms}^{Drive} is shown

in Fig. 3.2.4, with which we can obtain a dimensionless slope S. Since $\dfrac{\mathrm{D}z_{piezo}}{\mathrm{D}V^{Def}}$ is just

the AFM sensitivity W_N and $\Delta V^{Def} = 2\sqrt{2}\Delta V^{Def}_{rms}$, we have:

$$\frac{\mathrm{D}z_{piezo}}{\mathrm{D}V^{Drive}_{rms}} = \frac{\mathrm{D}z_{piezo}}{\mathrm{D}V^{Def}}\frac{2\sqrt{2}\mathrm{D}V^{Def}_{rms}}{\mathrm{D}V^{Drive}_{rms}} = 2\sqrt{2}\times W_N \times S \qquad (3.2.3)$$

For example, if $W_N = 96$ nm/V and $S = 0.547$ (from Fig. 3.2.3 and Fig. 3.2.4), then

$$\frac{\Delta z_{piezo}}{\Delta V^{Drive}_{rms}} = 2\sqrt{2}\times 96 \times 0.547 = 148.5 \,\text{nm/V} \qquad (3.2.4)$$

It means that for a lock-in output voltage of 1 mV$_{rms}$, the piezo tube oscillates with an amplitude of 0.1485 nm. If we want an oscillation Δz_{piezo} of 0.2 Å, the lock-in output signal RMS value should be 0.02/0.1485=0.13 mV.
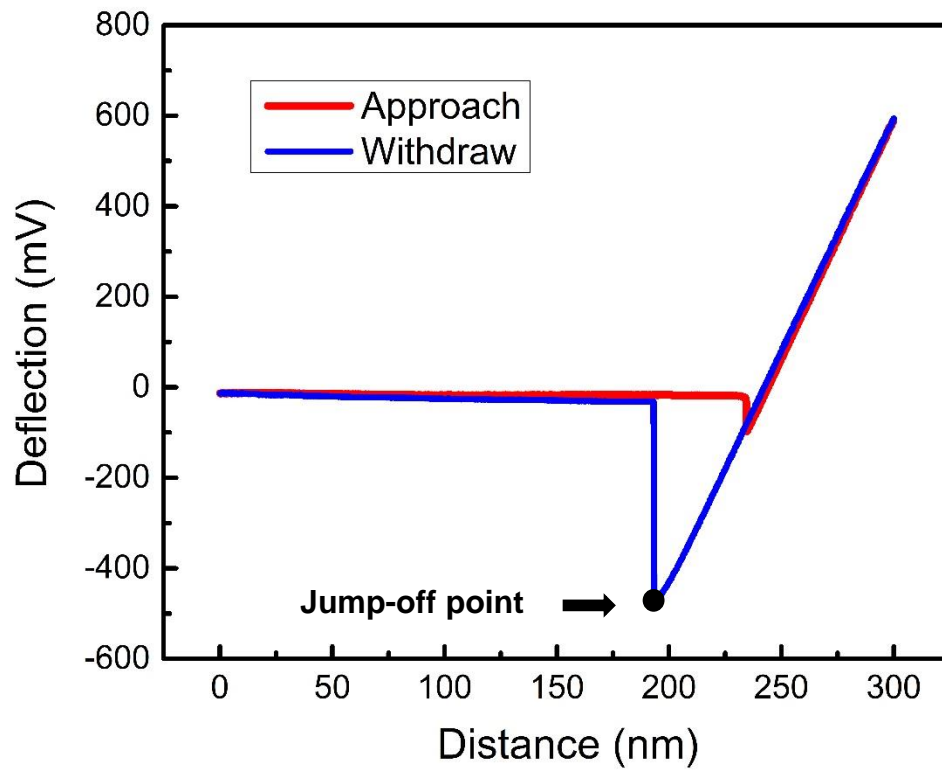
Figure 3.2.3: Force – distance curve of an AFM probe on a sapphire sample. The "jump-off" point is highlighted, the deflection corresponding to the jump-off point is the adhesion force between the probe and sample surface.
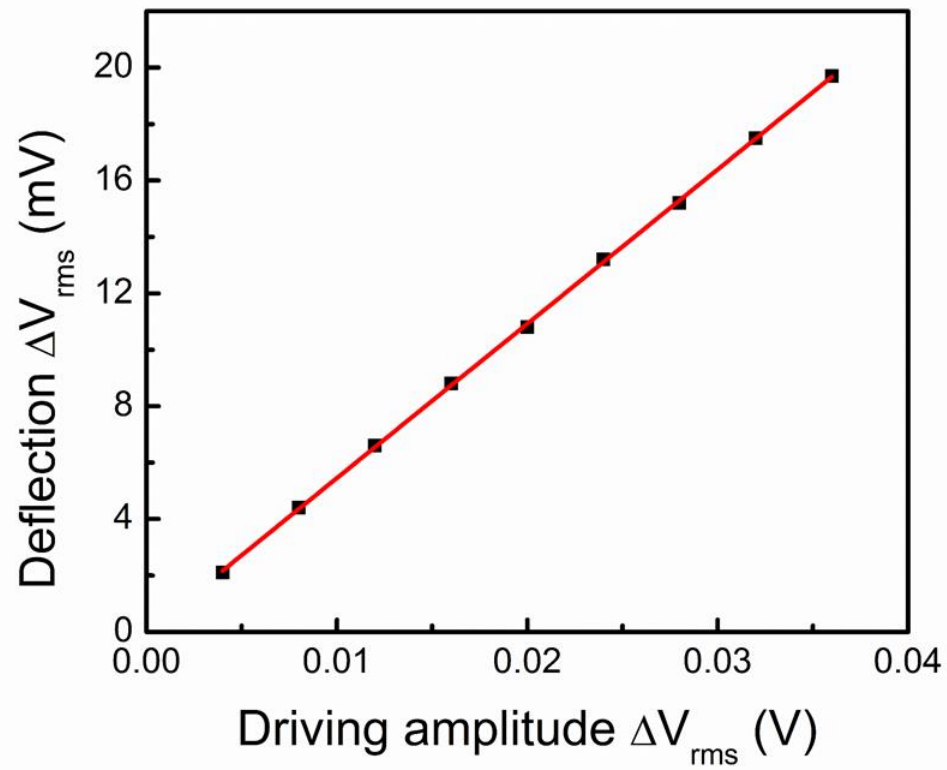
Figure 3.2.4: Relationship between amplitude of the oscillation signal (applied to the piezo tube) and the corresponding deflection variation.

Figure 3.2.5: The front face of the PicoPlus AFM controller. The Aux portal indicated

with blue box is the input of the small oscillation.

3.2.4 Data Acquisition

As mentioned at the beginning of this chapter, previous nano-indentation method can be termed as "direct measurement" since the indentation curve (or force vs. displacement curve) is directly obtained by indenting a large distance with an AFM probe on the suspended sample. MoNI, however, is a differential measurement which means we do not directly collect the indentation curve but instead measure the slope of the indentation curve and integrate over the normal force afterwards. The differential method can dramatically decrease the noise level (by integrating) and increase the vertical resolution.

Before starting the experiment, we need to slightly adjust the position of photodetector such that the "deflection" (or "vertical") and "friction" (or "horizontal") signal are 0.00V. After approaching the AFM probe under contact mode with a large force (~ 100nN) on the sample surface, we apply the output signal to Z-piezo through the input portal on the AFM controller (Fig. 3.2.5) with the frequency and amplitude acquired in *3.2.2* and *3.2.3*. We can use PicoView, the official software of Agilent AFM to acquire the raw data curves in the following steps (assuming the probe is already approached on the surface):

(1) Open "Spectroscopy" window by clicking "Spectroscopy" icon

(2) Switch to "Expert" mode under the "Spectroscopy" tab

(3) Switch the output control to "Force Setpoint", choose "input" as "HEB Aux", here HEB stands for the "Head Electronic Box" of AFM

(4) Enter the "duration time" which is the total data acquisition time, to avoid thermal drift, a value from 10 to 40 seconds is suitable

(5) Choose the number of data points, 200 to 1000 is suitable

(6) (Most important step) Choose the starting and ending value of the force setpoint. Obviously, the starting point should always be larger than the ending point. Since we want to investigate the indentation behaviour at Å-scale displacement, *the ending point should be slightly after the "pull-off" point*. Since the deflection is 0.00V before approaching, 0V is a good try for the ending point. The range of the setpoint can be simply calculated by $F/(W_N \times k_{cantilever})$. The normal force range for most MoNI measurements are from 30 to 100nN. For example, if $F_z = 80$nN, $W_N = 80$nm/V and $k_{cantilever} = 50$N/m, the setpoint range is simply $80/(80 \times 50) = 0.02$V. Then the starting point is $0 + 0.02V = 0.02V$. Once all the parameters are established, start the data collection. A typical raw curve is shown in Fig. 3.2.6(a). The pull-off force (or adhesion force) is approximately -0.027 in the unit of Volt. Usually we need to adjust the ending point to find the jump-off point.
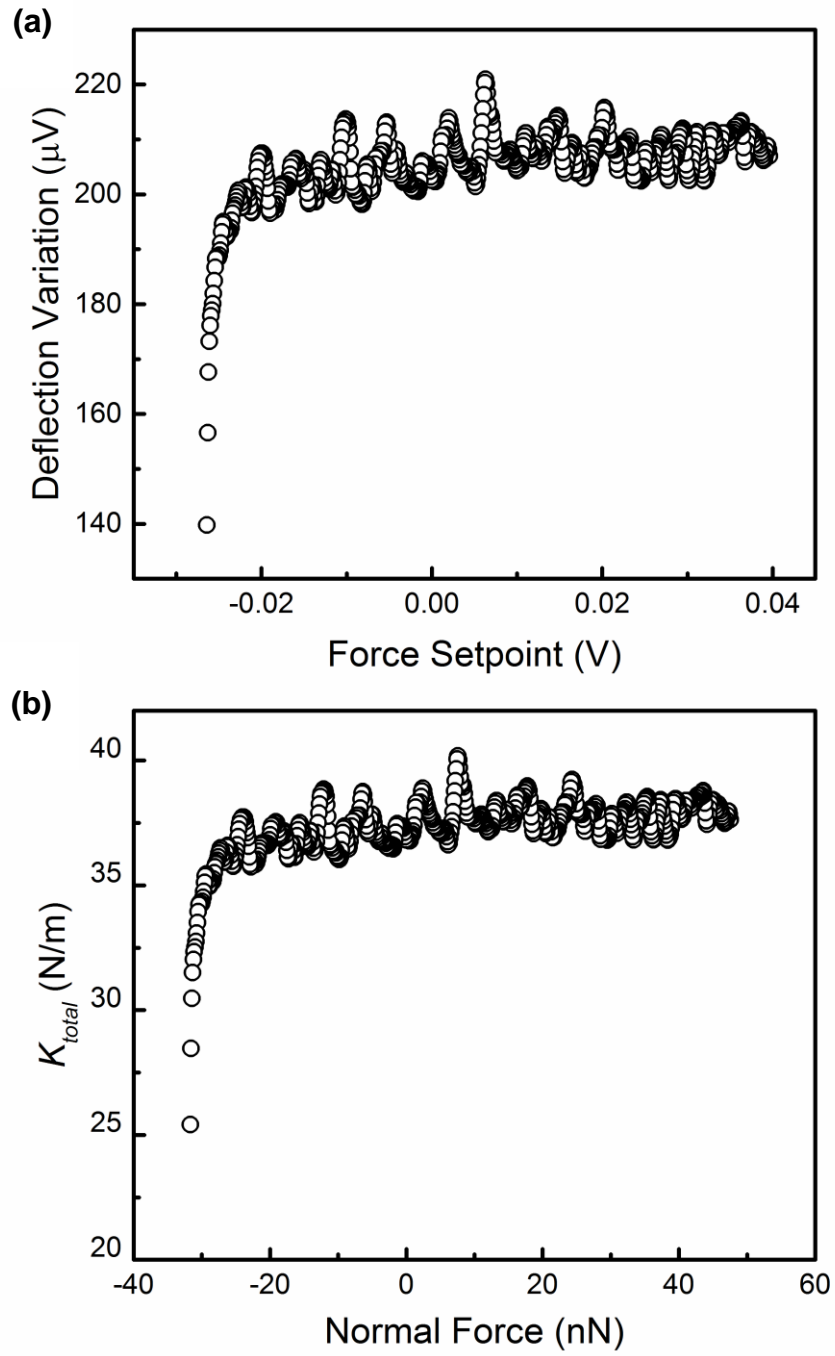
Figure 3.2.6: The raw MoNI data acquired on a SiC standard sample. (a) The raw deflection variation ΔV vs. normal force setpoint V. (b) total spring constant vs. normal force. Apparently, the curves in (a) and (b) have exactly the same shape.

3.2.5 Integration and Indentation Curves

In the raw data curve shown in Fig. 3.2.6(a), the X-axis is the deflection setpoint displayed in the unit of Volt, the normal force F_z can thus be converted by the following equation:

$$F_z = Setpoint\ (in\ Volt) \times k_{cantilever} \times W_N \tag{3.2.5}$$

Where $k_{cantilever}$ and W_N are the cantilever spring constant and laser-cantilever optical sensitivity.

The Y-axis the RMS value of the deflection variation ΔV_{rms}^{Def} caused by the applied sinusoidal oscillation. We can easily calculate the normal force variation in the same way as Eq. 3.2.5:

$$\Delta F_z = 2\sqrt{2} \times \Delta V_{rms}^{Def} \times k_{cantilever} \times W_N \tag{3.2.6}$$

Notice that the factor $2\sqrt{2}$ cannot be neglected since ΔV_{rms}^{Def} is RMS value which differs the amplitude by the factor of $2\sqrt{2}$. With oscillation Δz_{piezo} and normal force ΔF_z variation ready, we can simply divide the two parameters to get the total effective spring constant k_{tot} of the serial spring system of the cantilever $k_{cantilever}$ and probe/sample contact interface $k_{contact}$ as shown in Fig. 3.2.6(b). In other words, the raw data curve shows the total spring constant k_{tot} as a function of the normal force F_z.

The fixed piezo oscillation Δz_{piezo} is the sum of the cantilever bending displacement $\Delta z_{cantilever}$ and the probe/sample contact deformation $\Delta z_{contact}$.

$$\Delta z_{piezo} = \Delta z_{cantilever} + \Delta z_{contact} \qquad (3.2.7)$$

Dividing both sides of Eq. 3.2.7 by the normal force variation ΔF_z, we have

$$\frac{\Delta z_{piezo}}{\Delta F_z} = \frac{\Delta z_{cantilever}}{\Delta F_z} + \frac{\Delta z_{contact}}{\Delta F_z} \qquad (3.2.8)$$

As mentioned above, $\dfrac{\Delta F_z}{\Delta z_{cantilever}}$, $\dfrac{\Delta F_z}{\Delta z_{contact}}$ and $\dfrac{\Delta F_z}{\Delta z_{piezo}}$ are $k_{cantilever}$, $k_{contact}$ and k_{tot},

respectively. To be more specific:

$$\frac{1}{k_{tot}} = \frac{1}{k_{cantilever}} + \frac{1}{k_{contact}} \qquad (3.2.9)$$

Eq. 3.2.8 and Eq. 3.2.9 are actually equivalent. Since $k_{cantilever}$ is fixed, we can easily extract $k_{contact}$ from Eq. 3.2.9 and plot $k_{contact}$ vs. F_z. Finally we can integrate $1/k_{contact}$ over the range of F_z to get the probe/sample contact deformation $z_{contact}$.

$$z_{contact}(F_z) = \int \frac{\Delta z_{contact}}{\Delta F_z} \times \Delta F_z = \int \frac{\Delta F_z}{k_{contact}(F_z)} \qquad (3.2.10)$$

Figure 3.2.7 displays the indentation curve integrated from Fig. 3.2.6.
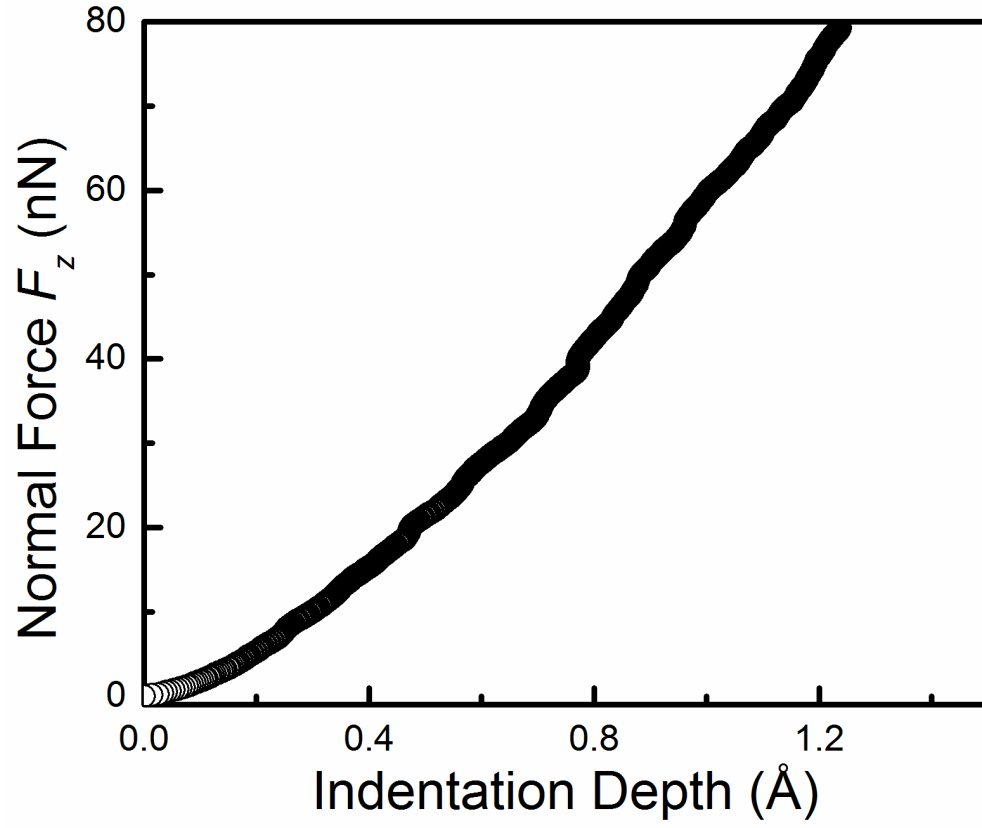
Figure 3.2.7: The indentation curve integrated from the raw data in Fig. 3.2.6 using Eq. 3.2.9 and Eq. 3.2.10.

Because of the design of the AFM used in MoNI experiments, the laser photo-detector undergoes a slow mechanical drift with time, which corresponds to a normal force drift of ~1nN/minute for the cantilever used in this thesis. This mechanical drift re-starts each time something in the AFM set-up is mechanically changed (e.g. the door of the AFM cage is open/closed). The indentation curves are acquired one after the other one in different locations of the sample for several consecutive hours. Therefore, after 6 hours of acquisition time the measured "apparent" shift of the pull-off force compared to the initial indentation measurement may be around 400 nN. We hereby remark that the normal force shift shown in some of the figures in this thesis is only due to a mechanical drift of the laser photo-detector.

However, very importantly, each raw curve is acquired within an average of 25 seconds, therefore in each curve we have a drift in the normal force F_z from the beginning of the indentation acquisition to the end of the individual curve acquisition of only $\Delta F_z \sim$ 0.4 nN, which is within the experimental error of the normal force reported in this thesis. This error in the normal force translates into an error in the indentation position of $\Delta z \sim$ 0.008 nm, which is smaller than the error reported as the limit of accuracy of the MoNI method $\Delta z = 0.01$ nm. We also underline (see Fig. 3.2.8) that while the indentation curves may shift along the F_z axis, the curves for the same material and conditions are almost perfectly congruent. Furthermore, we remark that other sources of errors and noise including the drift of the piezo-tube are instead fully compensated by the fact that the feedback loop is on during the indentation experiments and we acquire differential forces by lock-in detection.
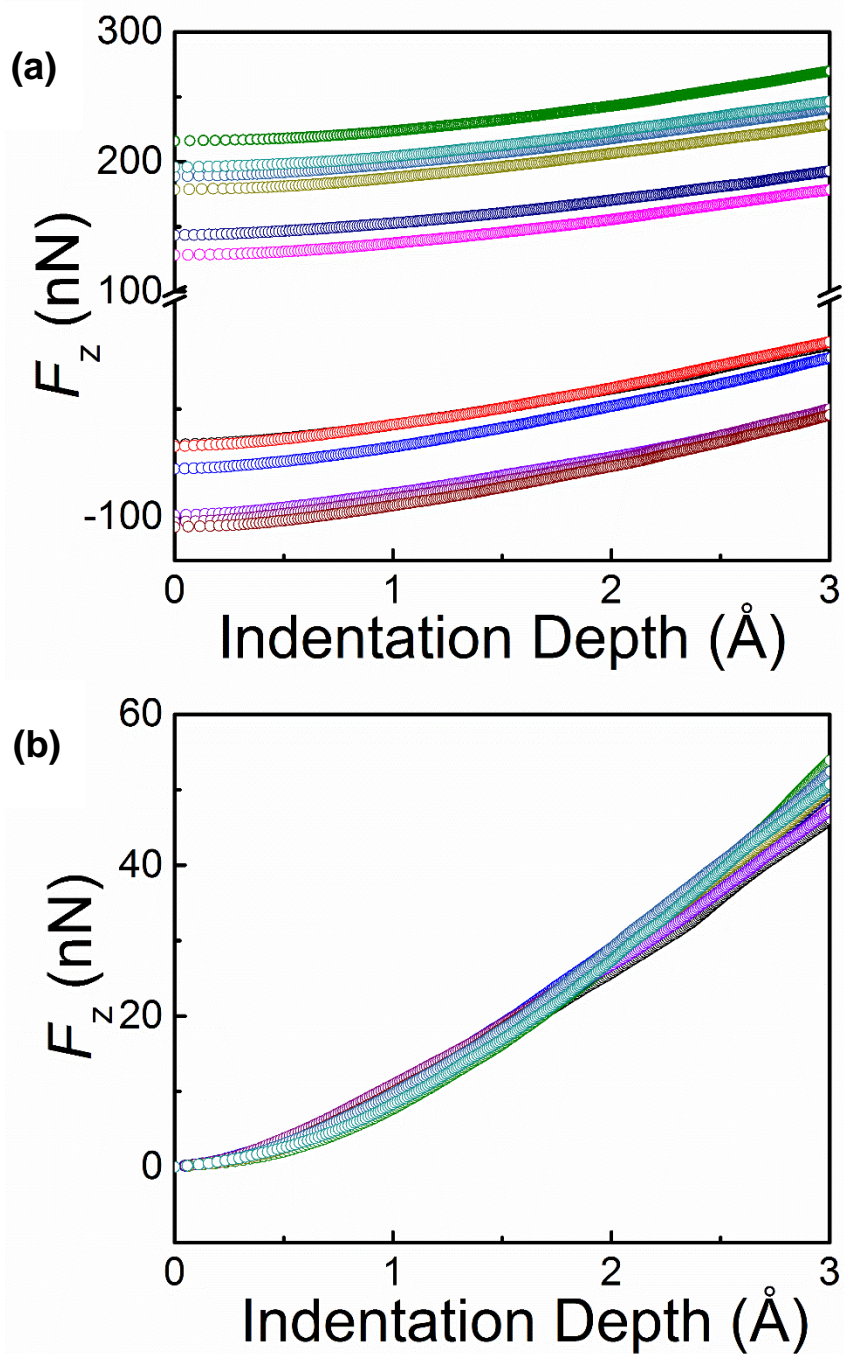
Figure 3.2.8: Indentation curves obtained on a graphene oxide (GO) sample at different regions within one set of measurement (~3 hours). (a) Raw indentation curves. (b) Indentation curves shift on *F*-axis to the origin point. Reprinted with permission from [85]. Copyright 2015, Nature Publishing Group.
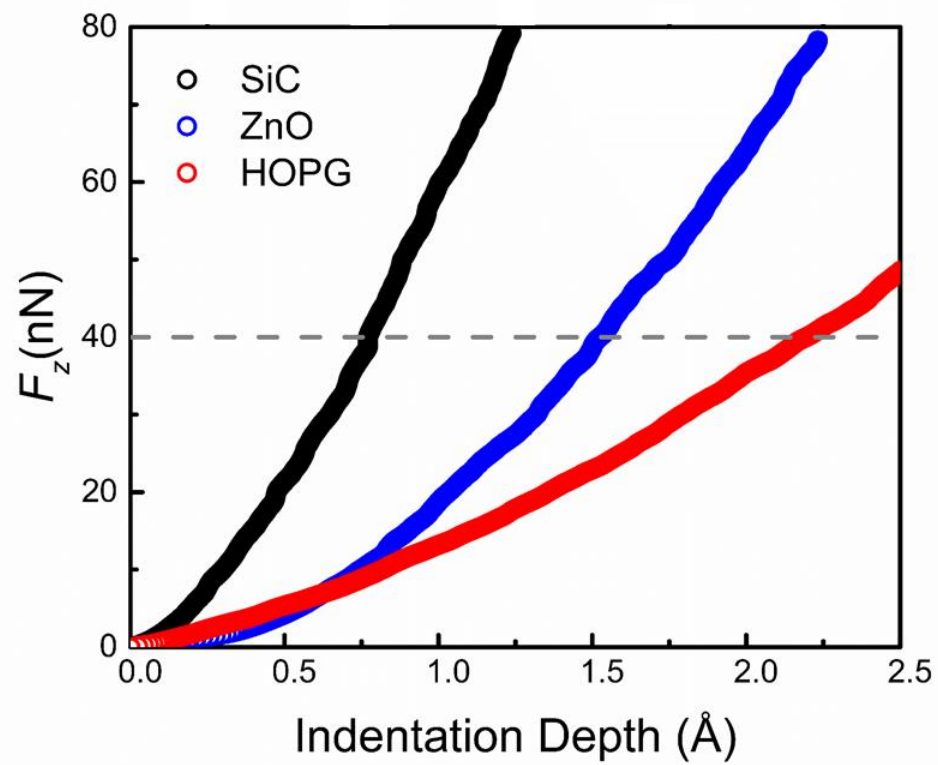
Figure 3.2.9: Indentation curves of SiC, ZnO and HOPG taken by one AFM probe.
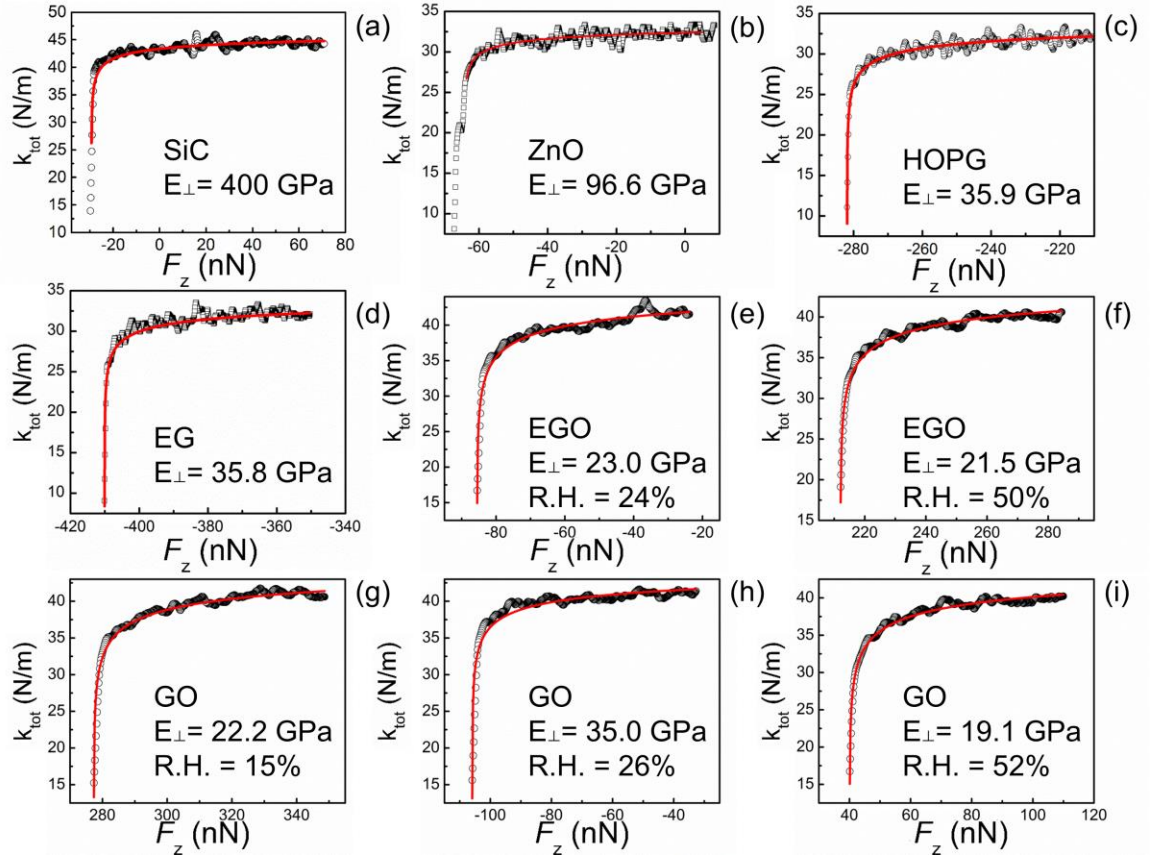
Figure 3.2.10: (a), (b), (c), (d) k_{tot} versus F_N curves of single crystal SiC, ZnO, highly oriented pyrolitic graphite (HOPG) and epitaxial graphene (EG), respectively. The black open dots are the raw curves while the red lines are the corresponding Hertz-plus-offset fitting curves modified to include adhesion according to the DMT model described in *3.2.6*). (d), (e) k_{tot} versus F_z curves of epitaxial graphene oxide (EGO) at 24% and 50% relative humidity (R.H.), respectively. (g), (h), (i) k_{tot} versus F_z curves of conventional graphene oxide (GO) films at 15%, 26% and 52% R.H., respectively. Reprinted with permission from [85]. Copyright 2015, Nature Publishing Group.

The stiffness of different materials can be qualitatively compared with the indentation curves acquired with the same AFM probe. In Figure 3.2.9, a horizontal gray line is plotted for $F_z = 40$ nN. The indentation depths of SiC, ZnO HOPG are approximately 0.8Å, 1.5Å and 2Å, respectively. Intuitively, the stiffer the material, the more difficult to indent a certain depth. Therefore, we can easily conclude that stiffness order is SiC > ZnO > HOPG. The Young's moduli we found in literature for SiC, ZnO and graphite are 400 GPa, 143 GPa and 36 GPa [85, 87, 89], respectively. Therefore, MoNI's qualitative accuracy is validated. Notice that all the data collection and mathematical calculation above are completely accurate without any approximations. The raw ktot vs. Fz curves of SiC, ZnO and HOPG as along with some epitaxial graphene (EG), graphene oxide (GO) and epitaxial graphene oxide (EGO) are also shown in Fig. 3.2.10. More detailed discussion of MoNI on 2D materials can be found in the next chapter.

However, we need an appropriate model to fit the indentation curves to extract analytical results. A detailed discussion of contact mechanics theory has been demonstrated in Chapter I, thus we will directly compare the DMT (Derjaguin, Muller and Toporov) [6] and JKR (Johnson, Kendall and Roberts) [5] models without digging into the theories. We remark again that both DMT and JKR models are in principal only valid for isotropic materials and in fact there is no analytical model for anisotropic materials contact [90, 91].

3.2.6 MoNI Calibration: Contact Mechanics Analysis and Curve Fitting

A calibrating MoNI measurement on a rigid and flat material has to be performed before moving to 2D materials to test the whole MoNI system's reliability as well as the model feasibility. As discussed in section 1.2, JKR and DMT are two frequently used

models in contact mechanics. Therefore in this section, we only focus on the validity of these two models.

SiC is a quasi-isotropic material with only one pair of Young's modulus E (400 GPa) and Poisson Ratio v (0.14) required to characterize its elastic property. Furthermore, SiC surface is pretty flat (surface roughness is within 0.5nm for an area of 500nm as shown in Fig. 3.2.11) and is stable under ambient temperature, humidity and pressure. Thus SiC is a perfect material for the reliability calibration of MoNI. Quartz sometimes is also used for MoNI calibration. Based on the discussion in Chapter I, we can derive that:

$$k_{contact}\ (Hertz \text{ and } DMT)\ = 2E^*a \tag{3.2.11}$$

$$k_{contact}(JKR) = 2E^*a \times (1 - \frac{2\sqrt{\dfrac{|F_{po}|}{3aRE^*}}}{\dfrac{2a}{R} - \sqrt{\dfrac{|F_{po}|}{3aRE^*}}}) \tag{3.2.12}$$

$$a_{DMT} = (\frac{3F_z R}{4E^*})^{1/3} \tag{3.2.13}$$

$$a_{JKR} = \{\frac{3R}{4E^*}[F_z - 2F_{po} + 2\sqrt{(-F_{po}F_z + F_{po}^2)}]\}^{1/3} \tag{3.2.14}$$

where E^* is the effective Young's modulus of the probe/sample contact, a is the contact area, R is the probe apex radius (for the curve in Fig. 3.2.8, $R = 120$ nm, probe radius measurement methods can be found in section 3.3) and F_{po} is the "pull-off" force (adhesion force). Here $E^* = (\dfrac{1-v_{sample}^2}{E_{sample}} + \dfrac{1-v_{probe}^2}{E_{probe}})^{-1}$ with $v_{sample/probe}$ and $E_{sample/probe}$ being the
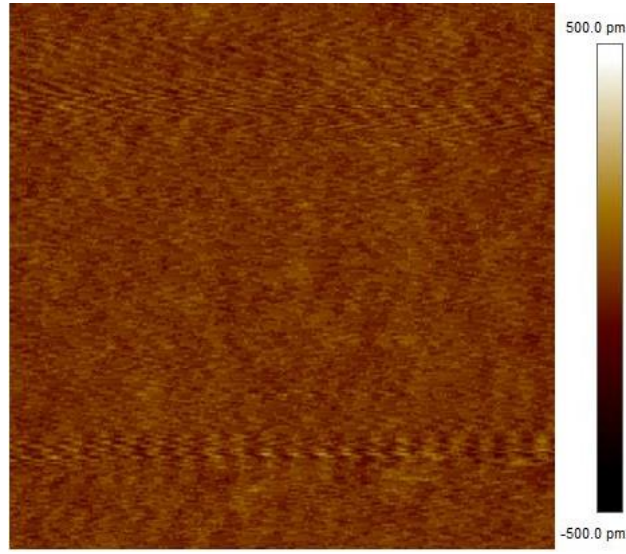
Figure 3.2.11: AFM topographic image of a SiC sample. The image size is 500nm and surface roughness is within 0.5nm.
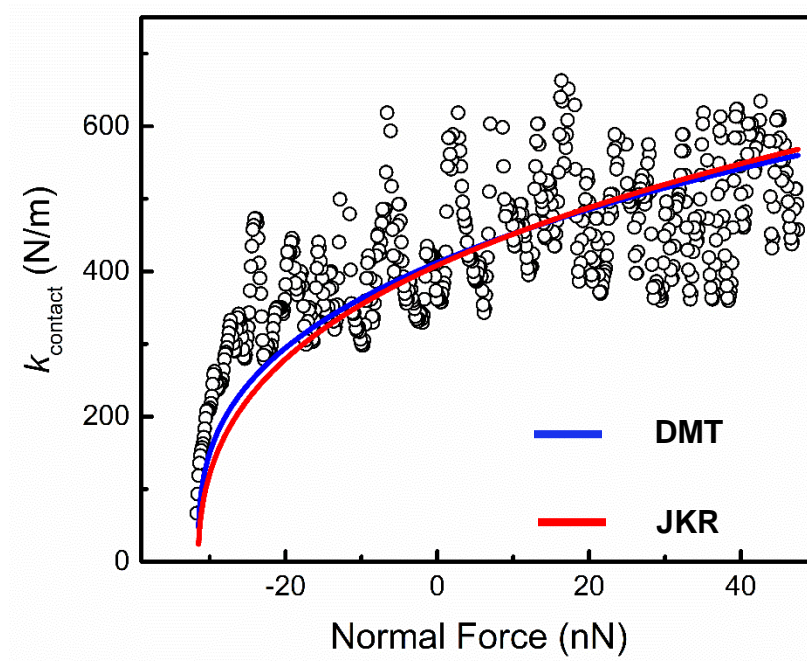
Figure 3.2.12: $k_{contact}$ vs. F_z of SiC. The blue and red curves are DMT and JKR fittings, respectively.
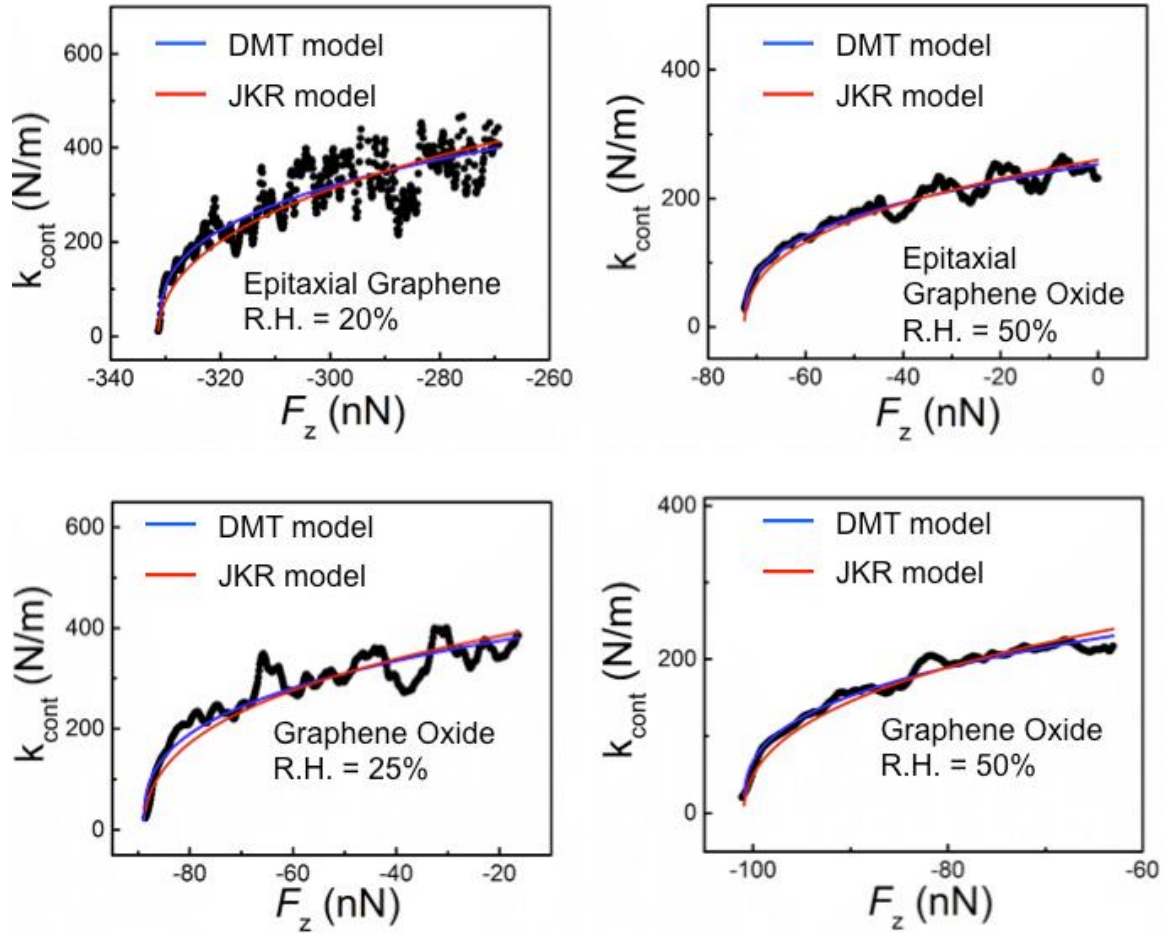
Figure 3.2.13: (a), (b), (c), (d) raw data of k_{cont} versus F_z for epitaxial graphene (EG), epitaxial graphene oxide (EGO) and conventional graphene oxide (GO), and corresponding DMT (blue line) and JKR (red line) fitting curves using the relationship (3.2.11) and (3.2.12). Reprinted with permission from [85]. Copyright 2015, Nature Publishing Group.

Poisson's ratio and Young's moduli of the investigated sample and the AFM probe, respectively. For the silicon probe used in the MoNI measurements, we use $E_{probe} = 169$ GPa and $v_{probe} = 0.27$ [86].

Figure 3.2.12 shows an experimental curve (black) of $k_{contact}$ vs. F_z of SiC as well as DMT (blue) and JKR (red) models. Apparently, DMT model is a better fit than JKR model which can be expected since DMT applies for small and stiff contact; but we also remark that the two models don't differ significantly. Besides, DMT model is much mathematically simpler than JKR model, we decided to use DMT model for most of MoNI measurements. Thus the equation to fit the indentation curve to extract the Young's modulus is:

$$F_z = \frac{4}{3} E^* R^{1/2} z_{contact}^{3/2} + F_{po} \qquad (3.2.15)$$

With all the probe parameters plugged into Eq. 3.2.15, we can get a Young's modulus of 400 GPa of SiC from Fig. 3.2.7, which is quite close to the value reported in literature.

Only by performing MoNI on a standard SiC (or Quartz) sample and obtaining a correct and reproducible Young's modulus, we can safely claim the MoNI system is reliable and stable. This is the so called "MoNI calibration" and it's critical before any measurements on 2D materials, especially after switching to a new AFM probe. Figure 3.2.13 shows some experimental curves (black) of $k_{contact}$ vs. F_z of epitaxial graphene (EG), graphene oxide (GO) and epitaxial graphene oxide (EGO) with DMT (blue) and JKR (red) fittings. Clearly, for 2D materials, DMT is still a more appropriate fitting model.

3.3   AFM Probe Radius and Cantilever Spring Constant Determination

3.3.1   Probe Radius Determination

There are mainly two methods to determine the AFM probe radius. The first and easiest way is taking a Scanning Electron Microscopy (SEM) image of the probe sideway as shown in Fig. 3.3.1 and we can measure the curvature radius directly. The other method is so-called "reference material method". We apply MoNI on a well-known quasi-isotropic material like SiC or fused Quartz of which the Young's moduli are known, then we fit the k_{tot} versus F_z curves while keeping E^* fixed and R as free fitting parameter. The last step is to calculate the average value of R over a set of consistent measurements. We use both methods to ensure consistency of the results. When the tip radius R is known, we use its value in the following MoNI fitting procedures. We underline that to insure that the probe is not changed or damaged during a set of measurements, we always use SiC as a reference sample before and after each set of measurements. If the reference samples cannot reproduce the "standard" indentation curves, the probe is discarded as well as the previous measurements.

3.3.2   Cantilever Spring Constant Measurement

We usually use Sader method [92] to determine the spring constant of the cantilever. Sader *et al.* demonstrated that for a rectangular cantilever:

$$k = M_e \rho_c bhL\omega_{vac}^2 \qquad\qquad (3.3.1)$$
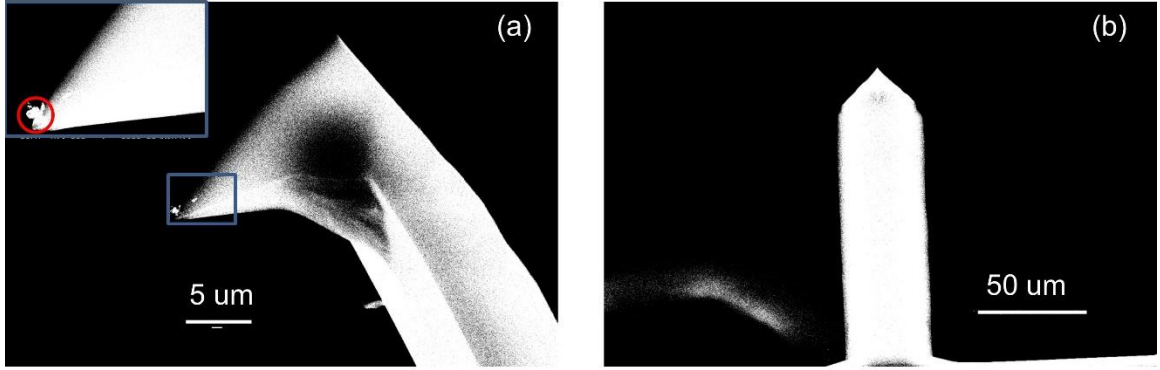
Figure 3.3.1: Scanning Electron Microscopy (SEM) images of an AFM probe used for MoNI. Reprinted with permission from [85]. Copyright 2015, Nature Publishing Group.

where ρ_c is the density of the cantilever, h, b and L are the thickness, width and length of the cantilever, respectively. ω_{vac} is the fundamental radial resonant frequency of the cantilever in vacuum. M_e is the normalized effective mass and $M_e = 0.2427$. We can simply measure the probe dimension with SEM (as shown in Fig. 3.3.1), tune the probe in Tapping Mode to get the resonance frequency and then employ Eq. 3.3.1 to calculate the spring constant quickly. For the probe in Fig. 3.3.1, the width and length are 35 µm and 110 µm, respectively; the thickness is 5.3 µm; and the resonance frequency is 326 kHz. Therefore, the resulting spring constant is 46 N/m, which is quite close to the spring constant claimed by the manufacturer - 45N/m.

Sader also proposed another more general equation for the spring constant of a rectangle cantilever [93, 94]:

$$k = 0.1906 \, \rho_f b^2 L Q_f \Gamma_i(\omega_f) \omega_f^2 \tag{3.3.2}$$

ρ_f is the density of the surrounding fluid (in our case, air), b and L are the width and length of the cantilever, Q_f is the quality factor of the cantilever and ω_f is the fundamental mode resonance frequency. Γ_i is the imaginary component of the hydrodynamic function which only depends on the Reynolds number

$$\mathrm{Re} = \rho_f \omega_f b^2 / (4\eta) \tag{3.3.3}$$

η is the viscosity of air, and is independent of the cantilever. More details of the mathematical derivation can be found in [95].

Figure 3.3.2 is a Scanning Electron Microscopy (SEM) image of another AFM probe used for MoNI (TAP525A, purchased from Bruker). The dimension of the cantilever can be easily obtained, here we have $b = 51.4\mu m$, $L = 118.0\mu m$. The resonance frequency and Quality factor of the cantilever are 525 kHz and 890, respectively. For air we use $\rho_f = 1.18 \mathrm{kg/m^3}$, $\eta = 1.86 \times 10^{-5} \mathrm{kg \cdot m^{-1} \cdot s^{-1}}$. Then we plug all the above parameters into Eq. 3.3.3 to get Re = 136. Plug the calculated Reynolds number into the hydrodynamic function $\Gamma(\omega_f)$ we can obtain the imaginary part $\Gamma_i = 0.255$. Finally we plug all the parameters into Eq. 3.3.2 and obtain $k = 173$ N/m, which is close to the spring constant claimed by the manufacturer - 200N/m.
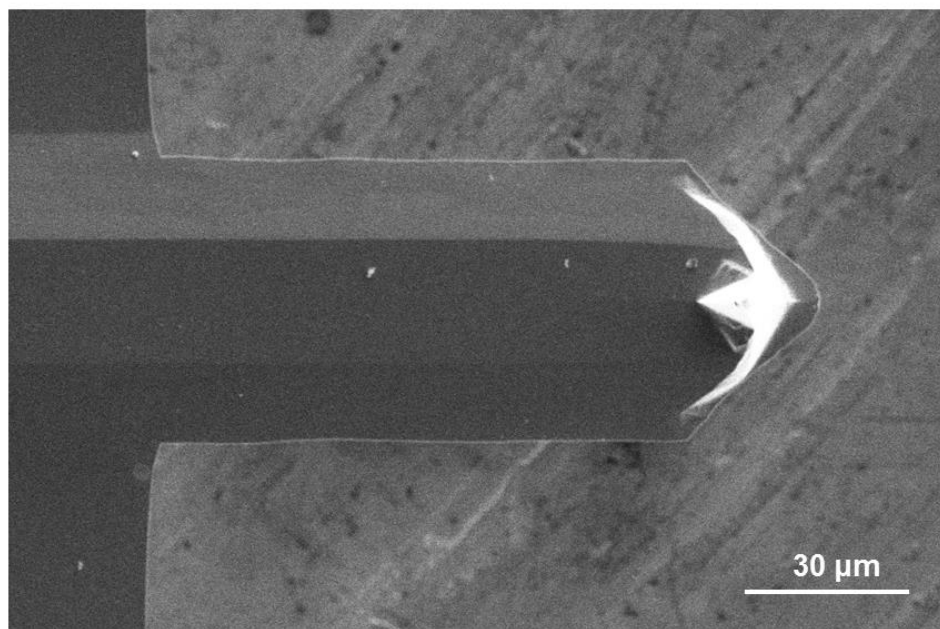
Figure 3.3.2: Scanning Electron Microscopy (SEM) images of an AFM probe used for MoNI.

CHAPTER 4.   INTERLAYER ELASTICITY OF 2D MATERIALS

This chapter is partly reproduced from the author's published article "Elastic coupling in the layers of two-dimensional materials" [85].

4.1   Inter-layer Elasticity of Epitaxial Graphene

4.1.1   Motivation

Recently, a large scientific and technological effort is underway to understand and control the properties of 2D materials, because of their potential technological applications [19-21, 85]. The most studied 2D material is graphene, existing as a single layer of graphite or a few-layer thick epitaxial graphene film. As discussed in section 2.1, one of the main characteristics of 2D materials is the high anisotropy between the in-plane and perpendicular-to-the-plane properties. For example, in graphite due to the strong covalent bonds between atoms in the plane, and the weak van der Waals interlayer interaction, the in-plane Young's modulus is $E_{//} = 1$ TPa [40], while the interlayer perpendicular-to-the-plane Young's modulus is only $E_{\perp} = 36$ GPa [24]. Recent studies have suggested that the mechanical properties of 2D materials are strongly correlated to their structure, and properties [96]. The in-plane Young's modulus of exfoliated graphene has been widely studied in bending experiments where a film is suspended on trenches or holes, and an AFM tip is used to bend the suspended film with deformations of tens and hundreds of nanometers [40]. On the other hand, very little is known about the elasticity perpendicular to the planes, hereafter called perpendicular or interlayer elasticity, of 2D materials composed of very few atomic layers. Recent calculations have investigated the out-of-

plane shear and Young's modulus of carbon nanotubes and graphene [97]. Experimentally, resonance ultrasound spectroscopy was used to study the elastic constants and the anisotropy between the in-plane and perpendicular-to-the-plane directions of thin films [98]. Investigations of the perpendicular-to-the-plane elasticity of a-few-layer-thick 2D films have not been reported, at the best of our knowledge, and remain an experimental challenge because they require to perform indentations on supported – as opposed to suspended – 2D films where the indentation should remain smaller than the films interlayer distance, i.e., less than a few Angstroms. Nevertheless, the interlayer elastic coupling is particularly important since it is related to the thermal [99], electronic [100], tribological [101], and optical [102] properties of 2D films. The perpendicular elasticity is expected to be affected by the structure and chemistry of the layers, the presence of stacking and intrinsic defects, and intercalation, which is a critical process for doping and tuning mechanical and electronic properties in 2D films.

Due to its unique feature, MoNI is a perfect method for the investigation of the interlayer elasticity of graphene. In this thesis we focus only on epitaxial graphene (EG) which is topologically flatter and cleaner than exfoliated graphene.
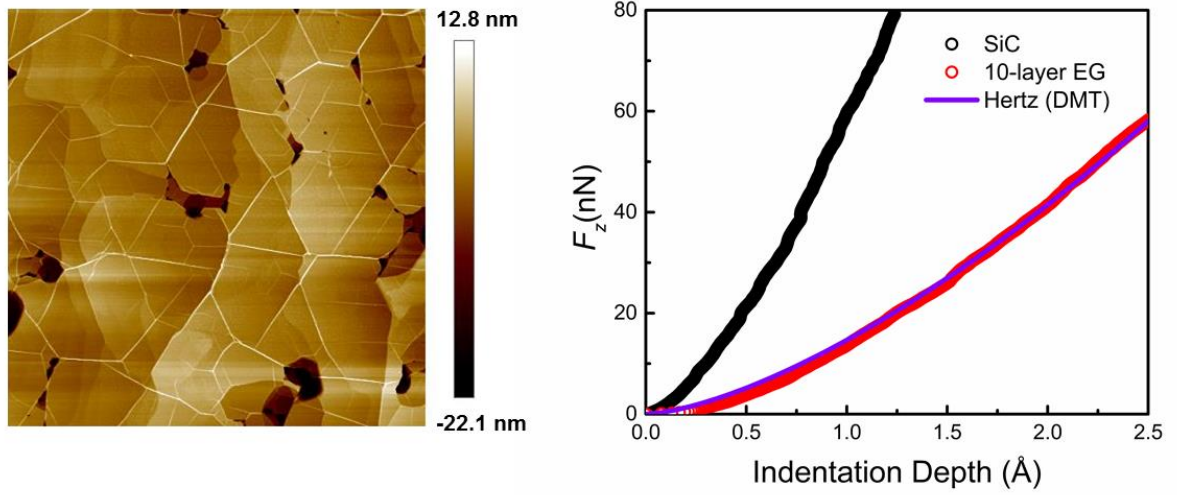
Figure 4.1.1: Left: AFM topographic image of a 10-layer epitaxial graphene (EG) grown on SiC (000-1). Right: MoNI indentation curves of a standard SiC sample (black), 10-layer EG (red) shown in the left panel and a Hertzian prediction with R = 120nm and $E_{graphene}$ = 36 GPa (purple).

4.1.2   *Experimental MoNI Results on Epitaixial Graphene*

Figure 4.1.1 shows an indentation curve of 10-layer EG on the Carbon polar face (000-1) of SiC as well as an indentation curve of SiC (a SiC sample purchased together with the SiC sample annealed to grow this 10-layer graphene), and a Hertz (DMT) curve with Young's modulus of E_1 = 36 GPa (graphite), E_2 = 169 GPa (Si tip) and tip radius R = 120nm. In Fig. 4.1.1, an AFM image of the EG sample is also displayed. We mark here all the curves reported in this chapter were taken with the same AFM probe as shown in Fig. 3.3.1. Interestingly, the 10-layer EG curve, HOPG curve and a theoretical Hertz curve overlap pretty well. This may imply that Hertz model is also valid for 10-layer EG.

Therefore, we could use Hertz model to fit the indentation curves leaving the interlayer Young's modulus $E_\perp$ as a free fitting parameter.

We have repeated several measurements as shown in Fig. 4.1.2 (we skip the integral part and directly fit the raw k_{total} vs. F curves to save time), and the Hertz fit provides for 10-layer epitaxial graphene a modulus perpendicular to the planes equal to $E_\perp = (36 \pm 3)$ GPa, the same as that of graphite [89]. This is not so surprising because graphene can be mechanically regarded as a "thinner version" of graphite, the inter-layer van der Waals property should not differ significantly. What remains unclear is why Hertz model, which is only valid for isotropic body theoretically, also works for 10-layer EG. This is not a coincidence. We will demonstrate this in the following two sections with two different methods.
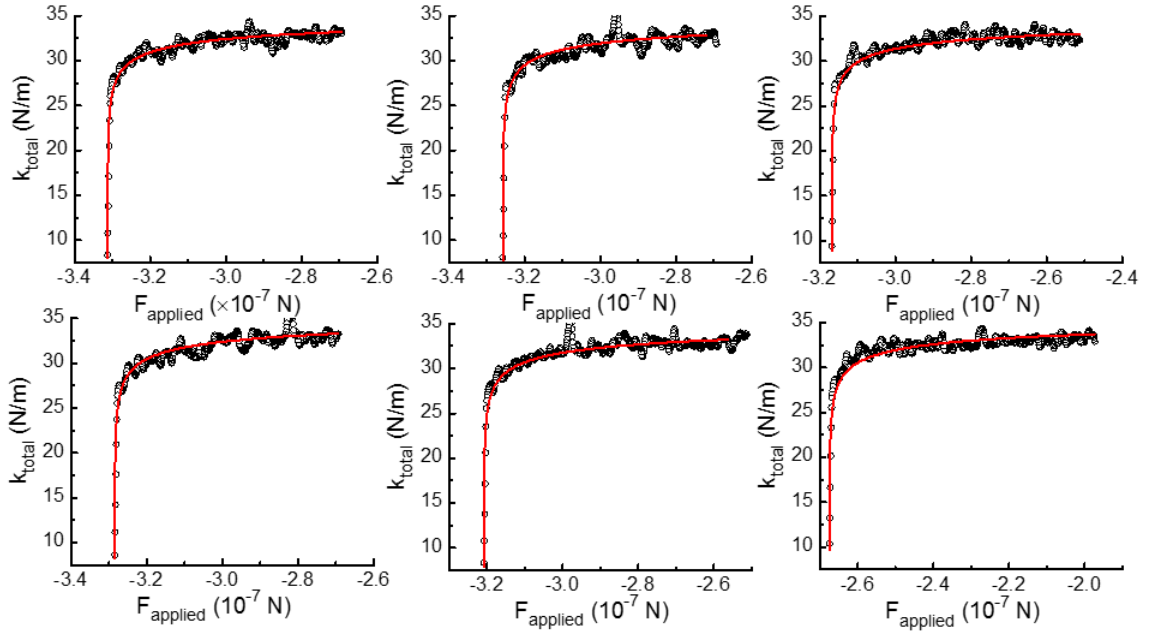
Figure 4.1.2: Six randomly chosen (from more than 20 curves) k_{total} vs. F curves from one set of MoNI experiments on epitaxial graphene. The red line in each panel is the Hertzian fitting curve.
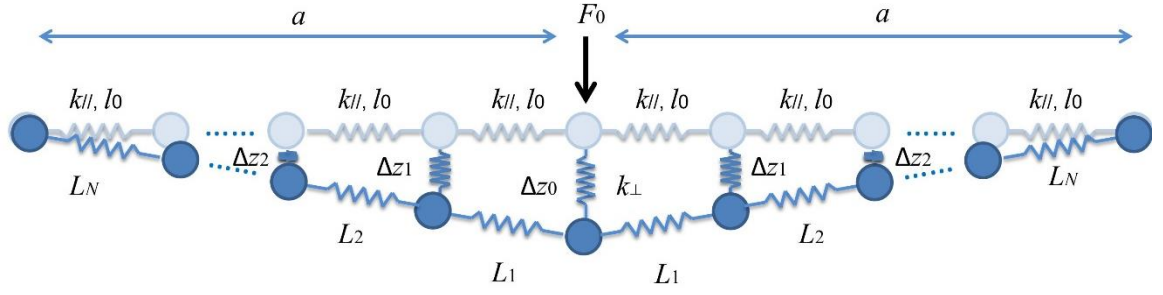
Figure 4.2.1: A one-dimensional spring system to illustrate the physical mechanism of the probe − 2D film contact. Reprint with permission from [85]. Copyright 2015, Nature Publishing Group.

4.2   Back-of-the-envelope Model

Following the MoNI (Å-indentation) provided in Chapter III, one can obtain the force vs. deformation curve of any material. We can directly compare the relative stiffness of two materials qualitatively from their indentation curves. However, if we want to extract quantitative results from the indentation curve, an analytical model is essential. We have reviewed some most-commonly used models in Chapter I, unfortunately, all of which are in principal only valid for isotropic materials. As a matter of fact, there's no analytical model for the contact of anisotropic materials.

However, the Hertz model (more specifically, DMT model) works pretty well in our report on 2D materials when some conditions are satisfied (actually they are always satisfied in MoNI experiment on 2D materials). A semi-quantitative back-of-the-envelope

analysis is given here to demonstrate the reason. We mark here this analysis is not perfect but able to settle our problem.

The layered material can be regarded as a system of springs, as shown in Fig. 4.2.1. The perpendicular spring constant $k_\perp$ represents the inter-layer interaction (i.e. the van der Waals interaction) while the in-plane spring constant $k_{//}$ represents the in-plane inter-atom interaction (i.e. covalence bonding). We have, $k_\perp / k_{//} \sim E_\perp / E_{//}$, where E are the elastic moduli of the material. The equilibrium lengths for the two types of springs ($k_\perp$ and $k_{//}$) are the inter-layer distance d_0 and the length of the in-plane covalent bond l_0, respectively. When a normal force F_0 is applied to the surface by a spherical tip, the number $2N$ (consider symmetry) of "involved" $k_{//}$ springs is simply given by a/l_0, where a is the contact radius. After indentation, the length of nth in-plane spring becomes L_n. The compression of nth perpendicular spring constant is Δz_n. Thus, the elongation of the nth in-plane spring constant Δl_n satisfies:

$$L_n^2 = l_0^2 + \Delta l_n^2 \qquad (4.1.1)$$

And it's easy to find that for an indentation of Δz_0

$$\Delta z_n = \Delta z_0 \times \frac{N-n}{N} \qquad (4.1.2)$$

If the tip radius is 100 nm and $\Delta z_0 = 0.3$ nm, the contact radius a is about 5 nm (approximated from Hertz model). Then a direct result is

$$\Delta z_0 << a, \Delta l_n << L_n \qquad (4.1.3)$$

With this simple approximation, we have

$$\Delta l_n \approx (\Delta z_n - \Delta z_{n+1}) \times \frac{\Delta z_0}{a} \tag{4.1.4}$$

With Eq 4.1.2 and 4.1.4, we can calculate the stress distribution among the two types of springs (in plane and perpendicular springs) given by the forces $F_\perp$ and $F_{//}$, respectively.

$$F_\perp = \Delta z_0 \times k_\perp \times [1 + 2\sum_{n=1}^{N} \frac{N-n}{N}] = \Delta z_0 \times k_\perp \times N \tag{4.1.5}$$

$$F_{//} = \Delta l \times k_{//} = k_{//} \times \frac{\Delta z_0}{N} \times \frac{\Delta z_0}{a} \tag{4.1.6}$$

The z-projection of $F_{//}$ then is

$$F_{//,z} \approx 2F_{//} \times \frac{\Delta z_0}{a} = 2k_{//} \times \frac{\Delta z_0}{N} \times \frac{\Delta z_0}{a} \times \frac{\Delta z_0}{a} \tag{4.1.7}$$

Setting $F_\perp + F_{//,z} = F_0$ as the basic constraint.

$$\frac{F_\perp}{F_{//,z}} = \frac{\Delta z_0 \times k_\perp \times N}{2k_{//} \times \frac{\Delta z_0}{N} \times \frac{\Delta z_0}{a} \times \frac{\Delta z_0}{a}} = \frac{k_\perp}{2k_{//}} \cdot \frac{N^2 a^2}{\Delta z_0^2} \tag{4.1.8}$$

If we use graphite as an example, then $N=a/2l_0=6$ nm/0.15nm=40 where l_0 is the length of sp^2 bond. Δz_0 is ~ 0.3 nm or less. So $(Na/\Delta z_0)^2= 0.64*10^6$. For graphite $k_\perp / k_{//} = E_\perp / E_{//}$ =36/1000 = 0.036, which is very small. However the product of the two, still makes $F_\perp / F_{//,z} = 10^4 \gg 1$. This means that since $F_\perp + F_{//,z} = F_0$, we can approximate $F_\perp = F_0$, i.e., the contribution to the normal indenting force is almost exclusively supported by the perpendicular springs, and it is independent of the in-plane bonds. In other words, *the normal force F_0 is mainly carried by the inter-layers interactions rather than the in-plane bonds*. Therefore, if we fit the indentation curves for a 2D layered material with Hertz (DMT) model, the Young's modulus obtained from the fit is almost equal to $E_\perp$. Notice that this simple analysis is valid only when $\Delta z_0 \sim 0.3$ nm, on the other hand we did not use any approximation for the values of the moduli $E_\perp$ and $E_{//}$. Furthermore, here we only analyzed a simplified one-dimensional-spring-system model, but a two-dimensional model will also give a similar result.

4.3 Semi Analytical Method (SAM)

A better insight of the contact pressure distribution as a function of the material elastic constants can be obtained using simulations with semi-analytical methods (SAM), which have proven their efficiency in describing the contact mechanics of anisotropic materials [103, 104]. SAM is an alternative to the Finite Element Method (FEM), quite close to the Boundary Element Method (BEM), suitable for continuum mechanics problems. The main advantage of BEM over SAM is that the first one is more versatile since it uses surface or volume integrals whatever is the shape of the volume of interest. Conversely SAM uses analytical solutions of these integrals for simple geometries (such as sphere or cuboid), which reduces the computation to a simple summation of elementary solutions. SAM consists of the numerical summation of elementary analytical solutions, such as the effect of a point load on a layered half-space, as far they are known. The difficulty for anisotropic elastic coating and/or substrate is that the set of equations to be solved requires manipulating complex numbers with conjugate pairs, leading to double roots when the material tends to behave as elastically isotropic. One of the advantages of SAMs when applied to contact problem compared to more widely used numerical techniques is the computing time which is at least one or two orders of magnitude shorter. For more details on SAM for the numerical procedure used to solve the contact problem for an elastic substrate coated with an anisotropic layer the reader may refer to [103, 104].

Here, we use SAM to simulate the force vs. indentation curves in graphite. We use graphite elastic constants found in literature, and we model the indentation of an AFM Silicon tip ($R = 100$ nm) in a graphite sample deposited on SiC. We use this configuration because the 2D materials studied here have been deposited either on SiC (epitaxial

graphene and epitaxial graphene oxide) or Si (conventional graphene oxide). For transversely isotropic material, there are 5 independent elastic constants:

$E_{//} = E_x = E_y = (C_{11}-C_{12}) (C_{11}C_{33}+C_{12}C_{33}-2C_{13}C_{13})/ (C_{11}C_{33}-C_{13}C_{13})$,

$E_\perp = E_z = C_{33}-2C_{13}C_{13}/ (C_{11}+C_{12})$,

$\nu_{zx} = C_{13}/ (C_{11}+C_{12})$,

$G_{xz} = C_{44}$,

$G_{xy} = (C_{11}-C_{12})/2$, $\nu_{xy} = \nu_{yx} = (E_x/G_{xy})-1$.

Notice that G_{xy} and ν_{xy} are correlated which means only one of them is independent. Graphite's elastic constants used here for SAM have been previously reported in literature [89] and they are $C_{11} = (1060\pm20)$ GPa, $C_{12} = (180\pm20)$ GPa, $C_{13} = (15\pm5)$ GPa, $C_{33} = (36.5\pm1)$ GPa and $C_{44} = (4.5\pm0.5)$ GPa. Giving for graphite $E_{//} = (1.06\pm0.02)$ TPa, and $E_\perp = (36.4\pm1)$ GPa. The SiC substrate was approximated as cubic with $E = 450$ GPa, $\nu=0.17$, and $G = E/2(1+\nu) =192.31$ GPa.
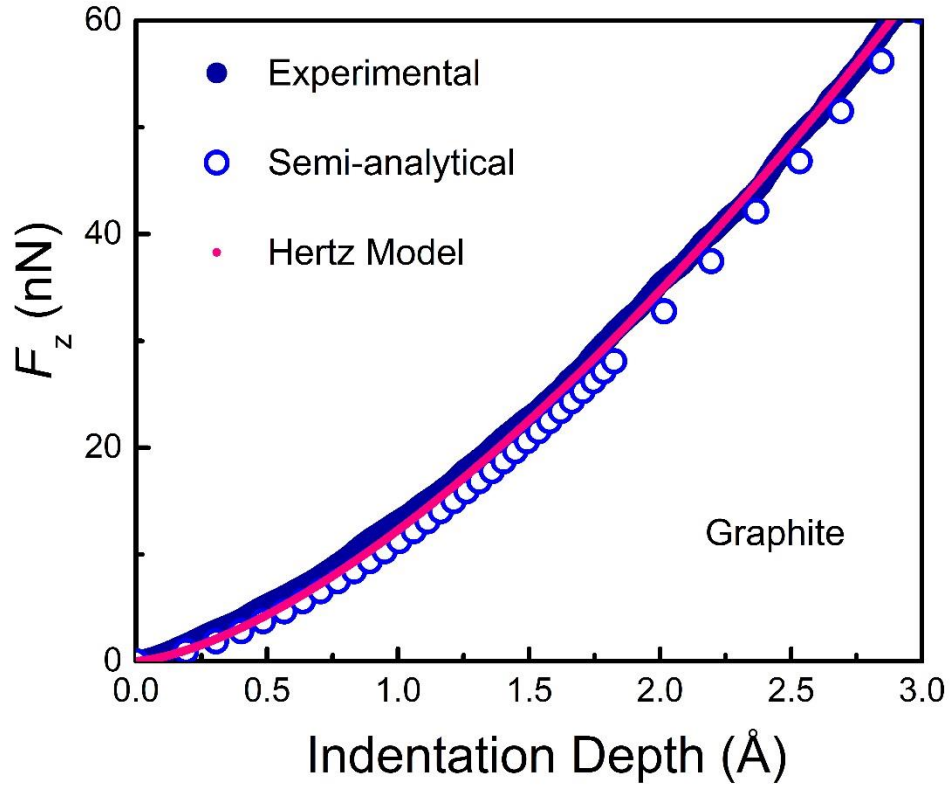
Figure 4.3.1: Experimentally measured indentation curves in HOPG (full circles), semi-

analytical model simulations of indentation in Graphite (open circles), and Hertzian fitting

(continuum line) of the indentation curves on HOPG. The indenting tip radius was 100 nm.

Reprinted with permission from [85]. Copyright 2015, Nature Publishing Group.

Figure 4.3.1 shows the results from the SAM simulations on graphite along with the experimental curves obtained by MoNI on a bulk sample of HOPG (the same in Fig. 4.1.1). In Fig. 4.3.1, the SAM simulated curve agrees extremely well with the experiments on HOPG, it is important to note that in the SAM simulations for graphite we use, according to literature, as in-plane Young's modulus $E_{//} = 1.046$ TPa, and as z-axis (perpendicular to the planes) Young's modulus $E_{\perp} = (36.4 \pm 1)$ GPa. Very interestingly, when Hertz model is applied to fit the experimental indentation curves measured on graphite (as shown in Fig. 4.3.1), as if graphite was an isotropic material, the result of the fitting procedure gives as the single isotropic modulus $E_{Hertz}^{HOPG} = (33 \pm 3)$ GPa, for $R = 100$ nm like the AFM tip radius. The Hertz model fitting curve is also reported in Fig. 4.3.1 to show the perfect agreement with experiments and SAM simulations. The Hertz model is therefore able with a simple fitting procedure to obtain a value of Young's modulus which is equal, within an error of 10%, to the most accepted value for the perpendicular-to-the-plane Young's modulus of graphite, i.e. $E_{\perp} = 36$ GPa.

The excellent consistency between experiment, simulation, and Hertz model when studying the indentation of 2D films with extremely small indentation depths is a direct consequence of the following SAM observations. If we consider sub-interlayer distance indentations in a transversally isotropic (orthotropic) material having $E_{\perp} = E_{Hertz}$ and $E_{//}$ varying up to one order of magnitude compared to E_{Hertz}, we find that the contact pressure and contact area for a given pressure remain almost the same as in an isotropic material having $E = E_{Hertz}$. On the other hand, the contact pressure changes dramatically compared to the isotropic case when varying $E_{\perp}$ in the same range while maintaining $E_{//} = E_{Hertz}$. Overall these results indicate that for sub-nm AFM indentations, much smaller than the

film's thickness, the force vs. indentation curves are very sensitive to $E_\perp$, and almost independent of the value of $E_{//}$.

In particular, the contact pressure distribution profiles in case of sub-nm indentations for the Hertz model in case of an isotropic material with $E_{Hertz} = 33$ GPa (the value of $E_\perp$ in graphite), and in the case of $E_{Hertz} = 1.046$ TPa (the value of $E_{//}$ in graphite) are plotted in Fig. 4.3.2 along with the SAM simulations for bulk graphite and 50 nm thick graphite. It can be easily concluded that the pressure distributions for an isotropic material having $E = 33$ GPa, bulk graphite, and 50 nm-thick graphite are almost all the same. On the other hand, the pressure distribution changes dramatically when considering an isotropic material with $E = 1.046$ TPa. We conclude that when studying 2D materials with sub-nm indentations, the Hertz model is an extremely simple and accurate model to fit the experimental AFM indentation curves and obtain the perpendicular Young's modulus $E_\perp$ of 2D films having a thickness larger than the indentation depth.
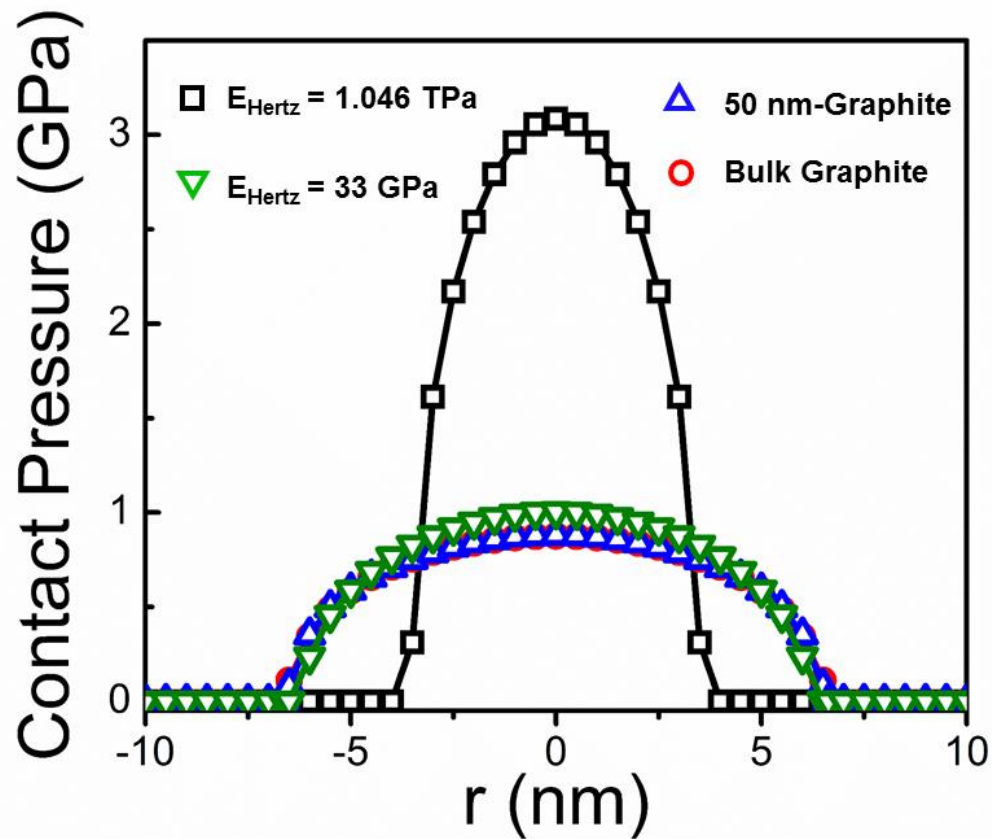
Figure 4.3.2: Contact pressure distribution profiles for Hertz contacts and SAM simulations of indentation in graphite. Note that for bulk graphite and for a graphite film 50 nm thick, the SAM simulations and the contact distribution profiles almost overlap. Reprinted with permission from [85]. Copyright 2015, Nature Publishing Group.

4.4   Intercalated Water in Graphene Oxide

4.4.1   MoNI on Epitaxial Graphene Oxide

To prepare Epitaxial Graphene Oxide (EGO) samples, the 10-layer epitaxial graphene samples on SiC chips (details on the epitaxial graphene growth can be found in Chapter II) are then directly oxidized shortly after preparation by using a milder Hummers' method [31, 52, 60, 105] as mentioned in Chapter II, which avoids graphene exfoliation and dispersion in solution. Once the reactions are terminated, EGO films on the SiC chips are picked up from the solution and rinsed with DI water for 1 minute. During this process, water molecules are intercalated between the GO layers. The EGO films, 10-layers thick, are finally blow-dried by nitrogen gas. Figure 4.4.1 is an AFM image of the EGO sample measured in this section and its X-Ray diffraction (XRD) spectroscopy. The interlayer distance increases from 3.4Å (graphene) to 9.3Å after oxidation due to the intercalated water [60].

We did MoNI on this EGO sample under different Relative Humidity (R.H.) by controlling the Nitrogen gas amount in the AFM chamber (Fig. 4.4.2). Figure.4.4.3 shows the measured out-of-plane Young's modulus E_z as a function of R.H.. Based on the results shown in Fig. 4.4.3, we can firmly say that the interlayer elasticity of EGO is ~ 22 GPa and does not vary with the environmental relative humidity.
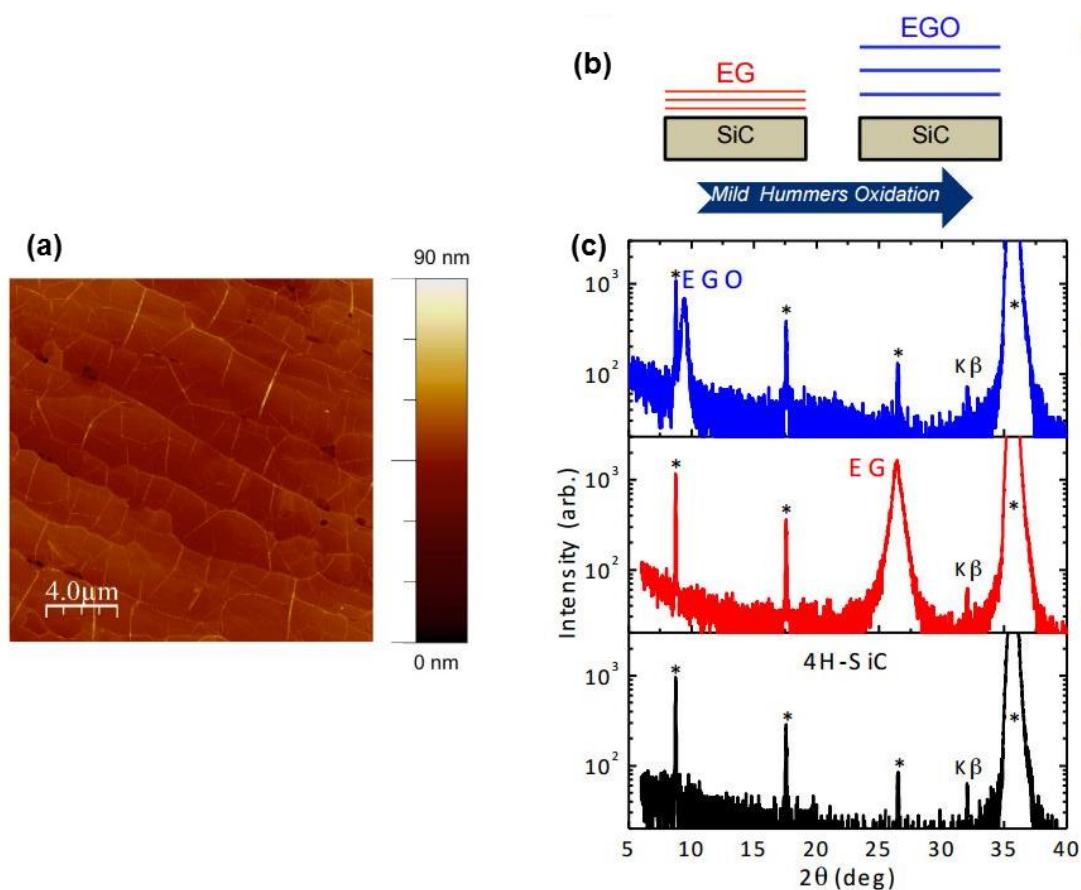
Figure 4.4.1: (a) AFM topographical image of the EGO sample measured in this section. (b) Schematic illustration of the Hummer's method. (b) XRD spectra of the 11($\pm$1)-layer EGO film in (a) (blue solid line), a 12($\pm$1)-EG film (red), and a bare 4H-SiC (000-1) substrate (black). The asterisks indicate peaks arising from the substrate. Peaks of EGO and EG are located at $2\theta = 9.46$ deg and $2\theta = 26.42$ deg and are corresponding to interlayer distances of 9.35 Å and 3.38 Å, respectively. Reprinted with permission from [60]. copyright 2014, Wiley Online Library.

96
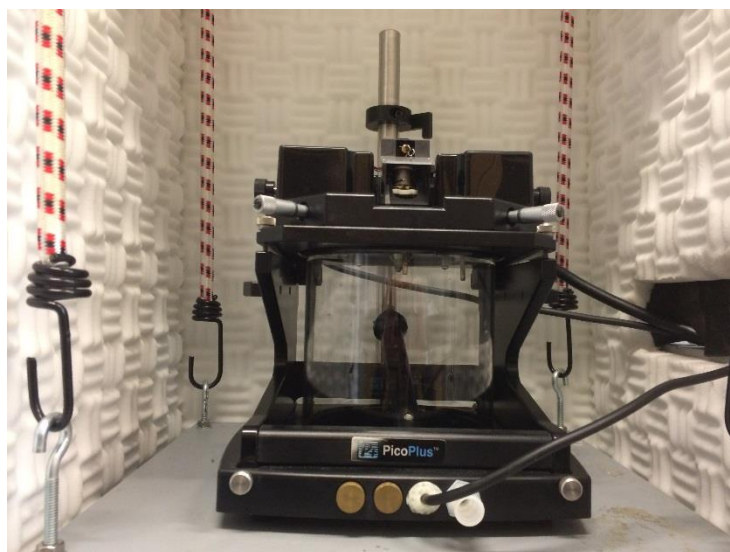
Figure 4.4.2 The environmental chamber. Relative humidity inside can be controlled by pumping Nitrogen.
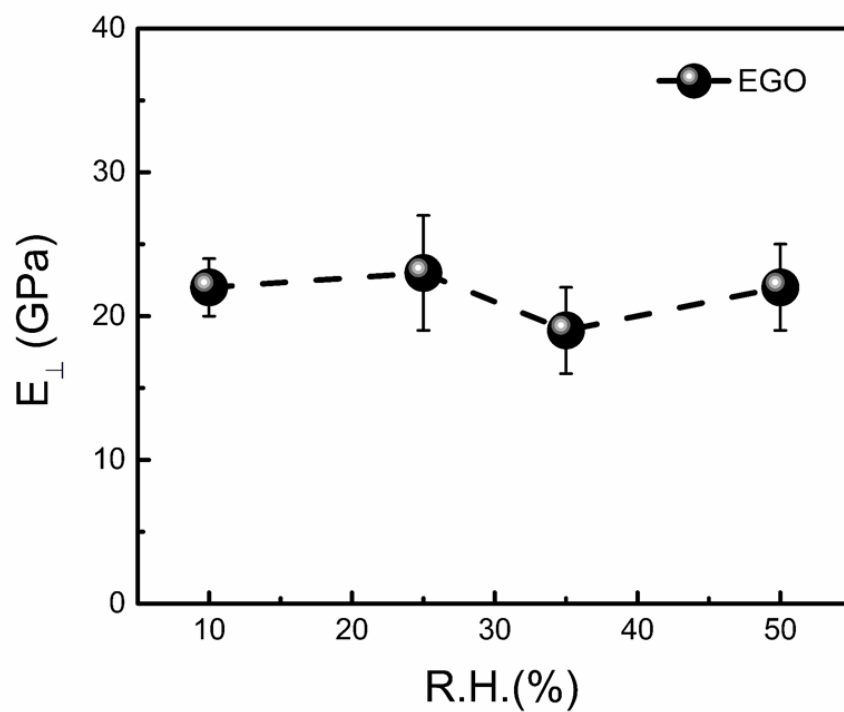
Figure 4.4.3: The out-of-plane Young's modulus $E_\perp$ of EGO vs. relative humidity (R.H.).

4.4.2   MoNI on Conventional Graphene Oxide

Besides EGO, we also performed MoNI on conventional graphene oxide (Conventional GO) under different R.H. The conventional graphene oxide films are prepared by drop casting colloidal GO dispersion on a Si chip and leaving it to dry at 80°C. Stable colloidal GO dispersions are produced by modified Hummers' method. Once the reaction is terminated, the oxidized portion is separated and cleaned from unoxidized graphite and other residual species. The cleaning is performed by centrifugation of the obtained suspension at 7800 rpm for 30 minutes in order to remove both the acidic content and ions. The solid content is collected and redispersed with DI H_2O. This operation is repeated in sequence until the pH of the supernatant raised close to neutrality. At that point, the exfoliation of graphite oxide is performed by prolonged and vigorous shaking, forming a brownish colloidal suspension of GO flakes. The subsequent collection of the purified supernatant results in stable aqueous GO suspensions, which are drop casted on Si to form a film with a thickness of 40-50 nm [105].

Figure 4.4.4 summarizes the out-of-plane Young's modulus of conventional GO acquired by MoNI at different R.H.. Unlike EGO, conventional GO's $E_\perp$ starts with 21GPa at low R.H. (10%), similar to the value of EGO; then it increases with R.H., reaching the maximum value of 35 GPa at ambient R.H. (25%); finally $E_\perp$ drops to 23 GPa as R.H. keeps increasing. To understand the origin of the very different behaviors of interlayer perpendicular elasticity in conventional GO and epitaxial GO, we have performed density functional theory (DFT) calculations on the elasticity of GO with a different amount of intercalated water.
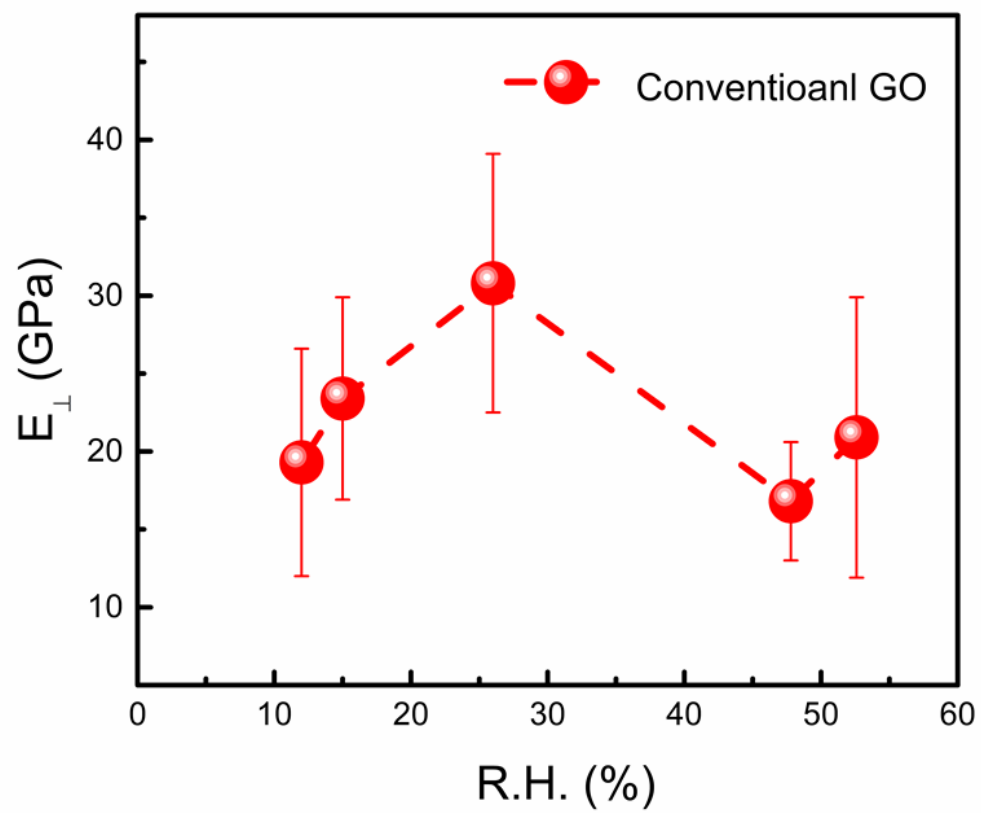
Figure 4.4.4: The out-of-plane Young's modulus $E_\perp$ of conventional GO vs. relative humidity (R.H.).

4.4.3 Results Analysis and Density Functional Theory (DFT) Calculations

Density functional theory (DFT) calculations in this section were carried out by our collaborators - Prof. Bongiorno and his group members using the *PWscf* code of QUANTUM Espresso toolkit [106]. We used a plane-wave basis set with an energy cutoff of 120 Ry, norm-conserving pseudopotentials for all atomic species [107] , and the exchange-correlation functional proposed by Perdew, Burke, and Ernzerhof [108]. We used a 3*3*3 Γ-centered Monkhorst-Pack meshes to sample the Brillouin zone of the supercells of graphene oxide models. Integration over the k-points was carried out with a Fermi-Dirac spreading of 0.002 Ry. Self-consistent electronic iterations proceeded until the energy difference is less than 10^{-7} eV. The ionic minimization was performed until the energy difference is less than 0.002 eV and the forces on each atom is less than 0.05 eV/Å. To account for the London dispersion forces in layered materials, we adopted the semi-empirical DFT-D2 approach proposed by Grimme [109] and implemented in QUANTUM-Espresso by Barone [110]. This DFT-D2 scheme was tested on graphite, and it gave an interlayer distance of 3.25 Å and an out-of-plane Young's modulus of 42.1 GPa, in good agreement with the experimental values [111].

DFT calculations have been performed on model structures of graphene oxide consisting of periodic stack of graphene layers fully oxidized by either hydroxyl or epoxide groups, including increasing concentrations of water molecules, and presenting AA stacking. For each model, we used a DFT-D2 scheme to perform a full structural optimization and determine the zero-temperature interlayer spacing. Subsequently, we applied a pressure and used DFT-D2 to estimate the z-axis Young's modulus from the
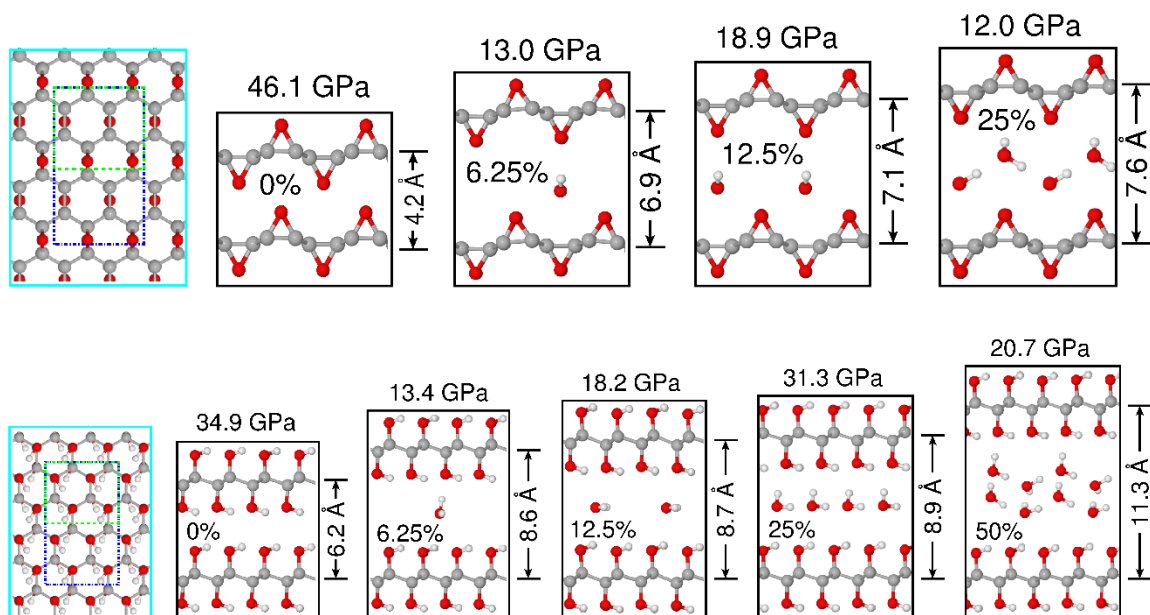
Figure 4.4.5: Top: Graphene oxide models fully covered by hydroxyl groups and including an increasing amounts of water. The first panel on the left shows the planar structure of the oxide layers. The dashed-line boxes indicate the planar dimensions of the supercells for the models with 0%, 12.5%, 25% and 50% water (green), and the model with 6.25% water (blue). The water content, and the computed interlayer distance and out-of-plane Young's modulus by DFT-D2 are reported inside, on the right, and on top of each model structure, respectively. Bottom: Same as (a) for graphene oxide models fully covered by epoxide groups. Reprinted with permission from [85]. Copyright 2015, Nature Publishing Group.

energy vs. displacement curves. The oxide layers were arranged in "AA" stacking geometry. An increasing amount of water molecules of 0%, 6.25%, 12.5%, 25% and 50% (with respect to the total number of C atoms) were intercalated in-between the layers for the models with hydroxyl functionalization. The GO models with epoxide functionalization include 0%, 6.25%, 12.5% and 25% water. For each model structure, we used the primitive unit cell as the supercell, including one GO layer, and the planar dimensions shown in Fig. 4.4.5. We used the DFT-D2 scheme to optimize the electronic charge density, ionic positions, and both lateral and vertical cell dimensions for all the GO models. A summary of the DFT results reporting $E_\perp$ and interlayer distance as a function of intercalated water percentage for GO structures fully oxidized with hydroxyls and epoxides are reported in Table 4.4.1.

Figure 4.4.6(a) shows the calculated F_z vs. displacement curves at varying intercalated water content for the case of graphene fully oxidized with hydroxyl groups, because previous experiments have shown that conventional GO films are mainly composed of hydroxyls groups. In comparison, Fig. 4.4.6(b) presents the experimental indentation curves on conventional GO at different relative humidity (R.H.). Figure 4.4.6(c) and (d) shows the resulting $E_\perp$ as a function of intercalated water percentage compared to carbon (for DFT calculations) and relative humidity (for MoNI experiments), respectively. A summary of the experimental results is also reported in Table 4.4.2. The agreement between experiments and DFT calculations is striking. DFT calculations and experiments show that $E_\perp$ increases with the amount of intercalated H_2O molecules (and relative humidity), reaching a maximum value of about 31 GPa at 25% of H_2O, and 35 GPa at R.H. = 25%, for the DFT calculations and indentation experiments, respectively. The

102

perpendicular elastic modulus then decreases down to 20 GPa at 50% of water, and 23 GPa at 50% relative humidity, for the DFT calculations and indentation experiments, respectively. We remark that while the presence of a maximum in the perpendicular modulus found in both experiments and calculations is a key result, the excellent quantitative agreement between water content (from DFT) and relative humidity (from experiments) might be only a coincidence. The DFT calculations clearly give an insight of the atomistic origin of the behavior of $E_\perp$ as a function of intercalated water. DFT calculations show that the interlayer distance and perpendicular Young's modulus in GO change abruptly between the case of dry layers and a multilayer film including small amount of H_2O (<6%), while more gradual variations of these physical properties are obtained for increasing the water content between 6.25% and 25% (Fig. 4.4.6c, and Table 4.4.2). In particular, $E_\perp$ drops from about 35 GPa (close to EG) in dry films to about 11-14 GPa when the layered structure includes 6.25% of H_2O. This behavior can be understood by considering that when the amount of water is only a few percentages of the Carbon amount, H_2O molecules swell the graphene structure increasing the interlayer distance from 3.4 Å to about 6.2 Å, but leaving the interlayer space mainly empty and therefore producing a soft structure with a low perpendicular elastic modulus. This interlayer modulus increases with increasing amount of water, which fills the interlayer space without changing too much the interlayer distance (Table 4.4.1). However, at 25% of water, H_2O molecules have completely filled a water layer in between the layers, and this situation corresponds with the maximum in perpendicular elastic modulus. Above 25% of water, the perpendicular elastic modulus decreases because a second water layer starts to form in between the layers further swelling and softening the GO structure. Thanks to this

explanation it is now possible to understand the different values of $E_\perp$ in epitaxial GO compared to conventional GO. EGO is not a porous structure and water intercalation is minimal [60] and independent of humidity. For this reason we find that $E_\perp$ in epitaxial GO remains constant and ~ 22 GPa for all R.H.. On the other hand, conventional GO is a porous structure[3] where the amount of intercalated water can change depending on the humidity, therefore in agreement with the DFT calculations we observe a maximum in conventional GO when varying the R.H..

DFT Calculations	All Hydroxyls		All Epoxides	
Water fraction (%)	Interlayer distance (Å)	$E_\perp$ (GPa)	Interlayer distance (Å)	$E_\perp$ (GPa)
0	6.2	34.9	4.2	46.1
6.25	8.6	13.4	6.9	13.0
12.5	8.7	18.2	7.1	19.2
25	8.9	31.3	7.6	14.3
50	11.3	20.7	N/A	N/A

Table 4.4.1: DFT reported $E_\perp$ and interlayer distance as a function of different fractions of intercalated water for GO structures fully oxidized with hydroxyls and epoxides.

Relative Humidity		10 ± 2 %	15 ± 3 %	25 ± 3 %	35 ± 3 %	50 ± 3 %
$E_\perp$ (GPa)	10-layer EGO	22 ± 3	-	23 ± 4	19 ± 3	22 ± 3
	Conventional GO	21 ± 6	26 ± 6	35 ± 10	-	23 ± 7
	10-layer EG	-	-	36 ± 3	-	-

Table 4.4.2: Summary of the experimental results of $E_\perp$ at different relative humidity.
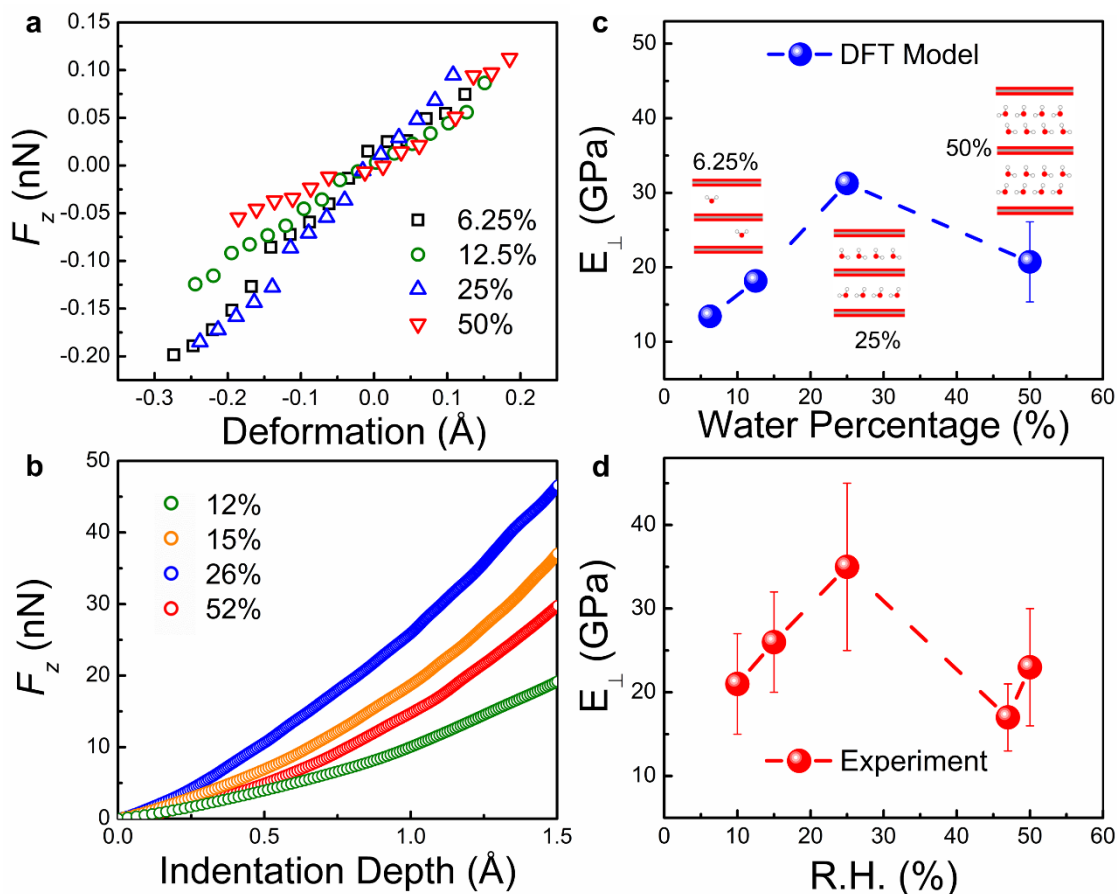
Figure 4.4.6: DFT and experimental results for conventional GO films. (a), the DFT calculated F_z vs. displacement curves for different water content in graphene fully oxidized with hydroxyl groups. (b), experimental F_z vs. indentation depth curves at different relative humidity in conventional graphene oxide. All the curves were obtained with the same AFM tip. (c-d), Experimental and DFT results of $E_\perp$ of GO as a function of water content and relative humidity, respectively. The insets are cartoons of the corresponding atomistic structures showing how water molecules fill the interlayer spacing. Each experimental point of $E_\perp$ is an average value on more than 30 different measurements. Reprinted with permission from [85]. Copyright 2015, Nature Publishing Group.

CHAPTER 5.   DIAMENE – A NEW ULTRA STIFF PAHSE OF GRAPHENE

The formation of diamond from graphite is theoretically enigmatic and experimentally extremely challenging, since it requires high pressures and temperatures above 1000K. In this chapter, we present the most recent MoNI experiments and density functional theory (DFT) calculations showing that at room temperature, pressures in the order of 1 GPa can induce the formation of single layer diamond from two-layer epitaxial graphene. Upon indentation with a nano-size probe, two-layer epitaxial graphene on SiC (0001) displays a stiffness equal or larger than that of diamond. This phenomenon vanishes for graphene films thicker than 5 layers, demonstrating a unique phase diagram for two-layer epitaxial graphene. DFT calculations confirm that two-layer graphene on SiC (0001) exhibits small to vanishing energy barriers for the graphitic-to-diamond phase transition. This barrier depends on the graphene/SiC interface and the possibility to saturate diamond's dangling bonds.

An article reporting the results in this chapter has been submitted to *Nature Nanotechnology*.

5.1   From Graphite to Diamond

5.1.1   *Traditional Synthesis Method*

Diamond has been intensively studied in both academic and industrial fields for hundreds of years due to its superlative mechanical, thermal and optical properties [112]. For example, diamond is one of the best thermal conductors (2×10^3 W m^{-1} K^{-1}), transparent

over a wide range of wavelengths and one of the hardest materials (Young's modulus ~ 1TPa). Numerous attempts have been made to synthesize thin diamond films by transforming precursor materials - mainly graphite [112]. The most commonly used method is simply applying high pressure and high temperature (HPHT) on the diamond seeds (e.g., graphite). However, this graphite – diamond transition requires extremely high temperature (above 1000°C) and high pressure (several GPa or even higher) since both graphite and diamond are thermodynamically stable at ambient temperature and pressure. Another widely used method is chemical vapor deposition (CVD), which creates a hydrogen diluted precursor gas (usually CH_4) over a substrate onto which the carbon atoms deposit to form diamond. Also, CVD method still requires rather high temperature (higher than 1000K) to ensure the formation of diamond instead of amorphous carbon. Other methods include microwave plasma from gas phase, sonication of graphite, etc.

5.1.2   Hydrogenation Method – Diamane

Graphene is also found to be a possible precursor candidate to produce diamond films. For example, by exposing graphene under hydrogen plasma, strong signal of C=C sp^2 bonds breaking and increase of C-C sp^3 hybridizations has been observed [113-115]. This decorated atomic-thick Carbon film with C-H and C-C sp^3 bonds is given a name "*diamane*" inspired by the naming of *graphene* [116]. However, as the most common method to produce diamane, hydrogenation is still not very convenient since it needs massive energy to prepare hydrogen plasma and may take up to 2 hours to achieve full saturation. The dehydrogenation also requires long time and high temperature [113, 114, 117]. Furthermore, yet no experimental study has been conducted aiming towards the

mechanical properties of diamane to confirm if diamane inherits diamond's unique super-stiffness and hardness.

5.2 Pressure Induced Ultra Stiff Phase of Graphene on SiC (0001) – Diamene

In this section, we introduce our most recent results on the fingerprint of formation of single-layer sp^3 diamond from bilayer epitaxial graphene on SiC (0001) by Angstrom - indenting experiments.

5.2.1 Preparation and Characterization of Epitaxial Graphene

Epitaxial graphene samples studied in this chapter were grown on 4H-SiC on axis wafers by the confinement controlled sublimation (CCS) method [51]. The wafers, purchased at CREE, are CMP polished on the growth face. Temperature and time were optimized to produce few graphene layers on the (000-1) -face (C-face) [24], or a single graphene layer on the (0001)-face (Si-face), around 1450 °C for 7 minutes and 1550 °C for 20 minutes, respectively. On the Si-face the first carbon layer is known as the buffer layer, and has a graphitic atomic structure but a semiconducting electronic structure due to its interaction with the (0001)-SiC interface. Sample quality and homogeneity were controlled by atomic force microscopy (topography, friction force and electrostatic force microscopy) and Raman spectroscopy. Details can be found in [24], [55] and in [118].
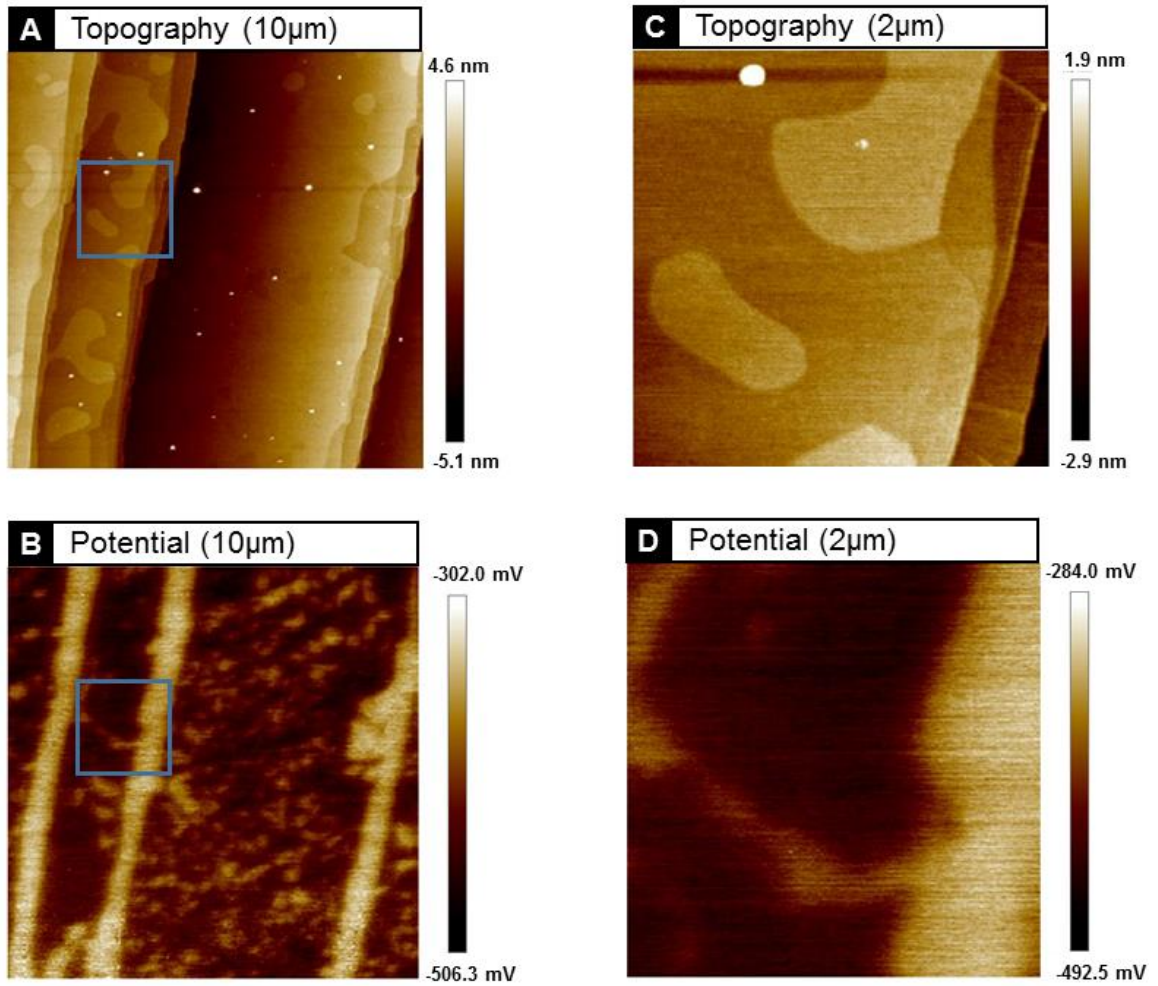
Figure 5.2.1: KPFM characterization of a non-uniform epitaxial graphene sample on SiC (0001). (A) Topographical and (B) corresponding surface potential images of a 10μm × 10μm area. (C) Topographical and (D) surface potential images of a zoom-in area (2μm × 2μm) as shown by a blue square in (A) and (B).

Kelvin Probe Force Microscopy (KPFM) is a unique AFM module that can measure the work function or surface potential difference between the metal-coated (usually Pt/Ir) probe and the sample surface. Previous study has demonstrated that the local work function of EG will increase as it gets thicker [119]. Figure 5.2.1 (a, b) are topographical and potential images of a 10μm × 10μm area of a particularly non-uniform EG sample on SiC (0001), respectively. A set of 2μm × 2μm zoom-in images are also shown in Fig. 5.2.1 (c, d). EG was uniformly distributed on the SiC steps which were automatically formed when SiC was heated. The SiC step height is around 5nm. The highest surface potential on the step edge indicates that EG is thickest there. Previous research has pointed out that EG growth tends to begin where the substrate has more defects or asymmetries which can play the role of growth nucleus [51]. As a result, EG growth is fastest on the step edge which has the geometrical asymmetry and graphene film is usually much thicker than the graphene on the flat step terraces. There are roughly two surface potential "populations" (dark and light areas) on the step terraces, revealing that there are at least two different layer numbers of EG.

To further investigate the number of graphene layers, Transmission Electron Microscopy (TEM) and Scanning Transmission Electron Microscopy (STEM) were also applied. Figure 5.2.2 shows TEM (a, b) and STEM (c, d) images of the same EG sample in Fig 5.2.1, taken in different areas. The SiC substrate is indicated in the Fig. 5.2.2, the lightest part in (c, d) is the Pt protection and the dark part between SiC and Pt is EG. Fig. 5.2.2 (a, c) and (b, d) show the buffer-layer and the single-layer EG, respectively. This sample surface is mainly covered with buffer-layer or single-layer EG. Combing the TEM and STEM images with the KPFM images we can tell that the areas with relatively lower
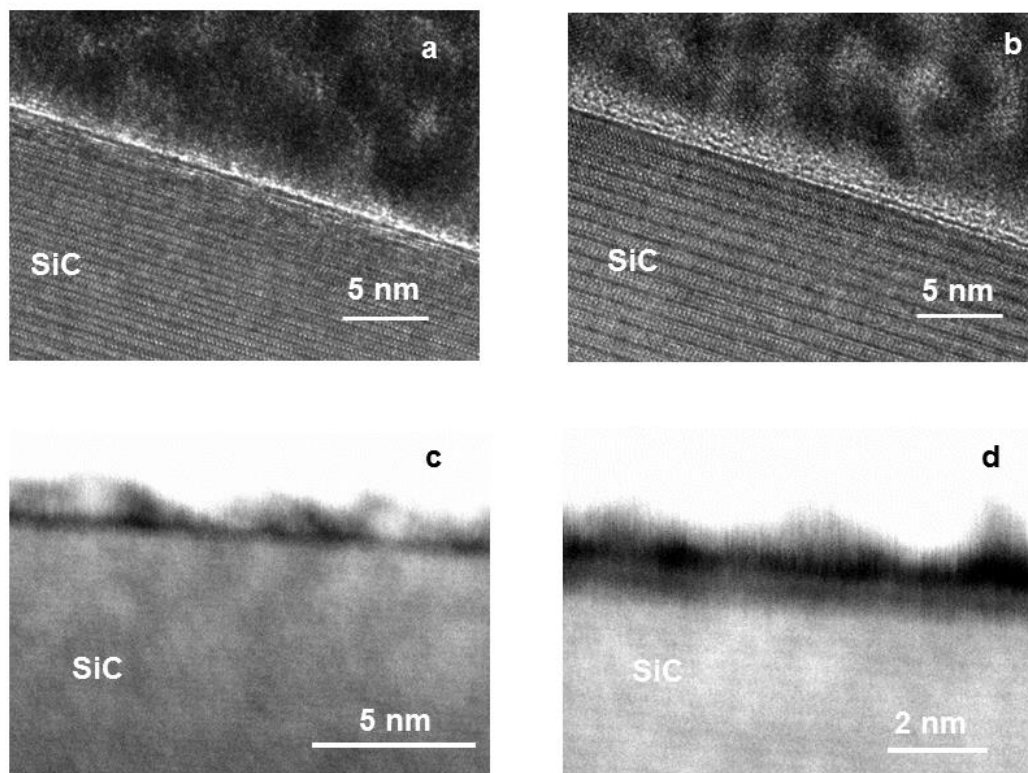
Figure 5.2.2: TEM (a, b) and STEM (c, d) images of the non-uniform buffer/two-layer epitaxial graphene sample in Fig. 5.2.1. (a, c) buffer layer. (b, d) 2-layer EG. The light bands between SiC and Pt coating correspond to graphene layers.

and higher surface potential are the buffer-layer (or 0th layer) and the very first few layers (< 3) of graphene, respectively.

Raman spectrums were also taken on different areas on this non-uniform EG sample as shown in Fig. 5.2.3. Two 2D peaks were found at 2685 cm^{-1} and 2737 cm^{-1}, indicating areas with different layer numbers.
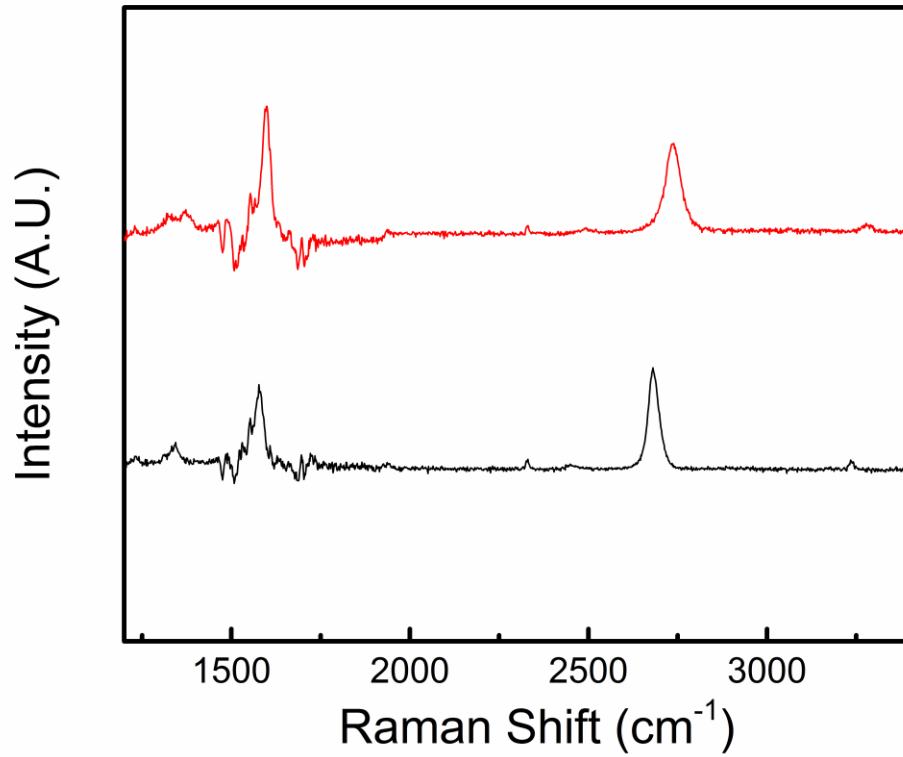
Figure 5.2.3: Raman spectrums of the second epitaxial graphene sample. The black and red curves are Raman spectrums taken at two different regions. Two different 2D peaks at ~2737 cm^{-1} and ~2685 cm^{-1} are observed.

We applied MoNI (Å - indentation) on EG films with different number of layers, precisely 10L, 5L, 2L and the first graphene-like layer on SiC (0001), also termed as buffer layer. To determine the number of layers in the different EG samples, we performed TEM measurements of the respective cross sections. The TEM images are shown with the corresponding indentations curves in Fig. 5.2.4. All the indentation curves in Fig. 5.2.4 are an average over more than 10 measurements on different regions of different samples. Here we directly use the indentation curves shown in Fig. 4.1.1 for 10-layer epitaxial graphene (10L-EG) and in Fig. 4.3.1 for bulk Highly Ordered Pyrolytic Graphite (HOPG), as shown in Fig. 5.2.4(b) together with a cartoon of the method (Fig. 5.2.4(a)). In Figure 5.2.4(d), we present the indentation curve for 5-layer EG on SiC (0001), as well as the indentation curve measured on bare SiC. 5L-EG is much softer than SiC since we are still probing the soft out-of-plane modulus of a graphitic system with an out-of-plane Young's modulus of 36 GPa as shown in Chapter IV. However, 5L epitaxial graphene on SiC displays slightly steeper (stiffer) curves than 10L-EG, very likely because of the influence of the very stiff SiC substrate. When we measure the very first graphene-like layer on SiC (0001) (Fig. 5.2.4(F)), which is covalently bonded with the SiC substrate and is referred to as *buffer layer*, we obtain almost the same but slightly softer indentation curves than in bare SiC. Actually the exact nature of the buffer layer is still unclear and under investigation in the scientific community [100]. This behavior is in agreement with physical intuition: when a film on a rigid substrate is thin enough the indentation measurements will sense mostly the stiffness of the underlying substrate. Overall the indentation curves for 10L, 5L and buffer layer graphene on SiC follow a very predictable behavior, and we expected that two-layer

epitaxial graphene (i.e., buffer layer plus one graphene layer) would have displayed indentation curves with intermediate values between 5L and the buffer layer. However, very surprisingly when we indent two layers of graphene, as shown in Fig. 5.2.5(a) with the corresponding TEM image (Fig. 5.2.5(b)), we obtain force vs. indentation curves which are steeper than the ones on bare SiC, and they can only be understood with a structural change in two-layer graphene. The measured astonishingly high stiffness of two-layer epitaxial graphene is even larger than the Hertzian prediction for indentation curves of the same silicon AFM probe on diamond, as shown in Fig. 5.2.5(a). Previous theoretical studies of indentation in suspended single layer graphene indicated that observed experimental instabilities could be understood by covalent bond formed between the indenter and graphene [120]. Hypothesizing that indeed bonds are formed between the probe and graphene, we have used the Hertz model to predict force vs. indentation curves in diamond when the probe is no more pure Si but covered with a SiC film. More specifically, we use the Hertz model to calculate the indentation curve when a SiC spherical probe indents a diamond sample. The resulting calculated indentation curve is reported as the purple line in Fig. 5.2.5(a), which overlaps very well with the experimental curve for 2L EG. Thus, we conclude that two-layer graphene is undergoing a structural change into a diamond-like sp^3 phase. The experiments also indicate that this phase change cannot be observed when the graphene film is too thick (more than 5 layers). Furthermore, the absence of ultra-stiffness in the single buffer graphene layer proves that two Carbon atomic layers are required to form a "diamond layer", here we gave a new name - "*diamene*".
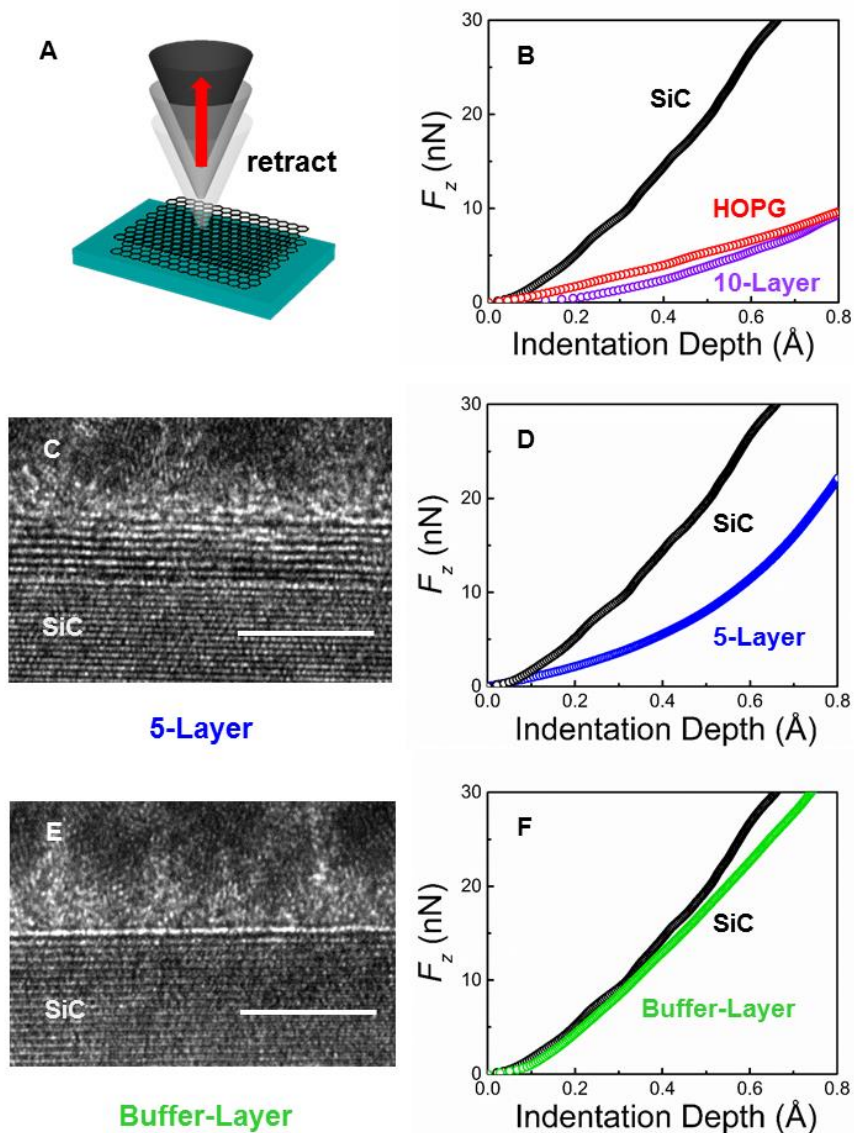
Figure 5.2.4: TEM images and indentation curves for multi-layer epitaxial graphene and buffer layer on SiC. (A) Schematics of the experiments performed in retracting mode. (B) Indentation curves of SiC, HOPG and 10L graphene on SiC(000-1). (C) TEM image and (D) indentation curve of 5L graphene on SiC (0001). (E) TEM image and (F) indentation curve of the buffer-layer on SiC (0001). The scale bars in (C) and (E) are both 5 nm.
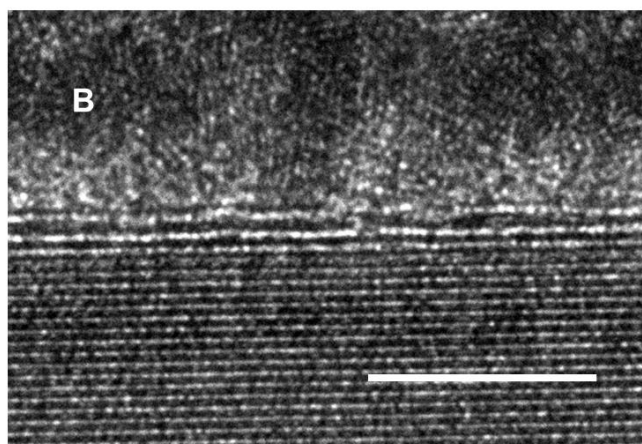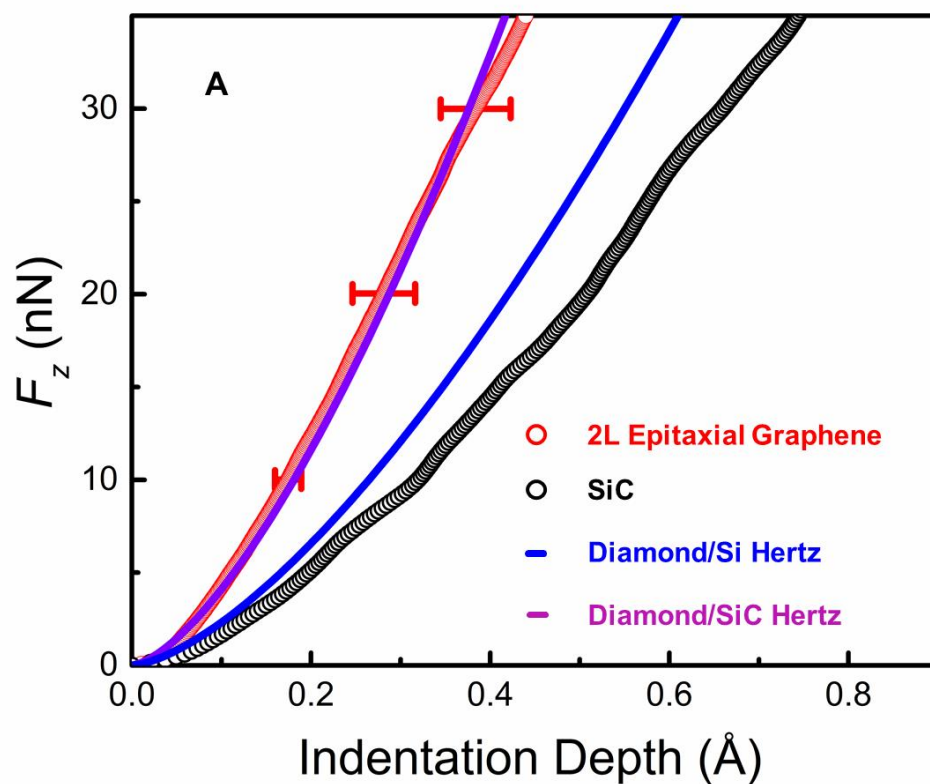
Figure 5.2.5: Ultra-stiff two-layer epitaxial graphene upon indentation. (A) Experimental indentation curves of two-layer EG, SiC and a theoretic Hertzian curve for a Si (blue) and SiC (purple) probe indenting diamond. (B) TEM image of two-layer EG, the scale bar is 5 nm.

5.2.3   Micro Hardness Measurements

Diamond does not only have a high stiffness but also a substantially high hardness. To further prove the existence of the diamene phase induced in two-layer epitaxial graphene, we have performed micro-hardness measurements with a diamond AFM indenter attached to a sapphire cantilever (TD10780, MICRO STAR). Upon indentation with a load of 6 μN (spring constant 80±40 N/m and tip radius ~ 100 nm) and with subsequent AFM topographic imaging, we were able to identify a shallow residual hole in SiC (diameter ~ 40 nm), a larger and deeper hole in 5-layer epitaxial graphene (diameter ~ 60 nm) and no residual indent at all in 2-layer graphene as shown in Fig. 5.2.6. The hole depths are around 500 pm and 1000 pm for SiC and 5-layer graphene, respectively. When we tried to apply larger loads on the 2-layer graphene, the diamond tip was worn out.
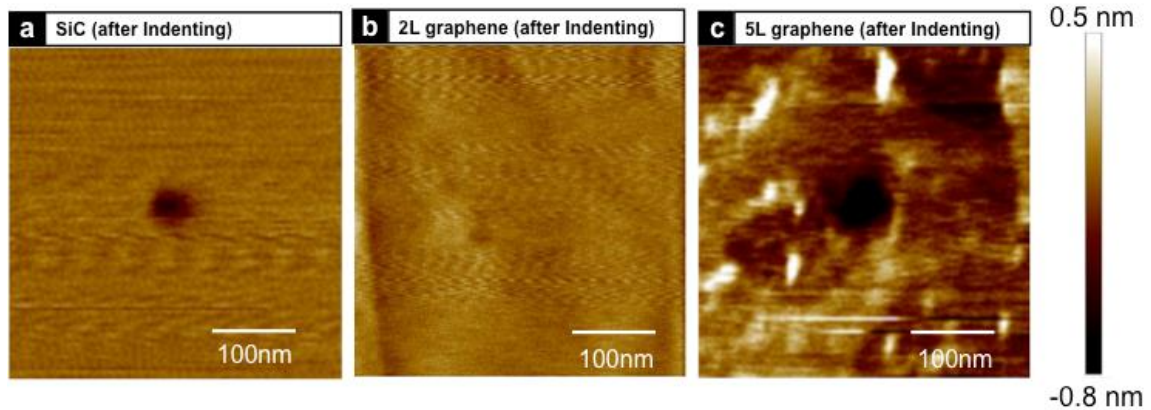
Figure 5.2.6: Micro-Hardness measurement. AFM topographic images (after micro-indentation) of (a) SiC, (b) 2-layer epitaxial graphene on SiC (0001) and (c) 5-layer epitaxial graphene on SiC (0001). The maximum load was 6 μN with an approaching speed of about 5μm/s.

5.2.4   Density Functional Theory (DFT) Calculation and Discussion

To validate our experimental analysis, our collaborators - Prof. Bongiorno and his group members used DFT calculations to model the complex process of a two-layer epitaxial graphene film undergoing nanoindentation by an AFM probe. To this end, and due to a lack of chemical information about the contact between probe and Carbon film, we consider model structures consisting of a two-layer graphene film sandwiched by simplistic representations of the SiC (0001) surface. Each one of the two mirroring surface models consists of one SiC layer, with Si atoms in contact with a graphene layer and Carbon atoms saturated by Hydrogen atoms (Fig. 5.2.7). In spite of its simplicity, this atomistic model allows to mimicking the occurrence of both a buffer layer in contact with the Si-face of SiC and the irregular chemical interaction between a partially reactive AFM probe (or environment) and the Carbon film surface. We use these model structures to determine from DFT the energy profile associated to the nanoindentation-induced homogeneous transformation of two-layer epitaxial graphene to diamene. In practice, this is achieved by carrying out DFT structural-optimization calculations of a sequence of model structures with an increasingly smaller distance between the mirroring SiC-H layers. In each of these calculations, total energy and optimal ionic configuration of graphene and SiC layers are determined by keeping fixed the positions of the terminal H atoms, and to explore qualitatively how the two combined factors (i.e. the atomic registry between buffer layer and SiC surface, and the steric, reactive interactions between probe and Carbon film surface) influence the energy cost associated to the structural transformation, we compute the energy curve for several model structures of this system, with increasingly larger surface areas and different bonding patterns at the interface between the buffer layer and

the Si-face of SiC. The energy profile computed by DFT for one of such model structures is shown in Fig. 5.2.7. Overall, our DFT modeling study corroborates the experimental analysis, showing that the homogenous phase change of a two-layer epitaxial graphene to diamene is indeed achievable at room temperature and upon compression by an AFM probe with local pressures of ~ 1 GPa. In particular, our calculations show that the energy barrier separating the two phases ranges between the thermal energy available at room temperature (Fig. 5.2.7) down to vanishing values, depending on the geometry of the bonding pattern at the graphene/SiC interface. This also suggests that, while the occurrence of buffer layer in chemical contact with the Si-face of SiC is key to the formation of diamene, the chemical interaction between probe and Carbon film might be key to favor the phase transformation.

In conclusion, we have found that two-layer epitaxial graphene on SiC displays an extremely high stiffness, equal or larger than diamond. Evidence of a room temperature pressure induced reversible transformation of two-layer epitaxial graphene into single layer diamond is observed experimentally and confirmed theoretically.
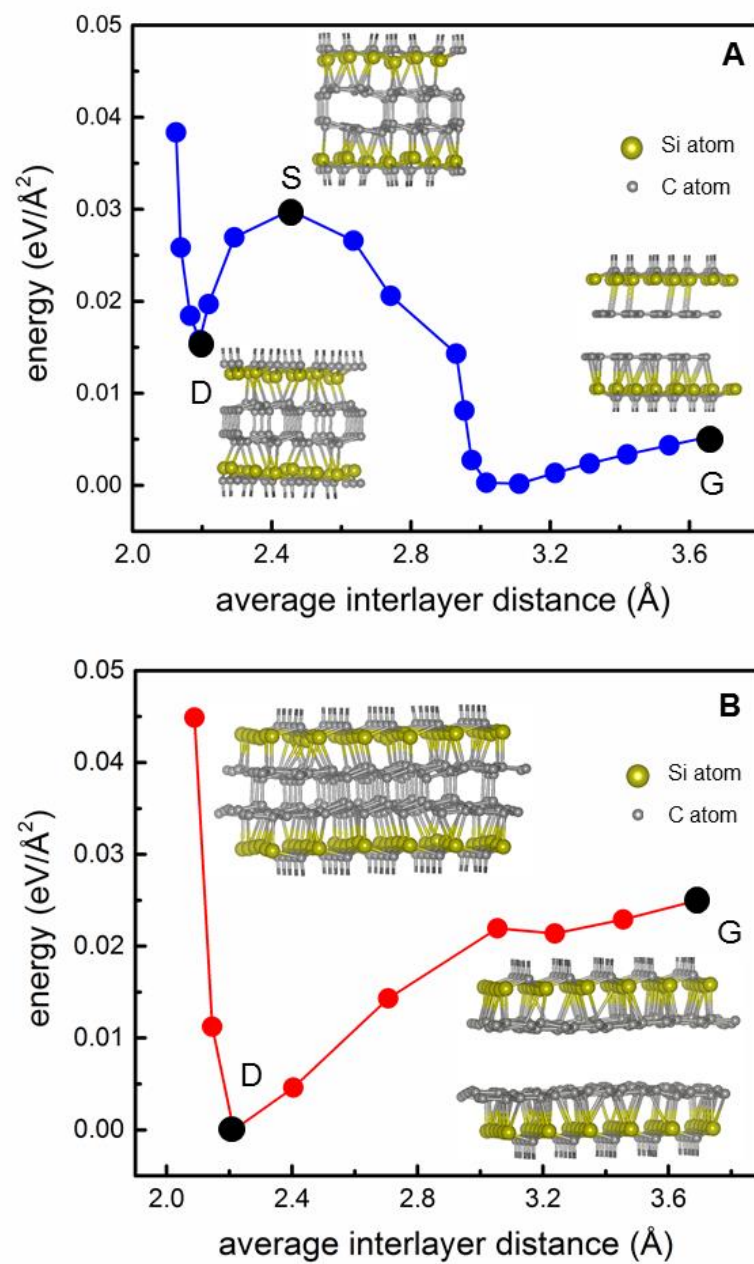
Figure 5.2.7: See caption on next page

Figure 5.2.7: Energy per unit surface area of a two-layer Carbon film sandwiched between mirroring representations of a Si-terminated SiC (0001) surface. Energy values are referred to the smallest one of each curve, and are plotted vs. the average distance between the Carbon layers. (A) Each of the two symmetric halves of the model consist of a graphene layer including 4×4 unit cells matching the Si-face of the SiC-H layer with periodicity of $2\sqrt{3} \times 2\sqrt{3} R30^0$. (B) Each graphene layer includes 6×6 unit cells and the interfacial periodicity with SiC is 5×5. The insets in (A) and (B) are ball-and-stick images of model structures showing two-layer (G) graphene and (D) diamond in contact with the SiC model surfaces. There is also an image of the transition-state model structure (S) in (A), separating the two equilibrium phases of the 2-layer Carbon film.

CHAPTER 6.   SUMMARY & FUTURE DEVELOPMENTS

6.1   Summary

In this thesis, we have presented a new methodology – *Modulated nanoindentation* (*MoNI*) or more straightforwardly – *Å indentation*, which combines sub-Å-resolution indentation measurements and semi-analytical methods (SAM). MoNI is proven to be a powerful tool to measure the elastic moduli of stiff materials (stiffer than SiC) with much higher resolution (both vertically and horizontally) than any other indentation method; more importantly, it also provides a new path to study the elasticity perpendicular-to-the-plane of few-layer-thick 2D materials.

The comparison between indentation experiments and semi-analytical methods has demonstrated that a simpler approach to interpret experimental sub-nm indentation curves in few-layer-thick 2D films is to use the Hertz model. We showed that the fitting of the experimental indentation curves with the Hertz model provides in good approximation the value of the perpendicular-to-the-plane elastic modulus $E_\perp$ of 2D films. The experimental study of epitaxial graphene and different types of graphene oxide (GO) films, combined with DFT calculations, has demonstrated that the interlayer elasticity is extremely sensitive to the presence of intercalated molecules in between the planes. In particular, these studies show that intercalated water in graphene oxide can dramatically change the interlayer elastic modulus, which at first decreases when a small amount of water is intercalated in between the layers and the structure is swelled, and then increases with increasing amount of water until H_2O molecules have completely filled a water layer in between the layers. Above this point, the perpendicular elastic modulus decreases because a second water layer

starts to form in between the layers further swelling and softening the GO structure. This understanding can also explain the different behavior of $E_\perp$ in conventional and epitaxial GO.

The results reported in Chapter IV provide a new path to study the interlayer elastic coupling and the van der Waals forces in few-layer-thick 2D materials, and shed new light on the use of the Hertz model in investigating the perpendicular-to-the-plane Young's modulus of 2D films. This study will impact a variety of fields, from electronics to phononics, allowing new investigations and understanding of the relationship between molecular structure, thermal conductivity, electronic properties, and phonons propagation in layered materials. For example, through local measurements of the elastic modulus, MoNI could probe interlayer and substrate interaction, as well as presence of dopants/intercalates, which are extremely important for modulating the electronic properties of 2D materials. Furthermore, the interlayer elasticity is strictly connected with the out-of-plane thermal properties of layered materials. The here-discussed interlayer elasticity measurements could help understanding the origin of the extremely low out-of-plane thermal conductivity found in thin films of transition metal dichalcogenides (TMDs) [99].

In Chapter V, we have demonstrated that two-layer epitaxial graphene on SiC can be induced into an ultra-stiff and -hard phase by local pressure of ~1GPa at room temperature. DFT calculations corroborate the experimental findings, showing that two-layer graphene on SiC (0001) exhibits small to vanishing energy barriers for the graphitic-to-diamene phase transition. This energy cost depends critically on the possibility to saturate diamene's dangling bonds at the interfaces. These studies open up new ways to

investigate the graphite-diamond phase transitions at room temperature, and suggest a route to produce and pattern single layer diamond by combining local heating and pressure on graphene [25]. Applications range from nanoelectronics and spintronics to force-activated adaptive ultra-strong coatings.

6.2 Future Developments

6.2.1 MoNI with "Hot" AFM Probes

Progress in nanotechnology depends on the capability to fabricate, position, and interconnect nanometer-scale structures. Thermochemical nanolithography (TCNL) [121], invented in our laboratory in 2007, uses a hot AFM tip as a localized source of heat to activate chemical reactions at the macro-down-to the atomic scale. TCNL has been implemented and employed to create nano-patterns for a variety of applications in biology, nanomedicine, nanoelectronics, and nanophotonics [121-123].

So far, we have demonstrated the ability of TCNL to generate proteins arrays with 10 nm-resolution, and concentration gradients of amines and proteins with sub-100 nm resolution [124, 125]. TCNL was also implemented to fabricate conjugate semiconducting polymer nanowires [126], piezoelectric/ferroelectric PZT and PTO ceramic nanostructures [127] and graphene nanoribbons [25]. TCNL has a broad range of applicability given the extreme writing speed (mm/s for most of the above mentioned reactions), potential massive parallelization (application of tip array has been demonstrated [105]), and high resolution (down to 10 nm). Some typical results are shown in Fig. 6.2.1 to Fig. 6.2.3.
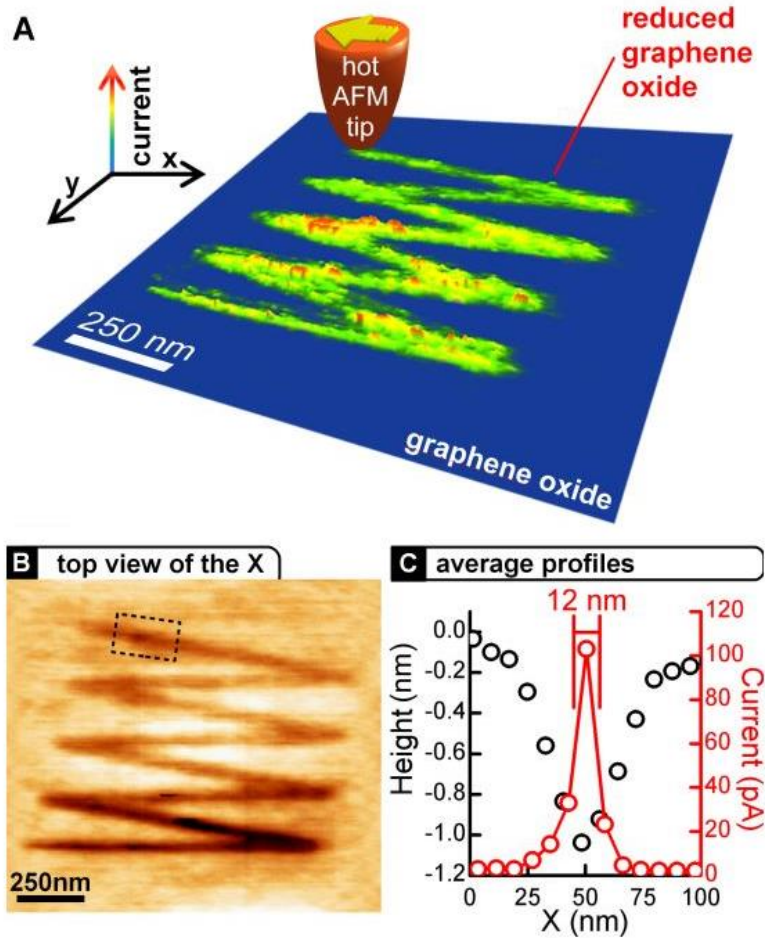
Figure 6.2.1: Local thermal reduction of an epitaxial graphene oxide (EGO) film: current and topographical images. (A) 3D CAFM current image (taken with a bias voltage of 2.5 V between tip and substrate) of a zigzag shaped nanowire formed after TCNL was performed on EGO at $T_{heater} \sim 1060$ °C with a linear speed of 0.2µm/s and a load of 120nN. (B) Corresponding topography image taken simultaneously with (A). (C) Averaged profiles of current and height of the cross sections that are indicated as dashed lines in (A) and (B). Reprinted with permission from [31], Copyright 2010, AAAS.
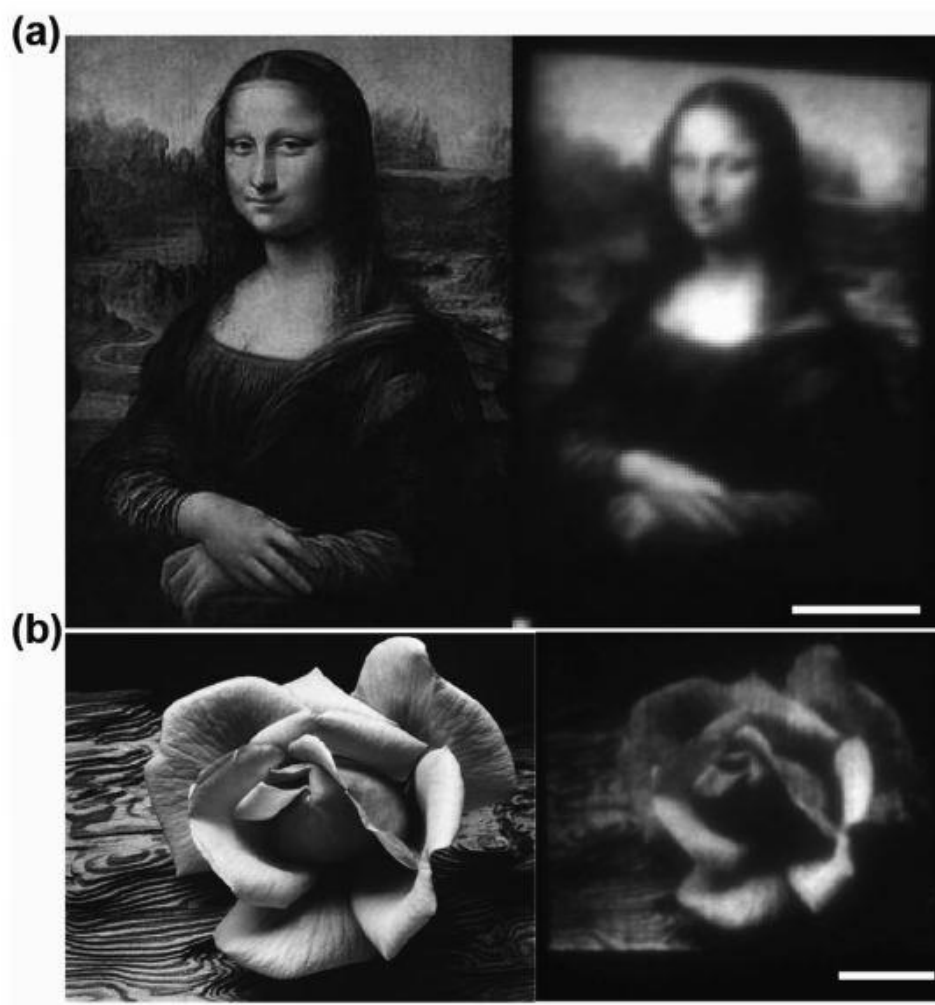
Figure 6.2.2: (a) (Left) Original image of the Mona Lisa, scaled and pixelated for input into the model in order to extract a power map. (Right) Experimental rendition of the Mona Lisa with a total width of just ~ 32 μm produced by TCNL. Scale bar: 10 μm. (b) (Left) Rose and Driftwood, 1932, photograph by Ansel Adams, copyright 2012 The Ansel Adams Publishing Rights Trust. (Right) TCNL reproduction of the photograph. Scale bar: 10 μm. Reprinted with permission from [122]. Copyright 2013, American Chemistry Society.
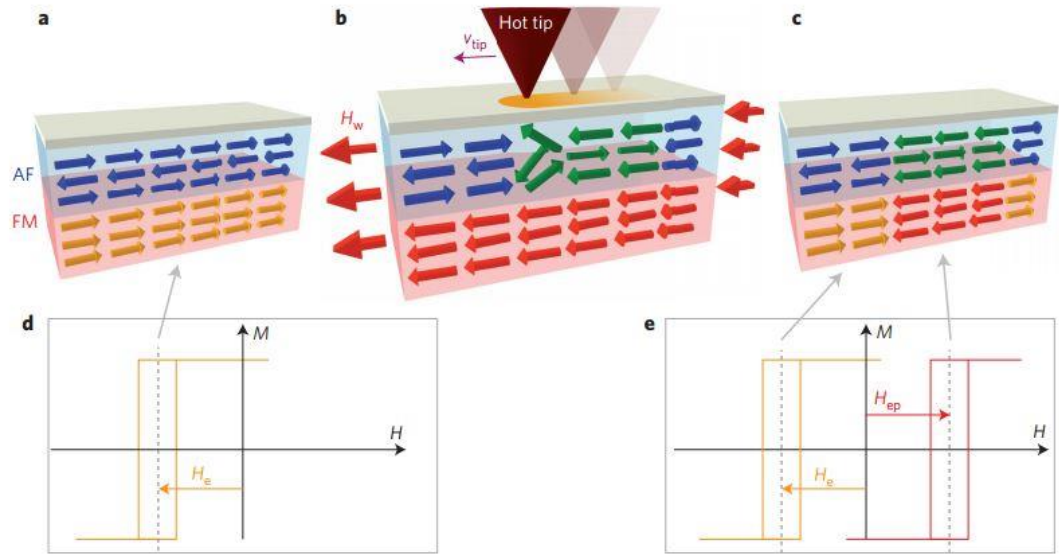
Figure 6.2.3: Magnetic patterning via TCNL. (a) After initialization, the magnetization of the ferromagnetic (FM) layer (yellow arrows) is uniformly pinned in one direction by the exchange interaction with the antiferromagnetic (AF) layer (blue arrows). (b) Sweeping a heated AFM tip on the sample surface in the presence of an external magnetic field H_w produces a local field cooling in the anti-ferromagnet (green arrows), which resets the exchange bias direction according to the underlying CoFeB spins (red arrows), aligned with H_w. (c) When the external magnetic field H_w is removed, the magnetic domain configuration in the ferromagnet is stabilized by the local exchange bias. (d, e) Magnetic hysteresis loops before (d) and after (e) patterning. H_e and H_{ep} indicate the opposite shift in the loops due to the exchange bias in the non-patterned and patterned areas, respectively. Reprinted with permission from [123]. Copyright 2016, Nature Publishing Group.

In Chapter V, we showed that a local pressure of ~ 1GPa by an AFM Silicon Probe can induce an ultra-stiff phase - diamene in 2-layer epitaxial graphene on SiC (0001). However, when the probe is completely retracted, the surface dangling bonds of diamene become unsaturated and active again, resulting in an unstable structure which will quickly collapse back into the original graphitic structure. What if we press 2L EG with *a heated AFM probe* under the same pressure? First of all, the additional energy injected by the local heating could help the graphene/diamene system skip the energy barrier (as shown in Fig. 5.2.7) much more easily. Furthermore, the local heating might be able to activate permanent dangling bonds saturation with passivating molecules in the surrounding atmosphere such as Hydrogen gas. As a consequence, the diamene structure can be created with less difficulty and even be stabilized after probe retraction. Single-layer diamond arrays or ribbons can be easily created by TCNL with a mediate pressure.

6.2.2   *MoNI on Van der Waals Heterostructures*

Van der Waals (vdW) heterostructure, where different 2D materials are assembled layer by layer with van der Waals force [128] as shown in Fig. 6.2.4, has very unique electronic, optical and thermal properties, and consequently a wide range of applications, including vertical transistor, p-n junctions, phototransistors and LEDs [128-131].

For future research, one can investigate the perpendicular elasticity, or more specifically, the unique van der Waals elastic interaction, of 2D heterostructures made of a variety of vdW materials, including mixing insulating, metallic and semiconducting layers, with the help of MoNI. The vertical mechanical, electronic and thermal transport properties of vdW heterostructures are strongly dependent on the following factors: strength of the

interlayer vdW bonds, stacking order, presence of defects in between the layer space, etc. All those factors are also correlated to the vertical elastic properties, which can be precisely investigated via MoNI. Furthermore, one might be able to tune the transverse transport properties by applying high mechanical load locally via MoNI. To conclude, MoNI can play a significant role in the study of van der Waals heterostructures due to its high flexibility, precision and potential wide range of applications.
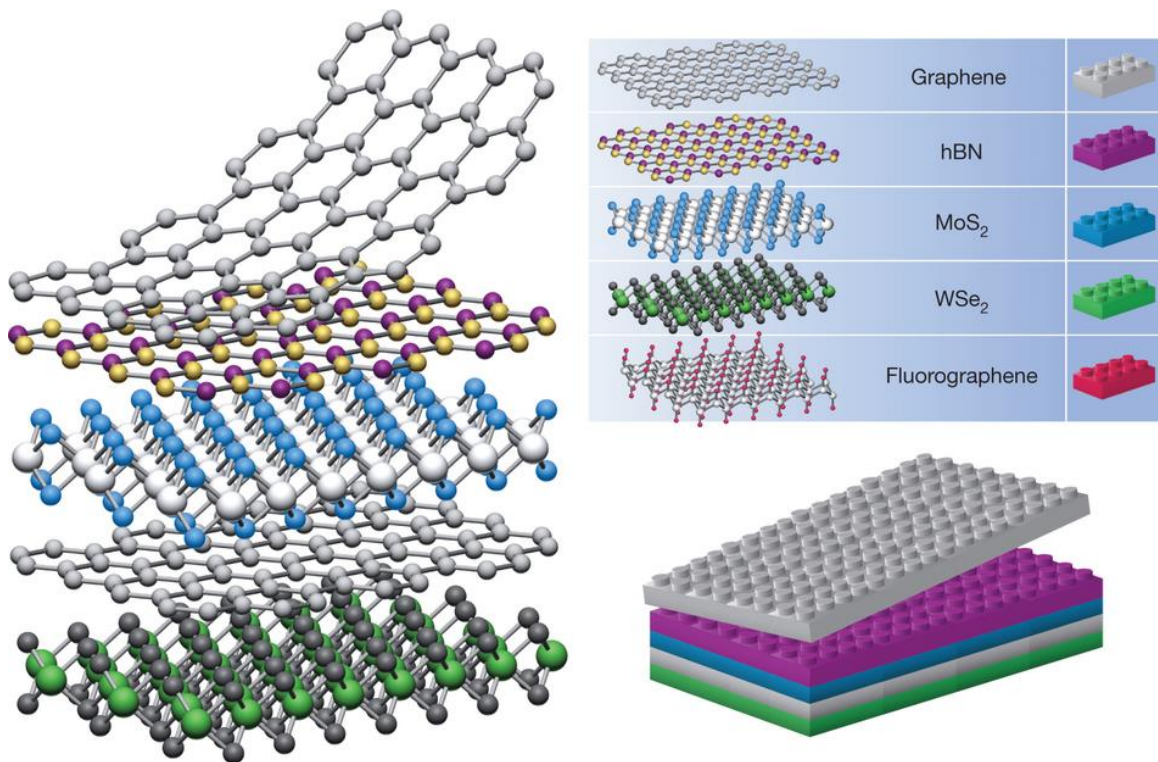

Figure 6.2.4: Van der Waals heterostructure. The 2D layers can be regarded as Lego blocks (right panel), the construction of a huge variety of layered structures becomes possible. Reprinted with permission from [128]. Copyright 2013, Nature Publishing Group.

6.2.3 *Perpendicular Elasticity and Thermal Conductivity*

The perpendicular thermal conductivity of thin films of TMDC are expected to show an extremely low thermal conductivity, which makes these films very attractive for thermoelectric applications. Recently it was shown [99, 132] that the thermal conductivity of thin films of WSe_2 grown from alternating W and Se layers is as small as 0.05 W/(m $\cdot$ K) at room temperature, 30 times smaller than the c-axis thermal conductivity of single-crystal WSe_2 and a factor of 6 smaller than the predicted minimum thermal conductivity for this material. The authors attributed the ultralow thermal conductivity of these disordered, layered crystals to the localization of lattice vibrations induced by the random stacking of two-dimensional crystalline WSe_2 sheets. They also observed that disordering of the layered structure by ion bombardment increases the thermal conductivity. Here, we propose to use the method - scanning spin probe (as shown in Fig. 6.2.5), which can be used to measure with nanoscale resolution the thermal conductivity of 2D films [133]. In particular, we are interested to relate the perpendicular elasticity and the vdW interaction between the planes with the perpendicular thermal conductivity. MoNI combined with scanning spin probe is offering the opportunity to understand the origin of the high thermal conductivity in 2D films and to investigate the role of defects, disorder, layer/layer twist and stacking in defining the perpendicular thermal conductivity of complex heterogeneous 2D films. To insure that we will measure only the perpendicular thermal conductivity we could fabricate nano-patterns of 2D structures either by conventional lithography or by TCNL.

130
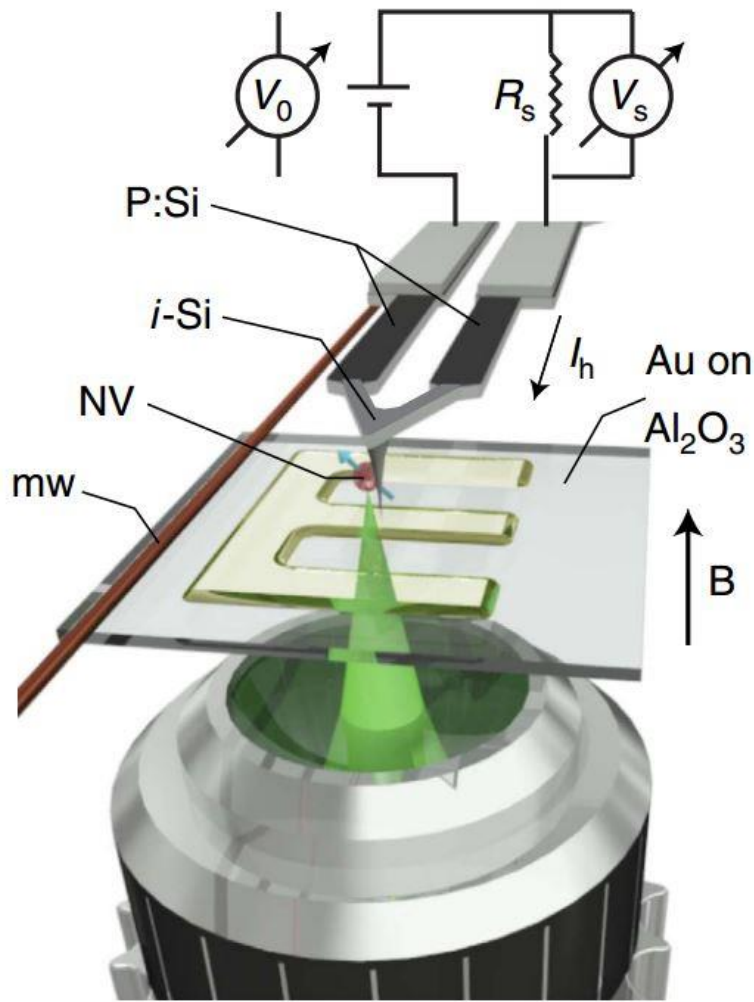
Figure 6.2.5: Schematics of our experimental setup. An electrical current circulates along the arms of a thermal AFM cantilever (phosphorous-doped Si) and heats up the end section above the tip (intrinsic Si). A high-NA objective excites and collects the fluorescence emitted by a diamond-nanocrystal-hosted Nitrogen vacancy (NV) attached to the AFM tip. A wire on the sample surface serves as the source of mw. The resistance (and thus temperature) of the intrinsic segment of the cantilever can be determined from the measured current Ih ¼ Vs/Rs and applied voltage V0. Our experiments are carried out in the presence of a magnetic field B along the direction normal to the sample. Reprinted with permission from [133]. Copyright 2015, Nature Publishing Group.

REFERENCES

[1] L.D. Landau, E.M. Lifshitz, Pergamon Press Ltd. (1959).

[2] K.L. Johnson, Cambridge University Press (1987).

[3] G. Binnig, C.F. Quate, C. Gerber, Phys. Rev. Lett., 56 (1986) 930.

[4] I.S. Sokolnikoff, R.D. Specht, McGraw-Hill New York (1956).

[5] K. Johnson, K. Kendall, A. Roberts, Proc. of the Royal Society of London A: Math., Phys. and Engi. Sci, The Royal Society (1971), pp. 301-313.

[6] B.V. Derjaguin, V.M. Muller, Y.P. Toporov, J. of Colloid and Interface Sci., 53 (1975) 314-326.

[7] D. Maugis, J. of Colloid and Interface Sci., 150 (1992) 243-269.

[8] D. Tabor, J. of Colloid and Interface Sci., 58 (1977) 2-13.

[9] R.W. Carpick, D.F. Ogletree, M. Salmeron, J. of Colloid and Interface Sci., 211 (1999) 395-400.

[10] B. Bhushan, Springer Science & Business Media (2010).

[11] G. Binnig, H. Rohrer, C. Gerber, E. Weibel, Phys. Rev. Lett., 49 (1982) 57.

[12] J.E. Jones, Proc. of the Royal Soc. of London A: Math., Phys. and Engi. Sci., The Royal Society1924, pp. 463-477.

[13] S. Magonov, V. Elings, M.-H. Whangbo, Surf. Sci., 375 (1997) L385-L391.

[14] P. De Wolf, J. Snauwaert, T. Clarysse, W. Vandervorst, L. Hellemans, Appl. Phys. Lett., 66 (1995) 1530-1532.

[15] P. Girard, Nanotechnology, 12 (2001) 485.

[16] M. Nonnenmacher, M. o'Boyle, H.K. Wickramasinghe, Appl. Phys. Lett., 58 (1991) 2921-2923.

[17] Y. Martin, H.K. Wickramasinghe, Appl. Phys. Lett., 50 (1987) 1455-1457.

[18] A.K. Geim, K.S. Novoselov, Nat. Mater., 6 (2007) 183-191.

[19] S.Z. Butler, S.M. Hollen, L. Cao, Y. Cui, J.A. Gupta, H.R. Gutiérrez, T.F. Heinz, S.S. Hong, J. Huang, A.F. Ismach, ACS Nano, 7 (2013) 2898-2926.

[20] M. Xu, T. Liang, M. Shi, H. Chen, Chem. Rev., 113 (2013) 3766-3798.

[21] J.Y. Park, S. Kwon, J.H. Kim, Adv. Mater. Interfaces, 1 (2014).

[22] A.K. Geim, Science, 324 (2009) 1530-1534.

[23] W.A. De Heer, C. Berger, X. Wu, P.N. First, E.H. Conrad, X. Li, T. Li, M. Sprinkle, J. Hass, M.L. Sadowski, Solid State Comm., 143 (2007) 92-100.

[24] C. Berger, Z. Song, X. Li, X. Wu, N. Brown, C. Naud, D. Mayou, T. Li, J. Hass, A.N. Marchenkov, Science, 312 (2006) 1191-1196.

[25] Z. Wei, D. Wang, S. Kim, S.-Y. Kim, Y. Hu, M.K. Yakes, A.R. Laracuente, Z. Dai, S.R. Marder, C. Berger, W.P. King, W. De Heer, P.E. Sheehan, E. Riedo, Science, 328 (2010) 1373-1376.

[26] A.C. Neto, F. Guinea, N.M. Peres, K.S. Novoselov, A.K. Geim, Rev. of Sci. Instrum., 81 (2009) 109.

[27] Y. Zhang, Y.-W. Tan, H.L. Stormer, P. Kim, Nature, 438 (2005) 201-204.

[28] K.S. Novoselov, Z. Jiang, Y. Zhang, S. Morozov, H.L. Stormer, U. Zeitler, J. Maan, G. Boebinger, P. Kim, A.K. Geim, Science, 315 (2007) 1379-1379.

[29] X. Du, I. Skachko, F. Duerr, A. Luican, E.Y. Andrei, Nature, 462 (2009) 192-195.

[30] W.-K. Tse, Z. Qiao, Y. Yao, A. MacDonald, Q. Niu, Phys. Rev. B, 83 (2011) 155447.

[31] S. Kim, S. Zhou, Y. Hu, M. Acik, Y.J. Chabal, C. Berger, W. de Heer, A. Bongiorno, E. Riedo, Nat. Mater., 11 (2012) 544-549.

[32] J.W. Suk, R.D. Piner, J. An, R.S. Ruoff, Acs Nano, 4 (2010) 6557-6564.

[33] D.R. Dreyer, S. Park, C.W. Bielawski, R.S. Ruoff, Chem. Soc. Rev., 39 (2010) 228-240.

[34] Y. Zhu, S. Murali, W. Cai, X. Li, J.W. Suk, J.R. Potts, R.S. Ruoff, Adv. Mater., 22 (2010) 3906-3924.

[35] Q.H. Wang, K. Kalantar-Zadeh, A. Kis, J.N. Coleman, M.S. Strano, Nat. Nanotech., 7 (2012) 699-712.

[36] M. Chhowalla, H.S. Shin, G. Eda, L.-J. Li, K.P. Loh, H. Zhang, Nat. Chem., 5 (2013) 263-275.

[37] B. Radisavljevic, A. Radenovic, J. Brivio, V. Giacometti, A. Kis, Nat. Nanotech., 6 (2011) 147-150.

[38] K.S. Novoselov, A.K. Geim, S. Morozov, D. Jiang, Y. Zhang, S. Dubonos, I. Grigorieva, A. Firsov, Science, 306 (2004) 666-669.

[39] C. Berger, Z. Song, T. Li, X. Li, A.Y. Ogbazghi, R. Feng, Z. Dai, A.N. Marchenkov, E.H. Conrad, P.N. First, W. De Heer, The J. of Phys. Chem. B, 108 (2004) 19912-19916.

[40] C. Lee, X. Wei, J.W. Kysar, J. Hone, Science, 321 (2008) 385-388.

[41] J.-H. Chen, C. Jang, S. Xiao, M. Ishigami, M.S. Fuhrer, Nat. Nanotech., 3 (2008) 206-209.

[42] S.K. Banerjee, L.F. Register, E. Tutuc, D. Basu, S. Kim, D. Reddy, A.H. MacDonald, Proc. of the IEEE, 98 (2010) 2032-2046.

[43] Y.-M. Lin, C. Dimitrakopoulos, K.A. Jenkins, D.B. Farmer, H.-Y. Chiu, A. Grill, P. Avouris, Science, 327 (2010) 662-662.

[44] C. Liu, Z. Yu, D. Neff, A. Zhamu, B.Z. Jang, Nano Lett., 10 (2010) 4863-4868.

[45] Y. Wang, Z. Shi, Y. Huang, Y. Ma, C. Wang, M. Chen, Y. Chen, The J. of Phys. Chem. C, 113 (2009) 13103-13107.

[46] A.A. Balandin, S. Ghosh, W. Bao, I. Calizo, D. Teweldebrhan, F. Miao, C.N. Lau, Nano Lett., 8 (2008) 902-907.

[47] R.R. Nair, P. Blake, A.N. Grigorenko, K.S. Novoselov, T.J. Booth, T. Stauber, N.M. Peres, A.K. Geim, Science, 320 (2008) 1308-1308.

[48] D. Wei, Y. Liu, Y. Wang, H. Zhang, L. Huang, G. Yu, Nano Lett., 9 (2009) 1752-1758.

[49] A. Reina, X. Jia, J. Ho, D. Nezich, H. Son, V. Bulovic, M.S. Dresselhaus, J. Kong, Nano Lett., 9 (2008) 30-35.

[50] W. Norimatsu, M. Kusunoki, Phys. Chem. Chem. Phys., 16 (2014) 3501-3511.

[51] W.A. De Heer, C. Berger, M. Ruan, M. Sprinkle, X. Li, Y. Hu, B. Zhang, J. Hankinson, E. Conrad, Proc. Natl. Acad. Sci., 108 (2011) 16900-16905.

[52] W.S. Hummers Jr, R.E. Offeman, J. of the Am. Chem. Soc., 80 (1958) 1339-1339.

[53] S. Park, R.S. Ruoff, Nat. Nanotech., 4 (2009) 217-224.

[54] G. Eda, G. Fanchini, M. Chhowalla, Nat. Nanotech., 3 (2008) 270-274.

[55] V. Chandra, J. Park, Y. Chun, J.W. Lee, I.-C. Hwang, K.S. Kim, ACS Nano, 4 (2010) 3979-3986.

[56] Y. Xu, H. Bai, G. Lu, C. Li, G. Shi, J. of Am. Chem. Soc., 130 (2008) 5856-5857.

[57] N. Li, M. Zheng, H. Lu, Z. Hu, C. Shen, X. Chang, G. Ji, J. Cao, Y. Shi, Chem. Comm., 48 (2012) 4106-4108.

[58] K.P. Loh, Q. Bao, G. Eda, M. Chhowalla, Nat. Chem., 2 (2010) 1015-1024.

[59] S. Park, J. An, J.W. Suk, R.S. Ruoff, Small, 6 (2010) 210-212.

[60] S. Zhou, S. Kim, E. Di Gennaro, Y. Hu, C. Gong, X. Lu, C. Berger, W. de Heer, E. Riedo, Y. Chabal, Adv. Mater. Interfaces, (2014).

[61] C.R. Dean, A.F. Young, I. Meric, C. Lee, L. Wang, S. Sorgenfrei, K. Watanabe, T. Taniguchi, P. Kim, K. Shepard, Nat. Nanotech., 5 (2010) 722-726.

[62] L. Ci, L. Song, C. Jin, D. Jariwala, D. Wu, Y. Li, A. Srivastava, Z. Wang, K. Storr, L. Balicas, Nat. Mater., 9 (2010) 430-435.

[63] L. Song, L. Ci, H. Lu, P.B. Sorokin, C. Jin, J. Ni, A.G. Kvashnin, D.G. Kvashnin, J. Lou, B.I. Yakobson, Nano Lett., 10 (2010) 3209-3215.

[64] J. Wilson, A. Yoffe, Adv. in Phys., 18 (1969) 193-335.

[65] H. Schmidt, S. Wang, L. Chu, M. Toh, R. Kumar, W. Zhao, A.H. Castro Neto, J. Martin, S. Adam, B. Özyilmaz, Nano Lett., 14 (2014) 1909-1913.

[66] A. Castellanos-Gomez, M. Poot, G.A. Steele, H.S. van der Zant, N. Agrait, G. Rubio-Bollinger, Adv. Mater., 24 (2012) 772-775.

[67] Z. Yin, H. Li, H. Li, L. Jiang, Y. Shi, Y. Sun, G. Lu, Q. Zhang, X. Chen, H. Zhang, ACS Nano, 6 (2011) 74-80.

[68] C. Zhu, Z. Zeng, H. Li, F. Li, C. Fan, H. Zhang, J. of Am. Chem. Soc., 135 (2013) 5998-6001.

[69] J.R. Brent, N. Savjani, E.A. Lewis, S.J. Haigh, D.J. Lewis, P. O'Brien, Chem. Comm., 50 (2014) 13338-13341.

[70] Q. Wei, X. Peng, Appl. Phys. Lett., 104 (2014) 251915.

[71] L. Li, Y. Yu, G.J. Ye, Q. Ge, X. Ou, H. Wu, D. Feng, X.H. Chen, Y. Zhang, Nat. Nanotech., 9 (2014) 372-377.

[72] J. Sun, H.-W. Lee, M. Pasta, H. Yuan, G. Zheng, Y. Sun, Y. Li, Y. Cui, Nat. Nanotech., 10 (2015) 980-985.

[73] L. Kou, C. Chen, S.C. Smith, The J. of Phys. Chem. Lett., 6 (2015) 2794-2805.

[74] H. Liu, A.T. Neal, Z. Zhu, X. Xu, D. Tomanek, P.D. Ye, Z. Luo, Acs Nano, (2014).

[75] E.S. Reich, Nature, 506 (2014) 19.

[76] S. Das, W. Zhang, M. Demarteau, A. Hoffmann, M. Dubey, A. Roelofs, Nano Lett., 14 (2014) 5733-5739.

[77] B. Poon, D. Rittel, G. Ravichandran, Intern. J. of Solids and Structures, 45 (2008) 6018-6033.

[78] G. Pharr, W. Oliver, MRS Bulletin, 17 (1992) 28-33.

[79] T. Chudoba, N. Schwarzer, F. Richter, U. Beck, Thin Solid Films, 377 (2000) 366-372.

[80] T. Chudoba, N. Schwarzer, F. Richter, Surf. and Coat. Technol., 127 (2000) 9-17.

[81] R. Saha, W.D. Nix, Acta Mater., 50 (2002) 23-38.

[82] T. Chudoba, N. Schwarzer, F. Richter, Thin Solid Films, 355 (1999) 284-289.

[83] B. Bhushan, V.N. Koinkar, Appl. Phys. Lett., 64 (1994) 1653-1655.

[84] M. Lucas, K. Gall, E. Riedo, J. of Appl. Phys., 104 (2008) 113515.

[85] Y. Gao, S. Kim, S. Zhou, H.-C. Chiu, D. Nélias, C. Berger, W. De Heer, L. Polloni, R. Sordan, A. Bongiorno, E. Riedo, Nat. Mater., 14 (2015) 714-720.

[86] H.C. Chiu, S. Kim, C. Klinke, E. Riedo, Appl. Phys. Lett., 101 (2012) 103109.

[87] M. Lucas, W. Mai, R. Yang, Z.L. Wang, E. Riedo, Nano Lett., 7 (2007) 1314-1317.

[88] I. Palaci, S. Fedrigo, H. Brune, C. Klinke, M. Chen, E. Riedo, Phys. Rev. Lett., 94 (2005) 175502.

[89] B.T. Kelly, (Applied Science, London, 1981).

[90] J. Willis, J. of the Mech. and Phys. of Solids, 14 (1966) 163-176.

[91] S.R. Swanson, Inter. J. of Solids and Structures, 41 (2004) 1945-1959.

[92] J.E. Sader, I. Larson, P. Mulvaney, L.R. White, Rev. of Sci. Instrum., 66 (1995) 3789-3798.

[93] C.P. Green, J.E. Sader, J. of Appl. Phys., 92 (2002) 6262-6274.

[94] J.E. Sader, J.W. Chon, P. Mulvaney, Rev. of Sci. Instrum., 70 (1999) 3967-3969.

[95] J.E. Sader, J. of Appl. Phys., 84 (1998) 64-76.

[96] S. Kwon, S. Choi, H. Chung, H. Yang, S. Seo, S.-H. Jhi, J. Young Park, Appl. Phys. Lett., 99 (2011) 013110.

[97] B. Hajgató, S. Güryel, Y. Dauphin, J.-M. Blairon, H.E. Miltner, G. Van Lier, F. De Proft, P. Geerlings, Chem. Phys. Lett., 564 (2013) 37-40.

[98] N. Nakamura, H. Ogi, M. Hirao, Ultrasonics, 42 (2004) 491-494.

[99] C. Chiritescu, D.G. Cahill, N. Nguyen, D. Johnson, A. Bodapati, P. Keblinski, P. Zschack, Science, 315 (2007) 351-353.

[100] C. Riedl, C. Coletti, U. Starke, J. of Phys. D: Appl. Phys., 43 (2010) 374009.

[101] M. Lucas, X. Zhang, I. Palaci, C. Klinke, E. Tosatti, E. Riedo, Nat. Mater., 8 (2009) 876-881.

[102] P. Tan, W. Han, W. Zhao, Z. Wu, K. Chang, H. Wang, Y. Wang, N. Bonini, N. Marzari, N. Pugno, Nat. Mater., 11 (2012) 294-300.

[103] C. Bagault, D. Nelias, M.-C. Baietto, T.C. Ovaert, Intern. J. of Solids and Structures, 50 (2013) 743-754.

[104] C. Bagault, D. Nelias, M.-C. Baietto, J. of Tribo., 134 (2012) 031401.

[105] K.M. Carroll, X. Lu, S. Kim, Y. Gao, H.-J. Kim, S. Somnath, L. Polloni, R. Sordan, W.P. King, J.E. Curtis, E. Riedo, Nanoscale, 6 (2014) 1299-1304.

[106] P. Giannozzi, S. Baroni, N. Bonini, M. Calandra, R. Car, C. Cavazzoni, D. Ceresoli, G.L. Chiarotti, M. Cococcioni, I. Dabo, A. Da1 Corso, S. de Gironcoli, S. Fabris, G. Fratesi, R. Gebauer, U. Gerstmann, C. Gougoussis, A. Kokalj, M. Lazzeri, L. Martin-Samos, N. Marzari, F. Mauri, R. Mazzarello, S. Paolini, A. Pasquarello, L. Paulatto, C. Sbraccia, S. Scandolo, G. Sclauzero, A.P. Seitsonen, A. Smogunov, P. Umari, R.M. Wentzcovitch, J. Phys.: Condens. Matter, 21 (2009) 395502.

[107] N. Troullier, J.L. Martins, Phys. Rev. B, 43 (1991) 1993.

[108] J.P. Perdew, K. Burke, M. Ernzerhof, Phys. Rev. Lett., 77 (1996) 3865.

[109] S. Grimme, J. of Compu. Chem, 27 (2006) 1787-1799.

[110] V. Barone, M. Casarin, D. Forrer, M. Pavone, M. Sambi, A. Vittadini, J. of Compu. Chem., 30 (2009) 934-939.

[111] A. Bosak, M. Krisch, M. Mohr, J. Maultzsch, C. Thomsen, Phys. Rev. B, 75 (2007) 153408.

[112] P.W. May, Philo. Trans. of the Royal Society of London A: Math., Phys. and Engi. Sci., 358 (2000) 473-495.

[113] S. Ryu, M.Y. Han, J. Maultzsch, T.F. Heinz, P. Kim, M.L. Steigerwald, L.E. Brus, Nano Lett., 8 (2008) 4597-4602.

[114] D.C. Elias, R.R. Nair, T. Mohiuddin, S. Morozov, P. Blake, M. Halsall, A. Ferrari, D. Boukhvalov, M. Katsnelson, A. Geim, Science, 323 (2009) 610-613.

[115] S. Rajasekaran, F. Abild-Pedersen, H. Ogasawara, A. Nilsson, S. Kaya, Phys. Rev. Lett., 111 (2013) 085503.

[116] A.G. Kvashnin, L.A. Chernozatonskii, B.I. Yakobson, P.B. Sorokin, Nano Lett., 14 (2014) 676-681.

[117] Z. Luo, T. Yu, K.-j. Kim, Z. Ni, Y. You, S. Lim, Z. Shen, S. Wang, J. Lin, Acs Nano, 3 (2009) 1781-1788.

[118] D.D. C. Berger, J. Gigliotti, J. Palmer, J. Hankinson, Y. Hu, J.-P. Turmaud, R. Puybaret, A. Ougazzaden, A. Sidorov, Z. Jiang, W.A. de Heer, arXiv:1611.08937 (2016).

[119] T. Filleter, K. Emtsev, T. Seyller, R. Bennewitz, Appl. Phys. Lett., 93 (2008) 3117.

[120] S. Kumar, D.M. Parks, Nano Lett., 15 (2015) 1503-1510.

[121] R. Szoszkiewicz, T. Okada, S.C. Jones, T.-D. Li, W.P. King, S.R. Marder, E. Riedo, Nano Lett., 7 (2007) 1064-1069.

[122] K.M. Carroll, A.J. Giordano, D. Wang, V.K. Kodali, J. Scrimgeour, W.P. King, S.R. Marder, E. Riedo, J.E. Curtis, Langmuir, 29 (2013) 8675-8682.

[123] E. Albisetti, D. Petti, M. Pancaldi, M. Madami, S. Tacchi, J. Curtis, W. King, A. Papp, G. Csaba, W. Porod, P. Vavassori, E. Riedo, R. Bertacco, Nat. Nanotech., (2016).

[124] D. Wang, V.K. Kodali, I. Underwood, D. William, J.E. Jarvholm, T. Okada, S.C. Jones, M. Rumi, Z. Dai, W.P. King, S.R. Marder, J.E. Curtis, E. Riedo, Adv. Func. Mater., 19 (2009) 3696-3702.

[125] E. Albisetti, K. Carroll, X. Lu, J. Curtis, D. Petti, R. Bertacco, E. Riedo, Nanotechnology, 27 (2016) 315302.

[126] D. Wang, S. Kim, W.D. Underwood, A.J. Giordano, C.L. Henderson, Z. Dai, W.P. King, S.R. Marder, E. Riedo, Appl. Phys. Lett., 95 (2009) 233108.

[127] S. Kim, Y. Bastani, H. Lu, W.P. King, S. Marder, K.H. Sandhage, A. Gruverman, E. Riedo, N. Bassiri-Gharb, Adv. Mater., 23 (2011) 3786-3790.

[128] A.K. Geim, I.V. Grigorieva, Nature, 499 (2013) 419-425.

[129] C.-H. Lee, G.-H. Lee, A.M. Van Der Zande, W. Chen, Y. Li, M. Han, X. Cui, G. Arefe, C. Nuckolls, T.F. Heinz, Nat. Nanotech., 9 (2014) 676-681.

[130] H. Fang, C. Battaglia, C. Carraro, S. Nemsak, B. Ozdol, J.S. Kang, H.A. Bechtel, S.B. Desai, F. Kronast, A.A. Unal, Proc. Natl. Aca. Sci., 111 (2014) 6198-6202.

[131] F. Withers, O. Del Pozo-Zamudio, A. Mishchenko, A. Rooney, A. Gholinia, K. Watanabe, T. Taniguchi, S. Haigh, A. Geim, A. Tartakovskii, Nat. Mater., 14 (2015) 301-306.

[132] R. Costescu, D. Cahill, F. Fabreguette, Z. Sechrist, S. George, Science, 303 (2004) 989-990.

[133] A. Laraoui, H. Aycock-Rizzo, Y. Gao, X. Lu, E. Riedo, C.A. Meriles, Nat. Comm., 6 (2015).

LIST OF PUBLICATIONS

Published

1. Alper Gurarslan, Shuping Jiao, Tai-De Li, Guoqing Li, Yiling Yu, Yang Gao, Elisa Riedo, Zhiping Xu and Linyou Cao, "Van der waals force isolation of monolayer MoS_2", *Advanced Materials*, **28** (2016) 10055-10060.

2. Yang Gao[*], Suenne Kim[*], Si Zhou, Hsian-Chih Chiu, Daniel Nelias, Claire Berger, Walt de Heer, Roman Sordan, Laura Polloni, Angelo Bongiorno and Elisa Riedo, "Elastic coupling between the layers in 2D materials", *Nature Materials*, **14** (2015), 714-720.

3. Abdelghani Laraoui, Halley Aycock-Rizzo, Yang Gao, Xi Lu, Elisa Riedo and Carlos Meriles, "Imaging thermal conductivity with nanoscale resolution using a scanning spin probe", *Nature Communications*, **6** (2015)

4. Keith Carroll, Xi Lu, Suenne Kim, Yang Gao, Hoe-Joon Kim, Suhas Somnath, Laura Polloni, Roman Sordan, William King, Jennifer Curtis and Elisa Riedo, "Parallelization of thermochemical nanolithography" *Nanoscale*, **6** (2014) 1299-1304.

Submitted

1. Yang Gao[*], Tengfei Cao*, Claire Berger, Walt de Heer, Angelo Bongiorno and Elisa Riedo, "Inducing an ultra-stiff phase in two-layer graphene: the fingerprint of diamene", submitted to *Nature Nanotechnology*

*: shared first author